From Excitons to Polaritons: Strong Coupling and Ultrafast Dynamics in 2D Perovskite Microcavities

Yan Chen

The University of Sheffield

School of Mathematical and Physical Sciences

A thesis submitted for the degree of Doctor of Philosophy

Feb 2026

For my grandfather,

who I wish were here to see this.

For my parents, sister, and grandmother,

whose love has carried me here.

For my boyfriend, Peter Claronino,

who walks beside me.

Acknowledgements

First and foremost, I would like to express my sincere gratitude to my supervisor, Professor David Lidzey, for his guidance, patience, and invaluable insight throughout the course of this research. His support and expertise have been instrumental to the completion of this work.

I am also deeply grateful to my colleagues in the EPMM group and within the department for their assistance, collaborations, stimulating discussions, and continued support. Working alongside them made this journey both intellectually rewarding and personally enriching.

In particular, I would like to thank Dr. Kyriacos Georgiou (University of Cyprus) for his exceptional mentorship, and for sharing his extensive knowledge, which greatly contributed to this research. I am sincerely thankful to Dr. Tingxiang Yang for her assistance with the TRPL and the pump-probe measurements presented in this thesis. I also thank Timothy Thornber for his help with the XRD measurements. Finally, I would like to acknowledge Dr. Alex Ramadan, whose insightful discussions and enthusiasm for perovskite research provided significant inspiration for this work.

Abstract

Two-dimensional (2D) metal halide perovskites are promising materials for exploring strong light-matter coupling due to their large exciton binding energies and pronounced excitonic resonances. This thesis investigates the structural, optical, and dynamical properties of n = 1 butylammonium lead iodide (BA_2PbI_4) thin films and their integration into distributed Bragg reflector (DBR) microcavities.

Film morphology was optimized using solvent and additive engineering. AFM and XRD measurements showed that incorporation of 18-crown-6 significantly improved film uniformity and crystallinity. Optical spectroscopy confirmed strong excitonic absorption and narrow photoluminescence linewidths. Angle-resolved reflectivity measurements of DBR cavities revealed clear anti-crossing behaviour at room temperature, demonstrating strong coupling and exciton-polariton formation.

Low-temperature measurements identified amplified spontaneous emission (ASE) in films and bilayer structures. However, power-dependent photoluminescence studies of cavities showed no evidence of polariton condensation. Ultrafast pump-probe spectroscopy suggests that short polariton lifetimes, cavity losses, and relaxation bottlenecks limit condensation.

Contents

Chapter 1

Introduction

Over the past several decades, semiconductors have revolutionized the modern world. Advances in semiconductor fabrication and nanostructuring have enabled devices with decreasing dimensions and increasingly complicated functionalities, underpinning progress across a broad range of fields including optoelectronics, communications, sensing, and quantum photonics, etc. In particular, the ability to engineer light-matter interactions at the nanoscale has opened new pathways for controlling optical emission, energy transport, and nonlinear optical phenomena.

A wide variety of optical devices such as light-emitting diodes (LEDs)[1,2], lasers[3,4], and polaritonic devices[5,6], are based on semiconductor active layers embedded within optical microcavities. These microcavities can confine photons within a well-defined optical mode, and when an excitonic transition in the active material is resonant with a cavity photon mode, the two can interact strongly. If the exciton-photon coupling strength exceeds both the photon leakage rate (κ) and the exciton non-radiative decay rate (γ), the system enters the strong-coupling regime, giving rise to hybrid light-matter quasiparticles known as exciton-polaritons.

Exciton-polaritons inherit properties from both their photonic and excitonic constituents, combining an extremely small effective mass with strong nonlinear interactions. These characteristics allow polaritons to exhibit collective quantum phenomena, including macroscopic coherence and condensation. Under appropriate pumping conditions, polaritons can undergo a Bose-Einstein condensation, in which a macroscopic population accumulates in the lowest-energy state with a well-defined momentum, energy, and phase. Unlike conventional photon lasing,

polariton condensation does not require population inversion and can therefore occur at significantly lower thresholds. Such phenomena have enabled studies of superfluidity[7,8], quantized vortices[9,10], as well as the development of low-threshold coherent light sources[11,12].

Exciton-polariton condensation has now been demonstrated across a broad range of material systems, including inorganic III–V semiconductors such as GaAs[13] and II–VI semiconductors such as CdTe[14] and ZnO[15]. While these systems established the foundation of modern polariton physics, condensation in conventional inorganic semiconductor microcavities is typically limited to cryogenic temperatures (e.g. ~ 25 K for GaAs[16] and 110 K for CdTe[17]). This limitation arises primarily from their relatively small exciton binding energies, which allow thermal dissociation of excitons at elevated temperatures and weaken the strong-coupling regime. Consequently, the requirement for low-temperature operation presents a significant challenge for practical polaritonic devices and applications. Subsequent demonstrations of room-temperature polariton condensation in organic materials, including small molecules[18,19], polymers[20,21], and organic microcrystals[22,23], highlighted the importance of large exciton binding energies, but often suffered from limited charge transport and structural disorder.

In recent years, metal halide perovskites have emerged as a promising alternative platform for polariton physics. These materials combine solution-processability with strong optical absorption, high oscillator strengths, and exceptional structural and compositional tunability. Of particular interest are two-dimensional (2D) layered perovskites, which naturally form quantum-well structures with strong quantum and dielectric confinement. As a result, 2D perovskites exhibit large exciton binding energies enabling stable excitons and strong light-matter coupling even at room temperature. However, early demonstrations using solution-processed perovskite thin films were limited by surface roughness, inhomogeneous broadening, low cavity quality factors (Q), and reduced photoluminescence quantum yield. These factors significantly shorten polariton lifetimes

and hinder the accumulation of a macroscopic polariton population, preventing the realization of polariton condensation.[24–26] To date, polariton condensation in 2D perovskite microcavities has only been reported once, in 2020, using high-quality mechanically exfoliated PEAI perovskite flakes embedded within a microcavity operating at cryogenic temperature (4 K).[27]

Against this backdrop, the main objective of this thesis is to investigate strong exciton-photon coupling, exciton and polariton dynamics, and the conditions required for polariton condensation in 2D perovskite microcavities. In particular, this work focuses on the pure 2D perovskite BA_2PbI_4, exploring how film morphology, cavity design, and excitation conditions influence optical gain, relaxation dynamics, and the emergence or absence of collective polaritonic phenomena. A combination of steady-state and time-resolved optical spectroscopy techniques is employed to elucidate the interplay between excitons, polaritons, and optical cavities, and to identify the key physical limitations governing polariton condensation in this material system.

1.1. Thesis Outline

This thesis is organized as follows:

Chapter 2 introduces the theoretical background relevant to this work, including metal halide perovskites, excitons in low-dimensional systems, strong light-matter coupling, and the fundamental physics of exciton-polaritons and polariton condensation.

Chapter 3 describes the experimental methods used throughout the thesis, covering perovskite thin-film fabrication, microcavity design and fabrication, and the characterization techniques employed.

Chapter 4 focuses on the optimization of BA_2PbI_4 thin films and their integration into DBR microcavities, demonstrating the realization of strong exciton-photon coupling through angle-resolved reflectivity and photoluminescence measurements.

Chapter 5 investigates amplified spontaneous emission (ASE) in BA_2PbI_4 thin films and power-dependent photoluminescence in strongly coupled microcavities at low temperatures and attempts to determine whether the signatures of polariton condensation can be identified. It is concluded that under the conditions explored, polaritons do not undergo condensation in BA_2PbI_4 based microcavities.

Chapter 6 employs ultrafast pump-probe spectroscopy to characterise exciton and polariton relaxation dynamics in both bare BA_2PbI_4 films and microcavities, providing insight into the dynamical processes that limit polariton population buildup and condensation.

Chapter 7 summarizes the main findings of this thesis and discusses future directions for achieving polariton lasing and condensation in perovskite-based systems.

1.2. Contributions and Collaborations in This Thesis

The X-ray diffraction (XRD) data for the perovskite films in Chapter 4 were collected by Timothy Thornber.

Time-resolved photoluminescence (TRPL) measurements of the perovskite films and microcavities in Chapter 5 were performed by Dr. Tingxiang Yang (School of Biosciences).

Low-temperature amplified spontaneous emission (ASE) measurements on perovskite films in Chapter 5 were conducted with the assistance of Dr. Peter Claronino and Dr. Kyriacos Georgiou (University of Cyprus).

Low-temperature power-dependent photoluminescence measurements on the microcavities in Chapter 5 were carried out by Dr. Rafal Mirek and Dr. Thilo Stöferle at IBM Research Zurich.

Pump-probe spectroscopy measurements in Chapter 6 were performed at the University of Cyprus by Dr. Emmanouil Lioudakis, Prof. Andreas Othonos, and Dr. Kyriacos Georgiou.

I, the author of this thesis, designed and fabricated all thin films and microcavities presented in this work, and performed the AFM, steady-state absorption, and photoluminescence measurements, including angle-resolved and temperature-dependent measurements. All data presented in this thesis were processed and analysed by the author, with the exception of the low-temperature power-dependent photoluminescence measurements on the microcavities presented in Chapter 5, which were processed by the IBM group.

References

1 Y. Cao, N. Wang, H. Tian, J. Guo, Y. Wei, H. Chen, Y. Miao, W. Zou, K. Pan, Y. He, H. Cao, Y. Ke, M. Xu, Y. Wang, M. Yang, K. Du, Z. Fu, D. Kong, D. Dai, Y. Jin, G. Li, H. Li, Q. Peng, J. Wang, and W. Huang, "Perovskite light-emitting diodes based on spontaneously formed submicrometre-scale structures," Nature 562(7726), 249–253 (2018).

2 K. Lin, J. Xing, L.N. Quan, F.P.G. de Arquer, X. Gong, J. Lu, L. Xie, W. Zhao, D. Zhang, C. Yan, W. Li, X. Liu, Y. Lu, J. Kirman, E.H. Sargent, Q. Xiong, and Z. Wei, "Perovskite light-emitting diodes with external quantum efficiency exceeding 20 per cent," Nature 562(7726), 245–248 (2018).

3 S.W. Eaton, M. Lai, N.A. Gibson, A.B. Wong, L. Dou, J. Ma, L.-W. Wang, S.R. Leone, and P. Yang, "Lasing in robust cesium lead halide perovskite nanowires," Proceedings of the National Academy of Sciences 113(8), 1993–1998 (2016).

4 H. Zhu, Y. Fu, F. Meng, X. Wu, Z. Gong, Q. Ding, M.V. Gustafsson, M.T. Trinh, S. Jin, and X.-Y. Zhu, "Lead halide perovskite nanowire lasers with low lasing thresholds and high quality factors," Nature Mater 14(6), 636–642 (2015).

5 T.C.H. Liew, I.A. Shelykh, and G. Malpuech, "Polaritonic devices," Physica E: Low-Dimensional Systems and Nanostructures 43(9), 1543–1568 (2011).

6 D. Sanvitto, and S. Kéna-Cohen, "The road towards polaritonic devices," Nature Mater 15(10), 1061–1073 (2016).

7 A. Amo, J. Lefrere, S. Pigeon, C. Adrados, C. Ciuti, I. Carusotto, R. Houdre, E. Giacobino, and A. Bramati, "Observation of Superfluidity of Polaritons in Semiconductor Microcavities," Nature Phys 5(11), 805–810 (2009).

8 A. Amo, D. Sanvitto, F.P. Laussy, D. Ballarini, E. del Valle, M.D. Martin, A. Lemaître, J. Bloch, D.N. Krizhanovskii, M.S. Skolnick, C. Tejedor, and L. Viña, "Collective fluid dynamics of a polariton condensate in a semiconductor microcavity," Nature 457(7227), 291–295 (2009).

9 D. Sanvitto, F.M. Marchetti, M.H. Szymańska, G. Tosi, M. Baudisch, F.P. Laussy, D.N. Krizhanovskii, M.S. Skolnick, L. Marrucci, A. Lemaître, J. Bloch, C. Tejedor, and L. Viña, "Persistent currents and quantized vortices in a polariton superfluid," Nature Phys 6(7), 527–533 (2010).

10 K.G. Lagoudakis, M. Wouters, M. Richard, A. Baas, I. Carusotto, R. André, L.S. Dang, and B. Deveaud-Plédran, "Quantized vortices in an exciton–polariton condensate," Nature Phys 4(9), 706–710 (2008).

11 C. Schneider, A. Rahimi-Iman, N.Y. Kim, J. Fischer, I.G. Savenko, M. Amthor, M. Lermer, A. Wolf, L. Worschech, V.D. Kulakovskii, I.A. Shelykh, M. Kamp, S. Reitzenstein, A. Forchel, Y. Yamamoto, and S. Höfling, "An electrically pumped polariton laser," Nature 497(7449), 348–352 (2013).

12 H. Deng, G. Weihs, D. Snoke, J. Bloch, and Y. Yamamoto, "Polariton lasing vs. photon lasing in a semiconductor microcavity," Proceedings of the National Academy of Sciences 100(26), 15318–15323 (2003).

13 D. Bajoni, P. Senellart, A. Lemaître, and J. Bloch, "Photon lasing in GaAs microcavity: Similarities with a polariton condensate," Phys. Rev. B 76(20), 201305 (2007).

14 M. Richard, "Spontaneous Coherent Phase Transition of Polaritons in CdTe Microcavities," Phys. Rev. Lett. 94(18), (2005).

15 F. Li, L. Orosz, O. Kamoun, S. Bouchoule, C. Brimont, P. Disseix, T. Guillet, X. Lafosse, M. Leroux, J. Leymarie, M. Mexis, M. Mihailovic, G. Patriarche, F. Réveret, D. Solnyshkov, J. Zuniga-Perez, and G. Malpuech, "From Excitonic to Photonic Polariton Condensate in a ZnO-Based Microcavity," Phys. Rev. Lett. 110(19), 196406 (2013).

16 J. Kasprzak, M. Richard, S. Kundermann, A. Baas, P. Jeambrun, J.M.J. Keeling, F.M. Marchetti, M.H. Szymańska, R. André, J.L. Staehli, V. Savona, P.B. Littlewood, B. Deveaud, and L.S. Dang, "Bose–Einstein condensation of exciton polaritons," Nature 443(7110), 409–414 (2006).

17 D. Ballarini, M. De Giorgi, E. Cancellieri, R. Houdré, E. Giacobino, R. Cingolani, A. Bramati, G. Gigli, and D. Sanvitto, "All-optical polariton transistor," Nat Commun 4(1), 1778 (2013).

18 J. Tang, J. Zhang, Y. Lv, H. Wang, F.F. Xu, C. Zhang, L. Sun, J. Yao, and Y.S. Zhao, "Room temperature exciton–polariton Bose–Einstein condensation in organic single-crystal microribbon cavities," Nat Commun 12(1), 3265 (2021).

19 K.S. Daskalakis, S.A. Maier, R. Murray, and S. Kéna-Cohen, "Nonlinear interactions in an organic polariton condensate," Nat Mater 13(3), 271–278 (2014).

20 M. Dusel, S. Betzold, O.A. Egorov, S. Klembt, J. Ohmer, U. Fischer, S. Höfling, and C. Schneider, "Room temperature organic exciton–polariton condensate in a lattice," Nat Commun 11(1), 2863 (2020).

21 S.K. Rajendran, M. Wei, H. Ohadi, A. Ruseckas, G.A. Turnbull, and I.D.W. Samuel, "Low threshold polariton lasing from a solution-processed organic semiconductor in a planar microcavity," Advanced Optical Materials 7(12), 1–7 (2019).

22 S. Kéna-Cohen, and S.R. Forrest, “Room-temperature polariton lasing in an organic single-crystal microcavity,” Nature Photon 4(6), 371–375 (2010).

23 J. Ren, Q. Liao, H. Huang, Y. Li, T. Gao, X. Ma, S. Schumacher, J. Yao, S. Bai, and H. Fu, “Efficient Bosonic Condensation of Exciton Polaritons in an H-Aggregate Organic Single-Crystal Microcavity,” Nano Lett. 20(10), 7550–7557 (2020).

24 A. Brehier, R. Parashkov, J.S. Lauret, and E. Deleporte, “Strong exciton-photon coupling in a microcavity containing layered perovskite semiconductors,” Appl. Phys. Lett. 89(17), 171110 (2006).

25 T. Fujita, Y. Sato, T. Kuitani, and T. Ishihara, “Tunable polariton absorption of distributed feedback microcavities at room temperature,” Phys. Rev. B 57(19), 12428–12434 (1998).

26 M. Laitz, A.E.K. Kaplan, J. Deschamps, U. Barotov, A.H. Proppe, I. García-Benito, A. Osherov, G. Grancini, D.W. deQuilettes, K.A. Nelson, M.G. Bawendi, and V. Bulović, “Uncovering temperature-dependent exciton-polariton relaxation mechanisms in hybrid organic-inorganic perovskites,” Nat Commun 14(1), 2426 (2023).

27 L. Polimeno, A. Fieramosca, G. Lerario, M. Cinquino, M. De Giorgi, D. Ballarini, F. Todisco, L. Dominici, V. Ardizzone, M. Pugliese, C.T. Prontera, V. Maiorano, G. Gigli, L. De Marco, and D. Sanvitto, “Observation of Two Thresholds Leading to Polariton Condensation in 2D Hybrid Perovskites,” Advanced Optical Materials 8(16), 2000176 (2020).

Chapter 2

Background Theory

In this chapter, the theory relevant to the experimental results chapters is presented. The chapter begins with a brief background on metal halide perovskites and a summary of properties that are special to two-dimensional layered perovskites. In the end of the chapter, exciton-polaritons and microcavity concepts used throughout this thesis are detailed.

2.1. Metal Halide Perovskites Semiconductors

Metal halide perovskites (MHPs) have emerged over the past decade as a prominent class of semiconductor materials owing to their exceptional optoelectronic properties, including long carrier diffusion lengths, low trap-state densities, and strong light absorption.[1,2] These characteristics have enabled rapid progress in a wide range of optoelectronic applications, such as photovoltaics[3,4], light-emitting diodes[5,6], photodetectors[7,8] , and lasers[9,10].

The most extensively studied perovskites are three-dimensional (3D) MHPs, which ideally exhibit the ABX_3 crystal structure, as illustrated in **Figure 2.1**. In this structure, corner-sharing BX_6^{4-} octahedra form a three-dimensional network, with the A-site cation occupying the cavities between octahedra. The A-site is typically a monovalent cation, such as methylammonium (MA^+), formamidinium (FA^+), or inorganic alkali metal ions (e.g., Cs^+, Rb^+). The B-site is commonly occupied by a divalent metal cation, most frequently Pb^{2+}, while X represents a halide anion (Cl^-, Br^-, or I^-). The rigid framework of the 3D lattice imposes constraints on compositional and

structural tunability, as large organic cations cannot be accommodated within the ABX_3 structure. This limitation naturally leads to the formation of lower-dimensional metal halide perovskites when bulky organic spacer cations are introduced.

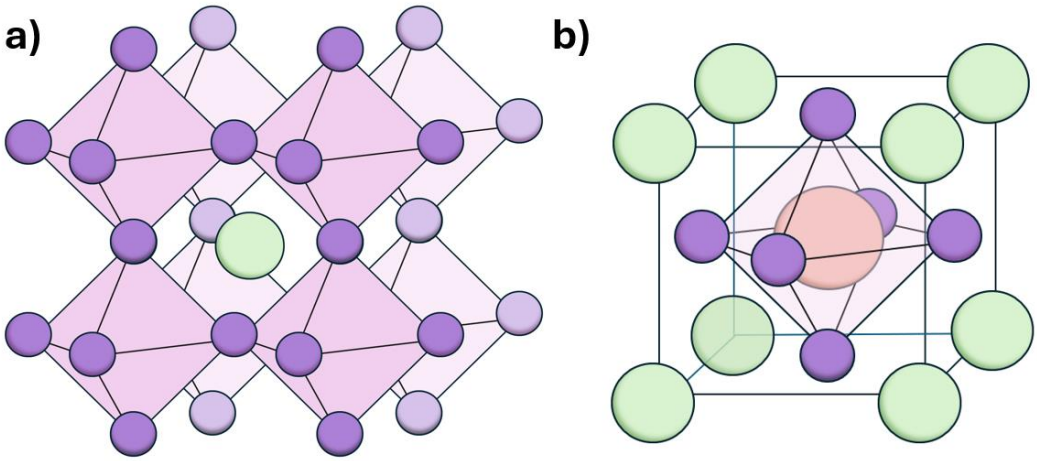

Figure 2.1 a) *Crystal structure where BX_6^{4-} octahedra occupying the corner spaces surrounding an A cation. A, B cations and X anions are shown as green, purple, and pink, respectively.* ***b)*** *Equivalent unit cell ABX_3 structure of a 3D perovskite.*

2.1.1. Two-dimensional (2D) layered perovskites

Two-dimensional (2D) metal halide perovskites can be conceptually derived by slicing the 3D ABX_3 lattice along crystallographic planes perpendicular to the ⟨100⟩, ⟨110⟩, or ⟨111⟩ directions, resulting in layered perovskite sheets belonging to distinct structural families. These inorganic sheets can stack periodically, separated by organic spacer layers, to form bulk layered crystals, as schematically shown in **Figure 2.2**.

Among the various 2D perovskite families, the Ruddlesden-Popper (RP) phase is the most widely studied. RP perovskites follow the general chemical formula $A'_2A_{n-1}B_nX_{3n+1}$, where A′ is a bulky

organic ammonium cation (most commonly butylammonium (BA^+) or phenylethylammonium (PEA^+)[11]) that cannot fit into the 3D perovskite lattice. The introduction of these large organic cations interrupts the three-dimensional connectivity of the inorganic framework, leading to the formation of a naturally layered structure composed of n sheets of corner-sharing BX_6^{4-} octahedra separated by organic barriers. Here, *n* denotes the number of inorganic octahedral layers within each perovskite slab. This layered architecture endows 2D perovskites with significantly greater structural and compositional freedom compared to their 3D counterparts, enabling tunable electronic and optical properties through control of composition, layer thickness, and organic spacer chemistry[12,13].

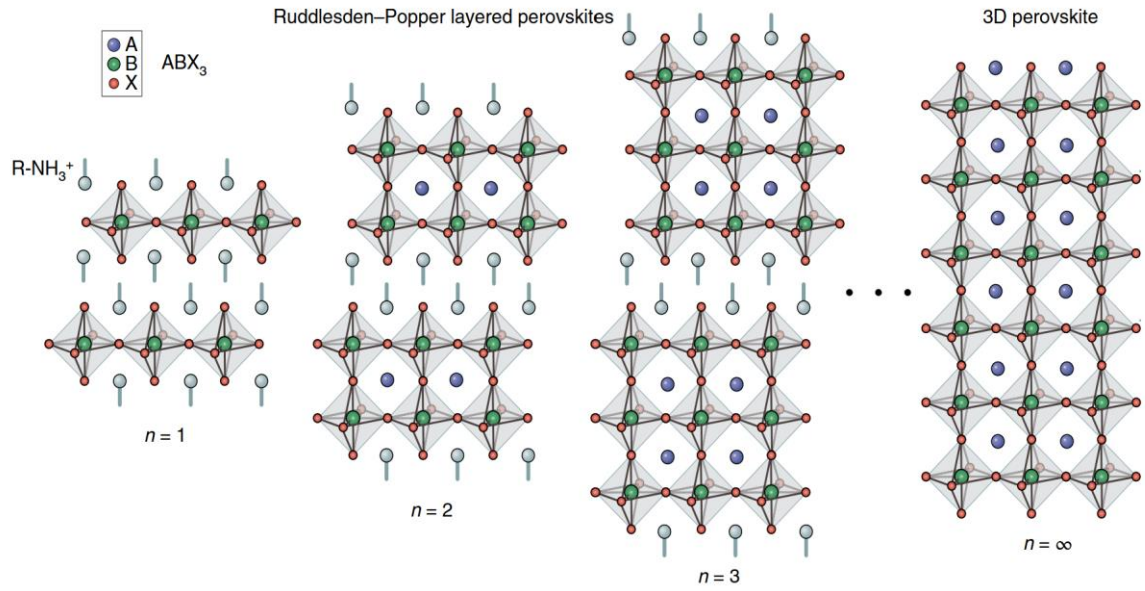

Figure 2.2 *Schematic structure of 2D MHPs. The structure of RP phase can be described as a stacked mono (n = 1) or multiple (n > 1) atomic layers of metal-halide octahedra separated by large organic cations. Here, A is cation; B is metal divalent cation; X is halide anion; and R-NH3 is organic cation.*[14]

2.2. Electronic Band Structure of Metal Halide Perovskites

The optoelectronic properties of MHPs are fundamentally governed by their electronic band structure, which determines the bandgap, charge-carrier effective masses, and excitonic interactions. In these materials, the band structure arises primarily from hybridization between the metal and halide atomic orbitals within the corner-sharing BX_6 octahedral framework, which has a mixed ionic-covalent character.

In lead-based perovskites, for example $APbI_3$, the electronic configurations of Pb^{2+} and I^- are $5d^{10}6s^26p^0$ and $5s^25p^6$, respectively. Because the Pb 6s and I 5p orbitals are energetically well aligned, they interact strongly and hybridize to form bonding and antibonding states.[15] The higher-energy antibonding Pb 6s - I 5p state constitutes the valence band maximum (VBM). This antibonding character shifts the VBM toward higher energies, effectively narrowing the bandgap, and plays a crucial role in their optoelectronic behavior. In particular, it contributes to the small electrons effective mass[16], high defect tolerance[17] and strong optical absorption commonly observed in lead halide perovskites.

The conduction band minimum (CBM), by contrast, is dominated by Pb 6p states with only a minor halide contribution. Owing to the large energy separation between the Pb 6p and I 5p orbitals, their hybridization is comparatively weak, and the CBM retains a predominantly metal-p character[15]. This clear separation between the orbital origins of the valence and conduction bands underpins the direct bandgap nature of lead halide perovskites.

2.2.1. Defects/Trap States

Real MHPs inevitably deviate from an ideal crystalline structure due to intrinsic lattice imperfections and stoichiometric fluctuations. These imperfections are commonly classified as defects, with the term so called point defects. Point defects include i) *vacancies*, where an atom or ion is absent from its lattice site; ii) *substitutions*, in which an atom occupies an incorrect lattice site; and iii) *interstitials*, where an extra atom or ion occupies a non-lattice position, as shown in **Figure 2.3**. In addition to point defects, extended defects such as dislocations, stacking faults, and grain boundaries are frequently observed in polycrystalline perovskite thin films, particularly in solution-processed materials.[18]

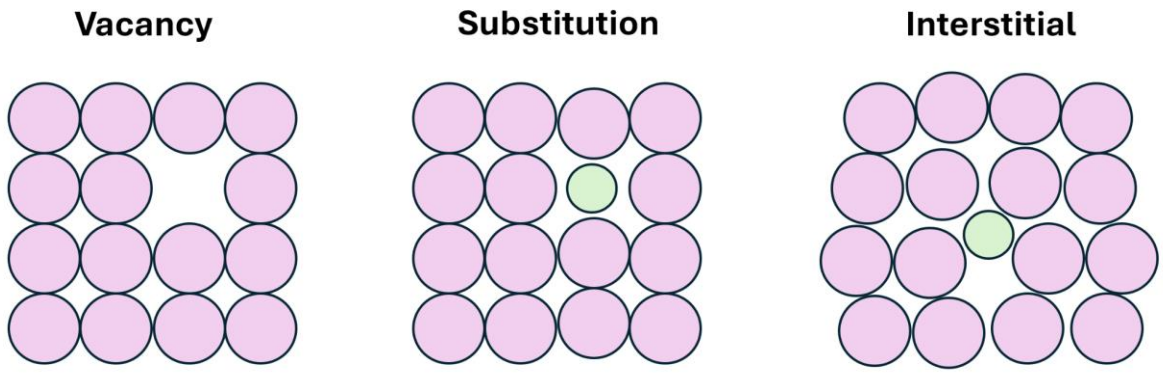

Figure 2.3 *Three typical types of point defects in crystals: vacancies, substitutions, and interstitials. Pink is the original atom in the lattice while green represents the external atom or impurity.*

In MHPs, certain defects can introduce localized electronic states within the bandgap. These states may act as non-radiative recombination centres, capturing charge carriers and locally reducing the effective bandgap. Such defect-induced states are therefore commonly referred to as trap states, and they play a crucial role in governing carrier lifetime, transport, and photoluminescence efficiency.

Notably, lead halide perovskites exhibit a significant degree of defect tolerance compared to conventional inorganic semiconductors. Owing to the antibonding character of the VBM as we discussed before, many intrinsic defects in Pb-halide perovskites form shallow energy levels rather than deep traps. This defect tolerance contributes to the relatively long carrier lifetimes and high optical quality, although deep trap states associated with extended defects and surface imperfections can still significantly impact optoelectronic performance.[19]

2.2.2. Excitons in 2D Layered Perovskites

An exciton is a quasiparticle formed from a coulombically bound electron-hole pair. The energy required to dissociate an exciton into free charge carriers is defined as the exciton binding energy (E_b). Excitons play a central role in determining the optical response of MHPs, and their properties in 2D systems differ fundamentally from those in 3D counterparts.

In 3D MHPs, the exciton binding energy is relatively small. This arises from the continuous corner-sharing Pb-I octahedral network, which provides strong electrostatic screening and results in a large relative dielectric constant (ε_r). Within a simple hydrogenic model, the exciton binding energy scales inversely with the dielectric constant and the electron-hole separation d_{e-h}, as expressed by

$$E_b = \frac{e^2}{4\pi \cdot \varepsilon_0 \cdot \varepsilon_r \cdot d_{e-h}} \tag{2.1}$$

Consequently, excitons in 3D perovskites are weakly bound and readily dissociate into free carriers at room temperature, giving rise to free-carrier dominated optoelectronic behavior.

In contrast, 2D perovskites consist of atomically thin inorganic Pb-I layers separated by bulky organic spacer cations, which disrupt the continuous ionic-covalent Pb-I framework present in 3D structures. As illustrated in **Figure 2.4**, the inorganic Pb-I slabs act as quantum wells of thickness *d*, while the organic layers form wide-bandgap potential barriers of thickness *L* with a lower dielectric constant ($\varepsilon_2 < \varepsilon_1$). This structural anisotropy leads to strong quantum confinement of charge carriers within the inorganic layers, increasing the separation between VBM and CBM and thereby widening the effective bandgap (E_g) relative to 3D perovskites. As the number of inorganic layers (n) increases, the strength of quantum confinement is progressively reduced, resulting in a narrowing of the optical bandgap and a gradual transition toward bulk-like electronic behavior.

In addition to quantum confinement, dielectric confinement plays a crucial role in 2D perovskites. The pronounced dielectric mismatch between the high-ε_1 inorganic layers and the low-ε_2 organic spacers significantly enhances the Coulomb interaction between electrons and holes. As a result, excitons in 2D perovskites exhibit markedly increased binding energies, often reaching several hundred meV.[20,21] This enhanced binding stabilizes excitons against thermal dissociation (k_BT) and gives rise to strong excitonic absorption features and pronounced resonances that persist even at room temperature. The combined effects of quantum and dielectric confinement thus underpin the exceptional excitonic properties of 2D perovskites, making them highly attractive for studies of strong light-matter coupling and polaritonic phenomena.

Many studies of low-dimensional halide perovskites have focused on monolayered structures with n = 1, corresponding to compounds of the form A'_2BX_4, where A′ is typically a long-chain, non-conjugated primary ammonium cation ($R\text{-}NH_3^+$). These single-layer perovskites represent an ideal platform for investigating fundamental excitonic phenomena, dimensional confinement, and strong light-matter interaction in hybrid organic-inorganic systems. Their appeal arises from the

well-defined quantum-well architecture formed by atomically thin inorganic layers separated by organic spacer cations, as well as their self-assembled and vertically ordered crystal structure.[22–26]

In this thesis, we focus on a prototypical pure-phase n = 1 2D perovskite, butylammonium lead iodide (BA_2PbI_4), in which the organic spacer cation is butylammonium ($CH_3CH_2CH_2CH_2\text{-}NH_3^+$). Owing to its strong excitonic response, large binding energy, and structural simplicity, BA_2PbI_4 serves as an ideal model system for studying strong light-matter coupling, optical gain, and exciton-polariton dynamics in perovskite microcavities.

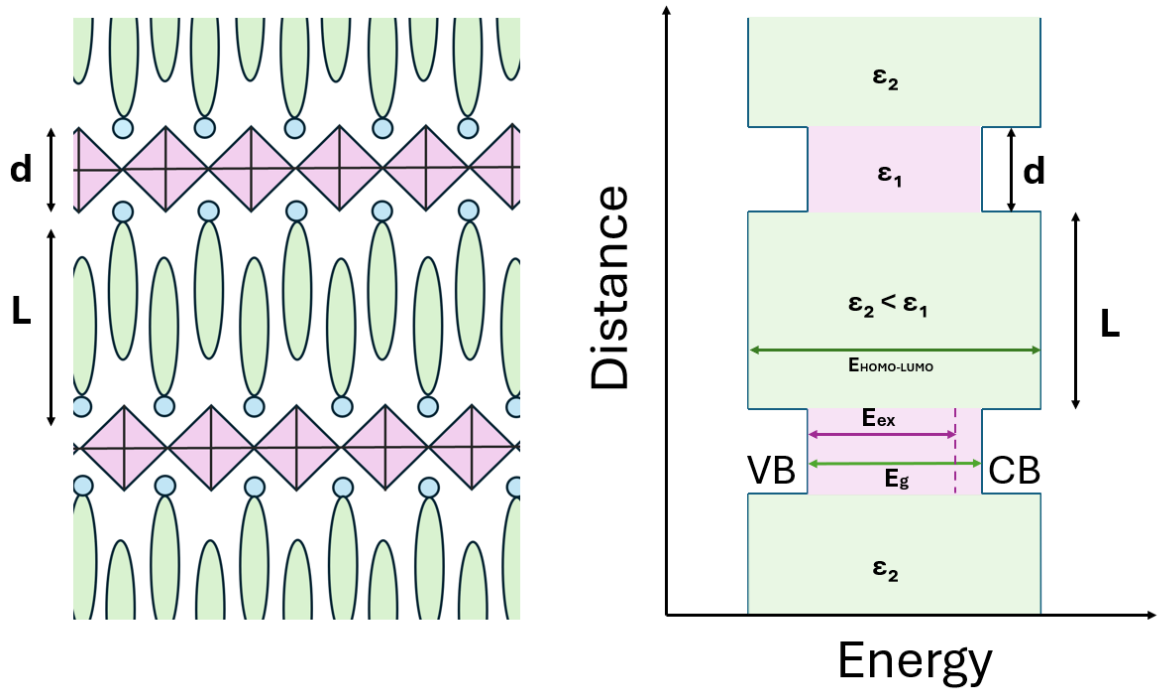

Figure 2.4 *Quantum-well structure and dielectric confinement in 2D perovskites.* ***Left:*** *Schematic crystal structure of a layered 2D perovskite, where thin inorganic Pb-I sheets of thickness d are separated by bulky organic spacer layers of thickness L.* ***Right:*** *Corresponding energy-band diagram illustrating quantum and dielectric confinement. The inorganic layer forms a quantum well between low-dielectric organic barriers ($\varepsilon_2 < \varepsilon_1$), leading to an increased E_g and enhanced E_b.*

2.3. Direct Bandgap and Optical Transitions

2.3.1. Absorption

Optical absorption in a semiconductor occurs when an incident photon with energy equal to or exceeding the bandgap promotes an electron from the valence band (VB) to the conduction band (CB). Unlike isolated atoms, where optical transitions occur between discrete energy levels, solids exhibit continuous energy bands due to a range of energy states within. As a result, interband optical transitions give rise to broadband absorption spectra rather than sharp atomic lines. The absorption process generates an electron-hole pair, which may exist either as free carriers or as a bound exciton, depending on the strength of Coulomb interactions.

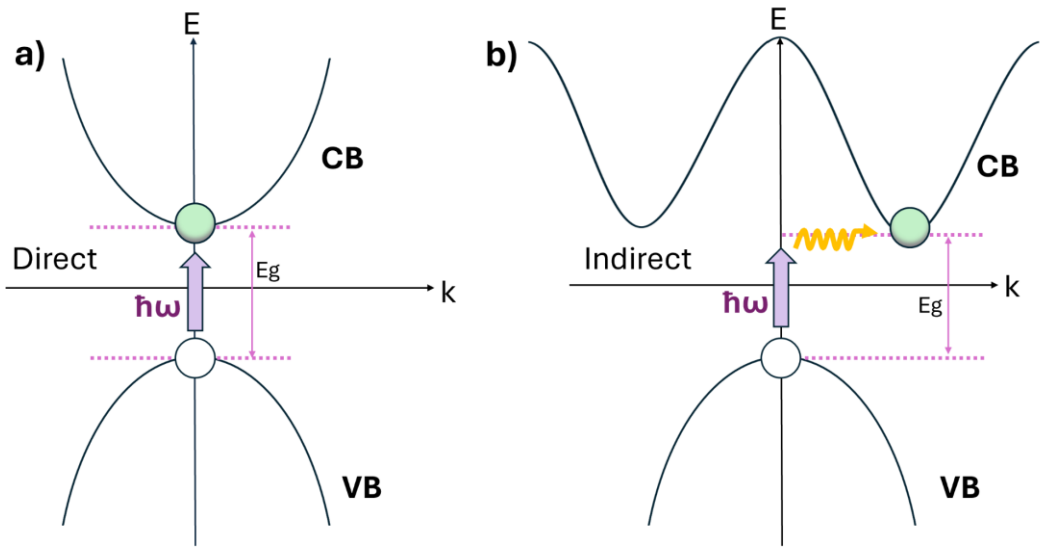

Figure 2.5 *Absorption transition in* ***a)*** *direct and* ***b)*** *indirect bandgap semiconductors.*

Semiconductors are commonly classified as direct or indirect bandgap materials according to the relative momentum of the VBM and CBM. In direct bandgap materials, both VBM and CBM are located at the Brillouin-zone center (k = 0), allowing vertical optical transitions that conserve crystal momentum (see **Figure 2.5a**). In contrast, indirect bandgap materials require phonon assistance to satisfy momentum conservation, resulting in weaker optical absorption near the band edge (see **Figure 2.5b**). MHPs are direct bandgap semiconductors, with band extrema located at or near k = 0. Consequently, optical absorption in MHPs is highly efficient, particularly close to the band edge.

A quantitative description of light absorption is given by the absorption coefficient α(hω), which describes the exponential attenuation of light intensity as it propagates through a material according to the Beer-Lambert law:

$$I(z) = I_0 \cdot e^{-\alpha(h\omega)z} \tag{2.2}$$

where I_0 is the incident intensity, hω is the photon energy, and z is the propagation distance.

However, in materials with strong Coulomb interactions, optical absorption cannot be described solely by free electron-hole transitions across the bandgap. Instead, the Coulomb attraction between electrons and holes leads to the formation of excitons, which manifest as discrete resonances below the bandgap energy. This effect is especially pronounced in 2D perovskites. The energy of the lowest excitonic transition is given by:

$$E_{ex} = E_g - E_b \tag{2.3}$$

where E_b is the exciton binding energy. As discussed in Section 2.2, 2D perovskites exhibit significantly enhanced exciton binding energies due to the combined effects of quantum

confinement and dielectric confinement. Consequently, excitonic absorption peaks appear well below the continuum band edge and dominate the optical spectra even at room temperature.

2.3.2. Photoluminacence and Recombinations

Upon optical excitation, materials absorbing photons with energies exceeding the bandgap generate excited states in the form of excitons or free charge carriers occupying the CB and VB. These excited species subsequently relax toward equilibrium through a variety of recombination pathways. Photoluminescence (PL) refers to all radiative recombination processes that result in the emission of photons with energies close to the optical bandgap.

For an ensemble of excited species with population n(t), the time evolution of the PL intensity following pulsed excitation is proportional to the decay of this population ($I(t) \propto n(t)$). If the dominant recombination process is monomolecular, the population decay follows first-order kinetics:

$$\frac{dn}{dt} = -kn \tag{2.4}$$

with the solution of:

$$n(t) = n_0 \cdot e^{-kt} \tag{2.5}$$

And this is leading to an exponential PL decay:

$$I(t) = I_0 \cdot e^{-kt} = I_0 \cdot e^{-\frac{t}{\tau}} \tag{2.6}$$

where I_0 is the initial emission intensity, k = 1/τ is the total recombination rate, and τ is the effective PL lifetime. The total recombination rate is given by the sum of radiative and non-radiative contributions:

$$k = k_{rad} + k_{non-rad} \quad (2.7)$$

The following sections will discuss all recombination processes relevant for this thesis.

2.3.3. Mono-molecular Recombination

Monomolecular recombination is characterized by recombination rates that scale linearly with the population of excited states. These processes dominate at low excitation densities and are particularly relevant in excitonic materials such as 2D perovskites.

2.3.3.1. Excitonic Recombination

In 2D perovskites, strong quantum and dielectric confinement stabilizes excitons with large binding energies. Once formed, an exciton behaves as a single quasiparticle, and its recombination can be described by a first-order rate equation:

$$\frac{dn_{ex}}{dt} = -k_1 n_{ex} \quad (2.8)$$

where n_{ex} is the exciton population and $k_1 = 1/\tau_{ex}$ is the excitonic recombination rate. Radiative excitonic recombination results in photon emission and dominates the PL of 2D perovskites[27].

2.3.3.2. Trap-assisted Recombination

Trap-assisted non-radiative recombination is another monomolecular decay pathway, in which carriers or excitons are captured by localized defect states within the bandgap as we discussed in section 2.2.1. This process can be described by:

$$\frac{dn}{dt} = -k_{trap}n \tag{2.9}$$

where k_{trap} is the trap-assisted recombination rate. In solution-processed 2D perovskite films, trap-assisted recombination could be enhanced due to grain boundaries, surface defects, and organic-inorganic interfaces[28,29].

2.3.4. Bi-molecular Recombination

Bimolecular recombination processes involve interactions between two excited species and therefore scale quadratically with excitation density. These mechanisms become increasingly important at higher carrier or exciton densities.

2.3.4.1. Free-carrier Recombination

In systems where free electrons and holes coexist, radiative recombination across the bandgap follows second-order kinetics:

$$\frac{dn_e}{dt} = \frac{dn_h}{dt} = -k_2 n_e n_h \tag{2.10}$$

where k_2 is the bimolecular recombination coefficient, and n_e and n_h are the electron and hole densities, respectively. In strongly excitonic 2D perovskites, this mechanism is typically suppressed due to rapid exciton formation.[27]

2.3.4.2. Exciton-Exciton Annihilation

At higher excitation densities, exciton-exciton annihilation (EEA) becomes an important non-radiative loss channel. In this process, two excitons interact, resulting in the non-radiative recombination of one exciton while transferring energy to the other. The annihilation rate scales as:

$$\frac{dn_{ex}}{dt} = -k_{EEA}{n_{ex}}^2 \tag{2.11}$$

where k_{EEA} is the exciton-exciton annihilation coefficient. EEA leads to PL saturation and a reduction in effective lifetime at higher fluences.

2.4. Optical microcavities

Before introducing exciton-polaritons, it is first necessary to define an optical microcavity, which provides the essential photonic confinement required for the strong light-matter coupling regime. Optical microcavities are structures designed to confine photons in a small volume, thereby enhancing their interaction with embedded electronic or excitonic states.

One of the most common types of optical microcavity is the Fabry-Pérot resonator, which consists of two parallel, highly reflective mirrors separated by an active spacer layer. The total cavity

thickness is typically on the order of a micrometre or less. At least one of the mirrors is partially transparent, allowing photons to enter and exit the cavity. Multiple reflections between the mirrors give rise to constructive interference, forming standing electromagnetic waves perpendicular to the mirror surfaces.

2.4.1. Distributed Bragg Reflectors

Highly reflective mirrors used in a microcavity to achieve optical confinement commonly include metallic reflectors such as silver (Ag) and aluminum (Al), as well as dielectric Distributed Bragg Reflectors (DBRs). In this thesis, dielectric DBRs are employed as both the top and bottom mirrors of the microcavities.

DBRs consist of alternating layers of high- and low-refractive-index dielectric materials, each with an optical thickness of one quarter of a target wavelength. The geometrical thickness of each layer $d_i = \lambda_0/4n_i$, where λ_0 is the design (central) wavelength and n_i is the refractive index of the dielectric layers. This quarter-wave condition ensures that reflections from each interface acquire the same phase, leading to constructive interference for reflected light. As incident light propagates through the periodic refractive-index modulation, partial reflections occur at each interface between the high-index (n_H) and low-index (n_L) layers. When the Bragg condition is satisfied, these reflected waves interfere constructively, resulting in very high reflectivity over a finite spectral range known as the photonic stopband (**Figure 2.6a**). The central wavelength of the stopband is directly determined by the layer thicknesses via $\lambda_0 = 4dn_i$, allowing straightforward spectral tuning of the mirror by adjusting the deposited layer thicknesses.

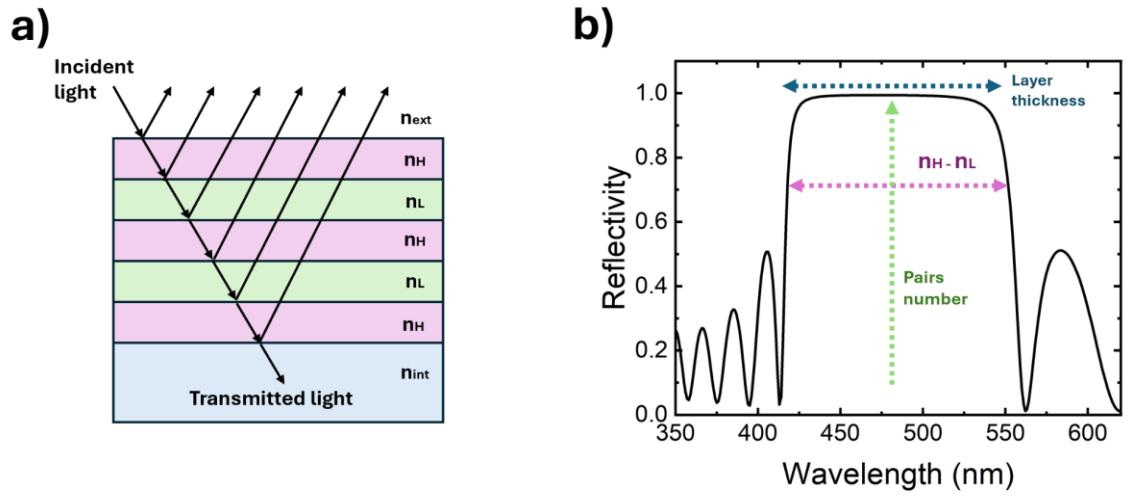

Figure 2.6 a) *Multiple-interface interference in a quarter-wave DBR and* ***b)*** *calculated reflectivity spectrum illustrating the stopband dependence on refractive-index contrast, layer thickness, and number of layer pairs.*

The peak reflectivity within the stopband depends strongly on both the refractive-index contrast (n_H- n_L). and the number of layer pairs *N*. For a DBR composed of *N* alternating pairs of high- and low-index layers, the reflectivity at normal incidence can be approximated by[30]

$$R = 1 - 4\frac{n_{ext}}{n_{int}}\left(\frac{n_L}{n_H}\right)^{2N} \tag{2.12}$$

where n_H and n_L are the high and low refractive index of dielectric layers, n_{ext} is the refractive index of the external medium (typically air), and n_{int} is the refractive index of the internal medium (such as substrate or active layer). *N* represents the number of dielectric material pairs. Since n_L/n_H < 1, the reflectivity increases exponentially with the number of layer pairs and with increasing refractive-index contrast (n_H- n_L). As a result, DBRs can readily achieve reflectivities exceeding 99% using a sufficient number of dielectric pairs, making them highly suitable for optical microcavities requiring strong photon confinement.

In addition to peak reflectivity, the spectral width of the stopband ($\Delta\lambda_{SB}$) is another key parameter governing DBR performance. The stopband width is determined primarily by the refractive-index contrast (n_H- n_L) and is given by[31]

$$\Delta\lambda_{SB} = \frac{4\lambda_0}{\pi} sin^{-1}(\frac{n_H - n_L}{n_H + n_L}) \quad (2.13)$$

indicating that a larger refractive-index mismatch produces a broader stopband (**Figure 2.6b**). A wide stopband is particularly advantageous for microcavity applications, as it ensures strong optical confinement over a broad spectral and angular range.

The high reflectivity and broad stopband provided by DBRs enable long photon lifetimes when used as cavity mirrors, forming the basis for high-quality-factor optical microcavities.

2.4.2. Fabry-Pérot Microcavity

A Fabry-Pérot cavity consists of an optical spacer (active layer) sandwiched between two highly reflective mirrors (DBRs in our work). The effective optical length of the cavity is not only determined by the physical thickness of the spacer layer, but also by the finite electromagnetic field penetration into the DBR mirrors. The total effective cavity length can therefore be written as:

$$L_{eff} = d_{DBR} + d_c \quad (2.14)$$

where d_c is the thickness of the active layer and d_{DBR} is the penetration depth of the optical field into a single DBR mirror. For a quarter-wave DBR, the penetration depth can be approximated as[30]

$$d_{DBR} = \frac{\lambda}{2n_c}\frac{n_H n_L}{n_H - n_L} \tag{2.15}$$

where λ is the cavity resonance wavelength, n_c is the refractive index of the cavity spacer layer, and n_H and n_L are the refractive indices of the high- and low-index DBR materials, respectively.

Constructive interference within the cavity requires that the optical phase accumulated during a round trip corresponds to an integer multiple of 2π. This leads to the standing-wave condition:

$$d_c = m\frac{\lambda}{2n_c} \tag{2.16}$$

where m = 1,2, 3… is the longitudinal mode index (**Figure 2.7**). Each integer value of m corresponds to a distinct cavity mode, allowing multiple resonant modes to be supported within a single cavity depending on its thickness. In this thesis, the cavity thickness is chosen as m = 1 to spectrally overlap with the excitonic resonance of the perovskite active layer.

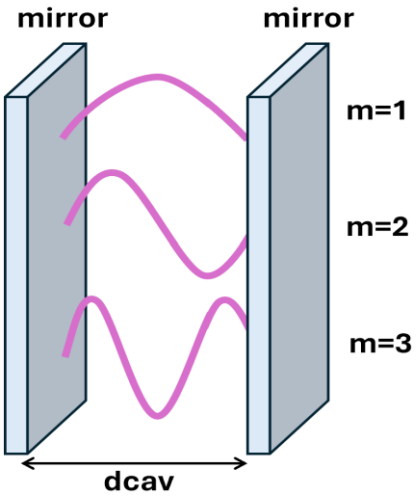

Figure 2.7 *Standing-wave resonant modes in a Fabry-Pérot microcavity, m is longitudinal cavity modes.*

A commonly used metric to quantify optical confinement in a microcavity is the quality factor, or Q-factor. The Q-factor characterizes the spectral sharpness and energy storage capability of a specific cavity mode and is defined as:

$$Q = \frac{\omega}{\Delta\omega} = \frac{\lambda}{\Delta\lambda} \tag{2.17}$$

where ω and Δω are the angular frequency of the cavity mode and its full width at half maximum (FWHM) in frequency space, respectively, and λ and Δλ are the corresponding quantities expressed in wavelength space. The quality factor is directly related to the photon lifetime τ_{ph}, which quantifies the average time a photon remains confined within the cavity before being lost through leakage, absorption, or scattering. This relationship is given by:

$$\tau_{ph} = \frac{Q}{\omega} = \frac{Q\lambda}{2\pi c} \tag{2.18}$$

where ω is the angular frequency of the cavity mode, λ is the resonance wavelength, and c is the speed of light. A higher Q-factor therefore corresponds to a longer photon lifetime and increased electromagnetic field buildup inside the cavity.

2.4.3. Cavity Photon Dispersion and Angle Dependence

In a planar Fabry-Pérot microcavity, optical confinement occurs only along the growth (vertical) direction, while photons remain free to propagate in the plane of the cavity. As a result, the cavity photon modes exhibit a 2D dispersion relation, and in this case the total photon wavevector inside the cavity can be written as:

$$k_{tot} = k_{\perp} + k_{\parallel} \tag{2.19}$$

where $k_\perp$ is the wavevector component perpendicular to the cavity plane and $k_\parallel$ is the in-plane (parallel) wavevector, as illustrated in **Figure 2.8a**. The perpendicular component is quantized by the cavity boundary conditions and is given by:

$$k_\perp = \frac{\pi m}{d_c} \tag{2.20}$$

where m is the longitudinal cavity mode index, and d_c is the cavity thickness.

The photon energy inside the cavity can then be expressed as:

$$E_c(k_\parallel) = \frac{\hbar c}{n_c}\sqrt{{k_\perp}^2 + {k_\parallel}^2} \tag{2.21}$$

At normal incidence ($k_\parallel$=0), this reduces to the cavity resonance energy:

$$E_0 = \hbar c \frac{k_\perp}{n_c} = \frac{hc}{2n_c d_c} m \tag{2.22}$$

For small in-plane wavevectors ($k_\parallel \ll k_\perp$), the dispersion can be approximated by a parabolic form:

$$E_c(k_\parallel) \approx E_0 + \frac{\hbar^2 {k_\parallel}^2}{2m_{ph}} \tag{2.23}$$

where the effective photon mass m_{ph} is given by:

$$m_{ph} = \frac{\hbar k_\perp n_c}{c} \tag{2.24}$$

This extremely small effective mass ($\sim 10^{-5}\, m_e$) is a defining feature of cavity photons and, later, of exciton-polaritons.

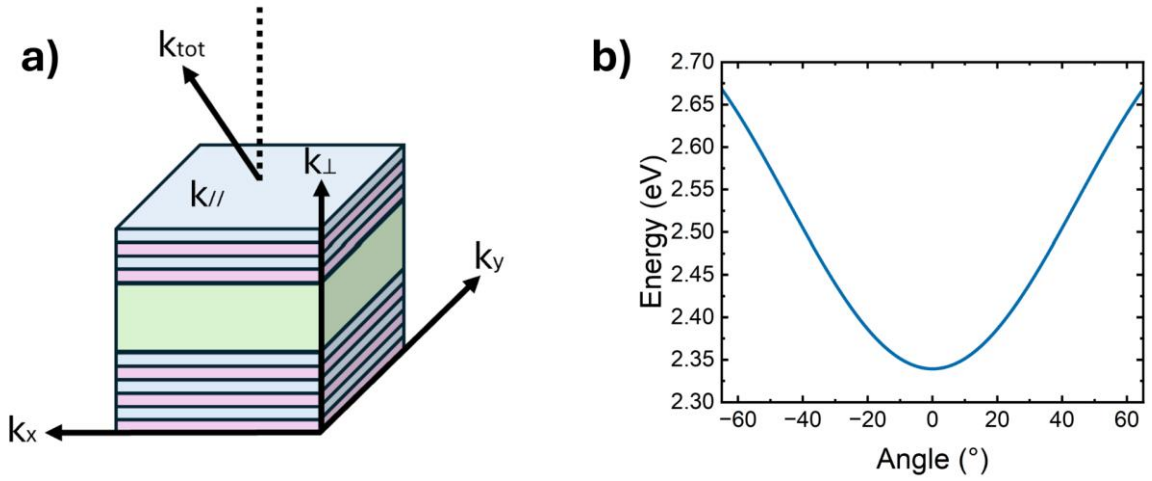

Figure 2.8 a) *Wavevector decomposition in a planar optical microcavity, total photon wavevector k_{tot} decomposed into in-plane ($k_{\parallel}$=k_x,k_y) and out-of-plane ($k_{\perp}$) components in a planar DBR microcavity* ***b)*** *Angular dispersion of the bare cavity photon mode.*

In experiments, cavity modes are typically probed via angle-resolved reflectivity or photoluminescence. The in-plane wavevector is directly related to the external emission angle θ_{ext} by

$$k_{\parallel} = \frac{\omega}{c} sin\theta_{ext} \tag{2.25}$$

here ω is the photon angular frequency. Substituting this relation into the dispersion yields the experimentally observed cavity mode energy as a function of angle (shown in **Figure 2.8b**):

$$E_c(\theta_{ext}) = E_0(1 - \frac{sin^2\theta_{ext}}{{n_c}^2})^{-\frac{1}{2}} \tag{2.26}$$

This expression shows that the cavity mode energy increases with increasing angle, giving rise to the characteristic upward-curving dispersion observed in angle-resolved measurements. Both the effective cavity length and refractive index play critical roles in shaping this dispersion.

It should be noted that cavity modes are polarization dependent. Transverse electric (TE) and transverse magnetic (TM) modes experience different phase shifts upon reflection from the DBR mirrors, leading to a small but measurable splitting at high angles. This effect becomes increasingly important in high-Q cavities and must be considered when analyzing angle-resolved dispersion[32].

2.5. Exciton-polaritons

When an optically active material is embedded inside an optical microcavity, its electronic dipole transitions can interact with the confined electromagnetic field of the cavity, provided that the excitonic transition energy is resonant (or near resonant) with the cavity photon mode. This interaction enables coherent energy exchange between light and matter, characterized by a coupling strength g, which is proportional to the transition dipole moment (oscillator strength) of the exciton and the electric field amplitude of the cavity mode. This process is schematically illustrated in **Figure 2.9**.

The nature of the light-matter interaction is determined by the relative magnitude of the coupling strength g compared to the photon decay rate of the cavity, κ ($\kappa = 1/\tau_{ph}$), and the exciton dephasing (or non-radiative decay) rate, γ. Depending on this balance, the system operates either in the weak-coupling or strong-coupling regime.

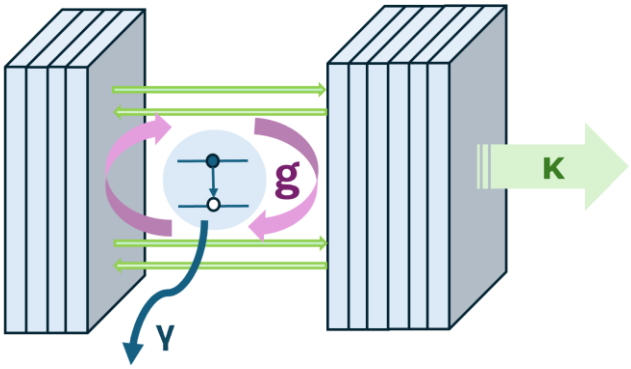

Figure 2.9 *Interaction of exciton and photon in a microcavity*

2.5.1. Weak Coupling

When the coupling strength g is smaller than the combined loss rates of the system, i.e.

$$g < \frac{\kappa+\gamma}{2} \tag{2.27}$$

The system is said to be in the weak-coupling regime. In this case, the emission of a photon is hardly absorbed by the active materials. Instead, the presence of the cavity modifies the photonic environment, altering the spontaneous emission rate of the emitter without changing its energy structure.

A hallmark of the weak-coupling regime is the Purcell effect, which describes the enhancement (or suppression) of the spontaneous emission rate of an emitter placed inside a resonant optical cavity. The enhancement factor, known as the Purcell factor F_p, is defined as[33]

$$F_p = \frac{\Gamma_c}{\Gamma_{free}} = \frac{3}{4\pi^2}\left(\frac{\lambda}{n}\right)^3 \frac{Q}{V_{eff}} \tag{2.28}$$

where Γ_c and Γ_{free} are the radiative decay rates inside and outside the cavity, respectively, λ is the emission wavelength, n is the refractive index of the cavity medium, Q is the cavity quality factor, and V_{eff} is the effective optical mode volume.

Physically, the Purcell effect arises from the modification of the local photonic density of states (LDOS) inside the cavity. According to Fermi's golden rule, the spontaneous emission rate for a transition from an initial state i to a final state f is given by

$$\Gamma_{i\to f} = \frac{2\pi}{\hbar}\left|M_{i\to f}\right|^2 \rho(\hbar\omega) \qquad (2.29)$$

where $M_{i\to f}$ is the matrix element of the interaction energy, ρ($\hbar$ω) is the photonic density of states at the transition energy. By increasing the density of optical states at resonance, the cavity enhances the probability of radiative recombination.

It should be noted that the Purcell factor represents the maximum achievable enhancement, assuming perfect spectral resonance between the emitter and cavity mode, optimal spatial overlap, alignment of the dipole moment with the cavity field, and negligible competing non-radiative processes. In practical systems, deviations from these ideal conditions often reduce the observed enhancement.

2.5.2. Strong Coupling

When the light-matter coupling strength g exceeds the photon decay rate κ and the exciton dephasing rate γ, the system enters the strong-coupling regime. In this regime, energy is coherently and reversibly exchanged between the cavity photon mode and the excitonic transition at a characteristic frequency known as the Rabi frequency, Ω.[34]

Under strong coupling, excitons and photons no longer exist as independent eigenstates. Instead, they hybridize to form new bosonic quasiparticles called exciton-polaritons. These polaritons are coherent superpositions of their light and matter components and simultaneously inherit a small effective mass from their photonic part and strong interactions from their excitonic part.

The criterion for achieving the strong-coupling regime is commonly expressed as

$$g^2 > \sqrt{\frac{\gamma^2 + \kappa^2}{2}} \tag{2.30}$$

which ensures that the coherent coupling dominates over dissipative processes. When this condition is satisfied, the eigenenergies of the system split into two distinct branches, called the upper polariton branch (UPB) and the lower polariton branch (LPB), separated by the Rabi splitting $\hbar\Omega = 2g$.[34]

The coupling strength g depends on both the oscillator strength of the excitonic transition and the electromagnetic field confinement of the cavity. It can be expressed as[35]

$$g \propto \sqrt{\frac{f}{n_c^2 L_{eff}}} \tag{2.31}$$

where nc is the refractive index in the cavity, f is exciton oscillator strength per unit area, and L_{eff} is the effective cavity length (see eq. 2.14). This scaling highlights that strong coupling is favored by a high density of absorbers and strong optical confinement. Consequently, in organic or hybrid material systems, achieving strong coupling typically requires a large molecular density or materials with intrinsically strong excitonic oscillator strengths.

As we have known $\kappa = 1/\tau_{ph}$, combining with eq. 2.18, the photon decay rate κ then can be related to the cavity quality factor Q through

$$\kappa = \frac{\omega}{Q} \tag{2.32}$$

where ω is the angular frequency of the cavity mode. A high-Q cavity therefore minimizes photon leakage and prolongs the photon lifetime, which is crucial for sustaining coherent light-matter interactions.

In contrast, evaluating the exciton dephasing rate γ is more complex, as it encompasses multiple decay and decoherence pathways. These include radiative decay into non-cavity modes, emission into off-resonant cavity modes, non-radiative recombination via defects or phonons, and pure dephasing processes.[32] All of these mechanisms contribute to broadening of the excitonic resonance and increase the effective value of γ, thereby raising the threshold for strong coupling.[36]

Alternatively, the energies and compositions of UPB and LPB states can be qualitatively obtained by diagonalizing a coupled two-level Hamiltonian describing the interaction between a cavity photon mode and an excitonic resonance.

The system can be represented by the Hamiltonian:

$$H = \begin{pmatrix} E_c(k_\parallel) & g \\ g & E_x(k_\parallel) \end{pmatrix} \tag{2.33}$$

where $E_c(k_\parallel)$ is the cavity photon dispersion as a function of the in-plane wavevector $k_\parallel$, E_x is the exciton energy (assumed to be nearly dispersionless due to the large exciton effective mass), and g is the light-matter coupling strength.

Diagonalization of this Hamiltonian yields the polariton eigenenergies:[37]

$$E_{UP/LP}(k_\parallel) = \frac{E_c(k_\parallel) + E_x}{2} \pm \frac{1}{2}\sqrt{[E_c(k_\parallel) - E_x]^2 + 4g^2} \tag{2.34}$$

Where UPB has higher energy (positive second term) and LPB has lower energy (negative second term). This expression describes the characteristic anticrossing behavior observed in angle-resolved measurements, which is a hallmark of strong coupling. At the resonance condition $E_c = E_x$, the energy splitting between the UPB and LPB is equal to the Rabi splitting $\hbar\Omega = 2g$.

Because the cavity photon energy depends on the in-plane wavevector $k_\parallel$, while the exciton energy remains nearly constant, the polariton branches inherit their dispersion primarily from the photonic component. As a result, the LPB exhibits a parabolic dispersion near $k_\parallel = 0$, with a very small effective mass. This extremely light effective mass is a key factor enabling polariton condensation at relatively low particle densities.

The composition of the polariton states can be quantified using the Hopfield coefficients, which describe the relative excitonic and photonic fractions of the polariton wavefunction. The polariton states can be written as

$$| \psi_{pol} \rangle = X(k_\parallel) | X \rangle + C(k_\parallel) | C \rangle \tag{2.35}$$

where $| X \rangle$ and $| C \rangle$ represent the bare exciton and cavity photon states, respectively, and $X(k_\parallel)$ and $C(k_\parallel)$ are the Hopfield coefficients.

The excitonic and photonic fractions are given by

$$\left|X(k_\parallel)\right|^2 = \frac{1}{2}\left(1 + \frac{E_x - E_c(k_\parallel)}{\sqrt{[E_c(k_\parallel) - E_x]^2 + 4g^2}}\right) \tag{2.36}$$

$$\left|C(k_\parallel)\right|^2 = \frac{1}{2}\left(1 - \frac{E_x - E_c(k_\parallel)}{\sqrt{[E_c(k_\parallel) - E_x]^2 + 4g^2}}\right) \tag{2.37}$$

with the normalization condition

$$|X|^2 + |C|^2 = 1 \tag{2.38}$$

The Hopfield coefficients depend strongly on the exciton-photon detuning, defined as

$$\Delta = E_c(0) - E_x \tag{2.39}$$

For negative detuning ($\Delta < 0$), the LPB is more photon-like, resulting in a lighter effective mass and faster radiative decay. Conversely, for positive detuning ($\Delta > 0$), the LPB becomes more exciton-like, leading to stronger interactions but reduced lifetime. At zero detuning, the LPB and UPB are equal superpositions of exciton and photon states. **Figure 2.10** illustrates the UPB and LPB dispersion relations and their corresponding Hopfield coefficients for three detuning conditions: negative, zero, and positive detuning. The anti-crossing behaviour at small in-plane wavevectors confirms the strong coupling regime, with a minimum energy splitting of $2g$ at zero detuning. The lower panels show the evolution of the excitonic ($|X|^2$) and photonic ($|C|^2$) fractions, revealing how the polariton composition depends on detuning: the LPB becomes increasingly photon-like for negative detuning and more exciton-like for positive detuning. This tunable light-matter character underpins the relaxation dynamics and nonlinear behaviour of exciton-polaritons in microcavities.

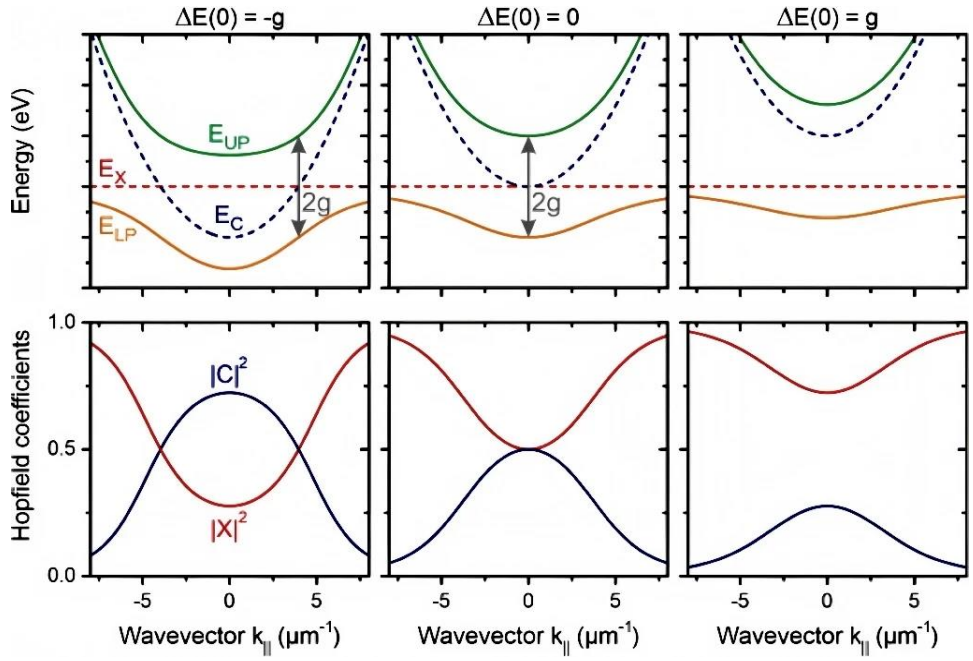

Figure 2.10 *UPB and LPB dispersions and corresponding excitonic and photonic fractions as a function of in-plane wavevector for different exciton-photon detunings.* ***a)*** *negative detuning;* ***b)*** *zero detuning;* ***c)*** *positive detuning.*[38] *Here, $|X|^2$ and $|C|^2$ are the excitonic and photonic fraction of LPB.*

2.6. Polariton Condensation

When exciton-polaritons are generated in sufficiently high densities and experience efficient relaxation toward the bottom of the LPB, they can undergo a collective phase transition known as polariton condensation or polariton lasing. This phenomenon is closely related to, but fundamentally distinct from conventional photon lasing which requires population inversion. Before we discuss how polariton lasing works, we will first introduce photon lasing.

2.6.1. Photon Lasing

Photon lasing is the conventional lasing mechanism observed in optical cavities containing a gain medium. It relies on population inversion between electronic states and stimulated emission of photons into a resonant cavity mode. In this weak-coupling regime, light-matter interaction is insufficient to form hybrid states, and excitons and photons behave as independent entities, as discussed in Section 2.5.1.

It involves three fundamental processes: absorption, spontaneous emission, and stimulated emission, as illustrated schematically in **Figure 2.11** for a transition between a ground state E_1 and an excited state E_2. Absorption and emission occur for photons with energy of $E_{ph} = E_2 - E_1$.

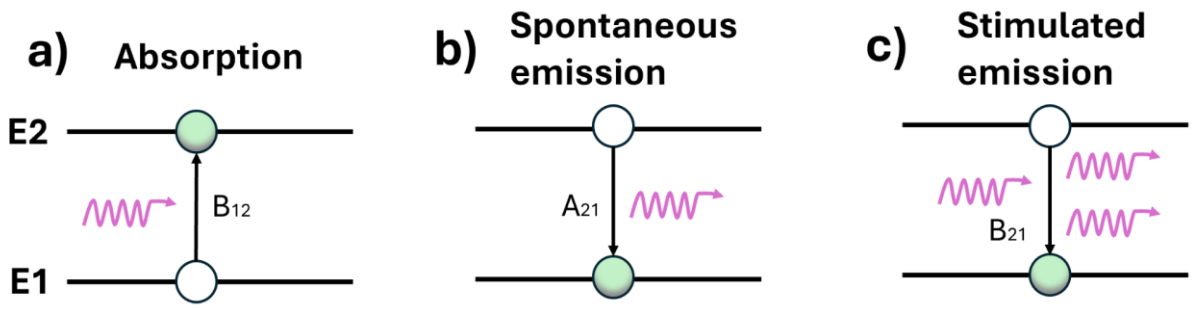

Figure 2.11 *Schematic diagram of* ***a)*** *absorption,* ***b)*** *spontaneous emission,* ***c)*** *stimulated emission in a two-level energy system. Here, E2 is the excited state and E1 is the ground state.*

The spontaneous emission rate is described by[39]

$$\frac{dN_2}{dt} = -A_{21}N_2 \qquad (2.40)$$

where N_2 is the excited-state population and A_{21} is the Einstein A-coefficient, which is related to the radiative lifetime τ by A_{21}=1/τ.

Absorption and stimulated emission processes require the presence of photon, therefore they also depend on the photon density ρ(ω) at the transition frequency ω, and are described by[39]

$$\frac{dN_1}{dt} = -B_{12}N_1\rho(\omega) \tag{2.41}$$

$$\frac{dN_2}{dt} = -B_{21}N_2\rho(\omega) \tag{2.42}$$

where B_{12} and B_{21} are the Einstein coefficients for absorption and stimulated emission, respectively. Stimulated emission generates a second photon with identical energy, phase, and direction as the incident photon, forming the basis of optical amplification, as shown in **Figure 2.11c**. By imposing thermal equilibrium conditions and using Planck's law of black-body radiation, the Einstein coefficients are related through[39]

$$g_1B_{12} = g_2B_{21} \tag{2.43}$$

$$A_{21} = \frac{\hbar\omega^3}{\pi^2c^2}B_{21} \tag{2.44}$$

where g_1 and g_2 are the degeneracies of the two states. These relations demonstrate that materials with strong optical absorption also exhibit strong spontaneous and stimulated emission.

For lasing to occur, the rate of stimulated emission must exceed that of absorption, requiring a condition

$$N_2 > \frac{g_2}{g_1}N_1 \tag{2.45}$$

known as population inversion, which cannot be achieved in thermal equilibrium and therefore necessitates external pumping.

Optical gain in the medium is described by[40]

$$I(z) = I_0 e^{Gz} \tag{2.46}$$

where G is the gain coefficient. By placing the gain medium inside a resonant cavity with mirror reflectivities R_1 and R_2, the effective interaction length is enhanced. The threshold gain for lasing is then given by[40]

$$G_{th} = \alpha - \frac{1}{2L} ln(R_1 R_2) \tag{2.47}$$

here α represents internal losses and L is the cavity length. Below threshold, emission is dominated by spontaneous processes, while above threshold, stimulated emission leads to a rapid increase in coherent, monochromatic output intensity

2.6.1.1. Amplified Spontaneous Emission vs. Photon Lasing

Amplified spontaneous emission (ASE) is the process where spontaneously emitted photons are amplified within a gain medium. Although ASE and photon lasing both result in enhanced optical emission, they arise from different physical mechanisms.

ASE occurs when spontaneous emission is amplified through stimulated emission as it propagates through a gain medium, without requiring optical feedback from a resonant cavity. In thin films or waveguides, ASE typically manifests as a sudden increase in emission intensity accompanied by linewidth narrowing above a threshold pump fluence. However, ASE lacks true mode selection, long-range coherence, and a well-defined cavity resonance.

Photon lasing, by contrast, requires optical feedback provided by a resonator, such as a DBR microcavity. The presence of a cavity enforces discrete optical modes and leads to highly directional, coherent emission. While both ASE and photon lasing involve population inversion and stimulated emission, only photon lasing exhibits strong cavity-mode dependence and true

lasing coherence. Crucially, both ASE and photon lasing occur in the weak coupling regime, where excitonic effects play a limited role and exciton-photon hybridization is absent.

2.6.2. Exciton-polariton Bose-Einstein Condensation

Bosons and fermions constitute the two fundamental classes of particles in nature, distinguished by their quantum statistical behaviour. Fermions obey the Pauli exclusion principle, which forbids two or more identical fermions from occupying the same quantum state simultaneously, as illustrated in **Figure 2.12a**. In contrast, bosons are not subject to this restriction and may occupy a single quantum state in macroscopic numbers (see **Figure 2.12b**).

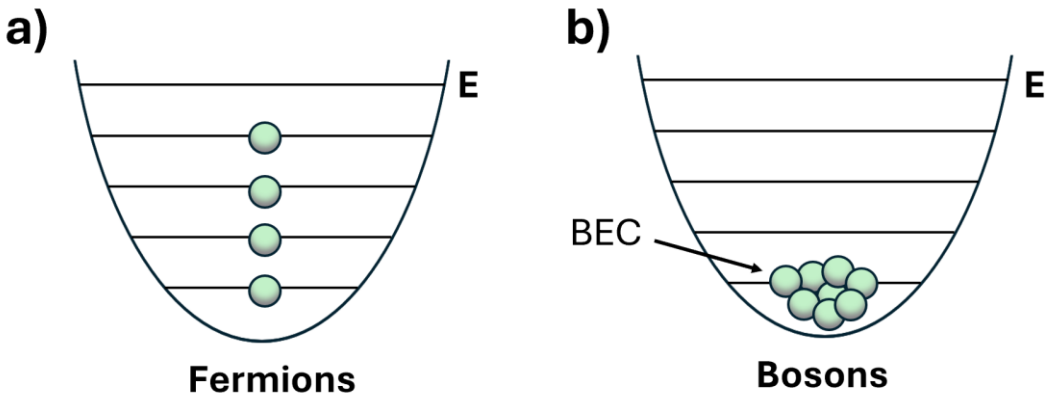

Figure 2.12 *Schematic diagrams of fermions and bosons.* ***a)*** *each fermion only occupies one quantum state,* ***b)*** *bosons can occupy the same quantum state.*

A defining property of bosons is that the probability for scattering into an already occupied quantum state is enhanced by the presence of other bosons in that state. This effect, known as bosonic final-state stimulation, leads to an avalanche-like increase in population of the same

quantum state once a critical density is reached[41,42]. Together with the absence of the Pauli exclusion principle, this behaviour forms the fundamental basis of Bose-Einstein condensation (BEC).

The concept of BEC originated from the work of Satyendra Nath Bose, who in 1924 derived Planck's law for black-body radiation by treating photons as a gas of indistinguishable, non-interacting bosons[43]. Building on this idea, Albert Einstein predicted that a conserved gas of massive bosons would undergo a phase transition below a critical temperature, at which a macroscopic fraction of particles condenses into the lowest quantum state. In this regime, the particles become indistinguishable and are described by a single macroscopic wavefunction, which is a defining feature of BEC. For BEC to occur, the wavefunctions of individual bosons must overlap significantly. This condition is reached when the thermal de Broglie wavelength, λ_{dB}, becomes comparable to the average interparticle spacing.

For a particle of momentum p, the de Broglie wavelength is defined as

$$\lambda_{dB} = \frac{h}{p} = \frac{2\pi\hbar}{p} \tag{2.48}$$

In a thermal gas, the characteristic momentum is determined by the thermal energy. For particles obeying Maxwell-Boltzmann statistics, the average kinetic energy is

$$\frac{p^2}{2m} = \frac{3}{2}k_B T \tag{2.49}$$

leading to a thermally averaged de Broglie wavelength

$$\lambda_{dB} = \sqrt{\frac{2\pi\hbar^2}{mk_B T}} \tag{2.50}$$

This expression shows that the λ_{dB} increases as the temperature decreases or as the particle mass becomes smaller. When λ_{dB} becomes comparable to the mean interparticle spacing, the individual particle wavefunctions begin to overlap, signalling a macroscopic fraction of bosons occupying the lowest quantum state, forming a BEC. The critical temperature T_c for condensation in an ideal three-dimensional Bose gas is given by

$$T_c = \frac{2\pi\hbar^2}{mk_BT}\left(\frac{n}{\varsigma(3/2)}\right)^{\frac{2}{3}} \tag{2.51}$$

where n is the particle density and ζ(3/2) ≈ 2.612 is the Riemann zeta function.

As hybrid light-matter states, polaritons inherit the exceptionally small effective mass of photons and the strong nonlinear interactions of excitons[44], making them ideal bosonic quasiparticles for realizing BEC at higher temperature than atomic gas. Under sufficient pumping, polaritons relax toward the bottom of the LPB and may macroscopically occupy the ground state. In this condensed phase, polaritons share a common energy, momentum, and phase, and photons escaping the cavity inherit these properties, resulting in coherent emission that closely resembles laser light.

The first experimental demonstration of polariton BEC was reported by Kasprzak et al. in a CdTe microcavity at cryogenic temperatures in 2006[45]. Since then, polariton condensation has been realized in a variety of material systems, including inorganic and organic semiconductors, and metal-halide perovskites, extending up to and beyond room temperature[46–48]. One practical advantage of polariton systems is that high particle densities can be readily achieved through either optical pumping or electrical injection.

For optical excitation, which is the most common approach in polariton experiments, two pumping schemes are typically used: i) resonant excitation, where polaritons are directly injected into the LPB at finite in-plane momentum using excitation near the exciton energy and at a large incident

angle; and ii) non-resonant excitation, where carriers are generated at higher energies, typically at the reflectivity minimum of the DBR stopband near $k_{\parallel} = 0$, from which they relax into the exciton reservoir[49]. These two excitation schemes are illustrated by the green and purple arrows in **Figure 2.13a**.

In both cases, excitation creates a high-energy exciton reservoir, from which polaritons are formed and populate a broad range of states along the LPB. Subsequent relaxation toward lower energies happens primarily through scattering with the crystal lattice and energy dissipation via phonon emission. However, as LPs relax toward smaller in-plane wavevectors, they become increasingly photon-like. This reduces their scattering efficiency while simultaneously shortening their lifetime due to enhanced photon leakage from the cavity. As a result, polaritons are often unable to reach the $k_{\parallel} = 0$ ground state before decaying, leading to the formation of a polariton relaxation bottleneck[50]. In this regime, polaritons accumulate at finite momentum rather than condensing at the bottom of the LPB, thereby hindering the onset of polariton condensation.

At sufficiently high polariton densities, polariton-polariton scattering (also known as stimulated scattering) becomes the dominant relaxation pathway. Owing to their excitonic component, polaritons inherit strong Coulomb-mediated interactions, giving rise to strong polariton-polariton repulsive interaction. These interactions significantly enhance thermalization toward the LPB minimum, enabling rapid population of the ground state and facilitating polariton condensation. The combined phonon-assisted and interaction-driven relaxation pathways are schematically illustrated in **Figure 2.13a**.

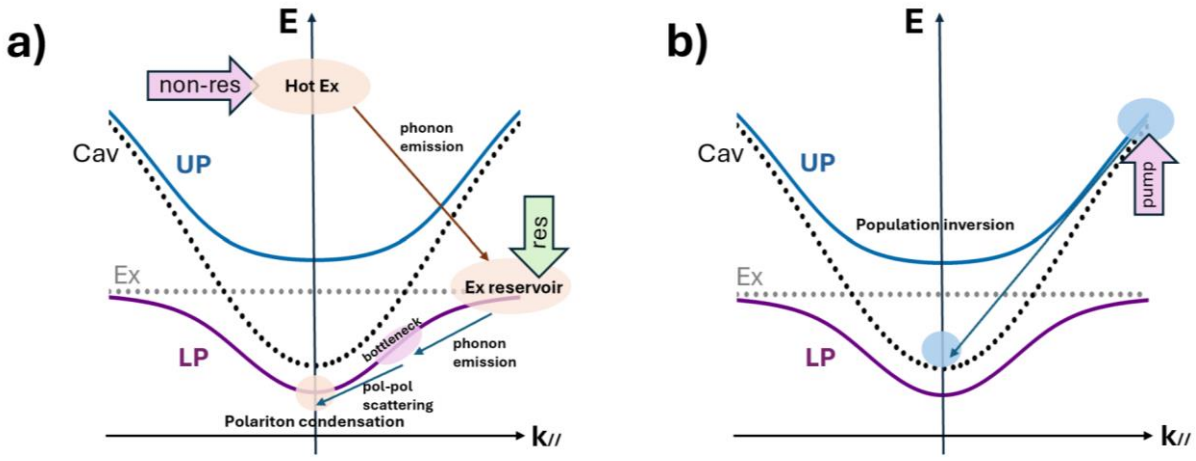

Figure 2.13 *Schematic process for* ***a)*** *polariton lasing and* ***b)*** *photonic lasing*

Bosonic final-state stimulation in polariton systems leads directly to nonlinear emission, while the macroscopic occupation of a single quantum state results in pronounced spatial and temporal coherence. Consequently, emission from a polariton condensate exhibits laser-like characteristics[51]. In contrast, photon lasing, illustrated in **Figure 2.13b**, is achieved through population inversion and stimulated emission of photons into the ground state of the cavity photon mode. This process occurs in the weak-coupling regime and requires significantly higher excitation densities. Polariton lasing, by comparison, occurs without population inversion, resulting in threshold powers that can be orders of magnitude lower than those required for conventional photon lasing[52]. In many microcavity systems, two distinct nonlinear thresholds are therefore observed: a lower threshold corresponding to polariton condensation, and a higher threshold marking the transition to photon lasing once strong coupling is lost.

2.7. A Historical View: Exciton-polaritons in 2D Layered Perovskites

Over the past decade, MHPs have emerged as a highly promising class of semiconductors for investigating light-matter interactions, not only from their outstanding optical properties as we discussed previously, but also from their remarkable versatility in fabrication and structural design. Perovskites can be synthesized using low-cost solution-based techniques and exhibit a high degree of tunability in composition, crystal structure, and dimensionality, spanning 3D bulk materials, 2D layered systems, 1D microwires, and 0D nanocrystals. This structural flexibility enables bandgap engineering across a broad spectral range from the ultraviolet to the near-infrared[53]. Among these systems, 2D Ruddlesden-Popper perovskites are particularly attractive for strong light-matter coupling studies. Their natural quantum-well architecture, combined with pronounced dielectric confinement results in large exciton binding energies and enhanced oscillator strengths.

The first experimental demonstration of strong coupling in a perovskite system employed spin-coated thin films of the 2D perovskite $(PEA)_2PbI_4$ integrated into a distributed feedback (DFB) cavity[54]. Subsequent studies in 2D perovskites between 2008 and 2012 explored a variety of Fabry-Pérot-type microcavity architectures, including all-dielectric, all-metal, and hybrid dielectric-metal mirrors[55–57]. These investigations collectively aimed to optimize cavity designs to enhance exciton-photon interaction strength.

Despite these early successes, the fabricated structures typically exhibited relatively low Q factors, primarily limited by film roughness, inhomogeneity, and scattering losses associated with solution-processed layers. The resulting short polariton lifetimes hindered the accumulation and thermalization of polaritons, preventing the realization of polariton condensation.[58]

Significant progress was achieved in 2018 through the use of mechanically exfoliated single-crystal flakes of $(PEA)_2PbI_4$ and $(PEA)_2PbBr_4$ embedded within double-DBR planar microcavities.

These systems demonstrated clear strong coupling with Rabi splittings as large as 242 meV and substantially improved cavity Q-factors exceeding 2000.[59] Building on this advancement, polariton condensation was reported in 2020 using high-quality exfoliated PEAI perovskite flakes placed within an Ag-DBR microcavity at cryogenic temperatures (4 K).[60] To date, this remains the only confirmed observation of polariton condensation in a 2D perovskite system.

More recently, perovskite-based polaritonic platforms have been extended toward room-temperature quantum simulation. In 2022, a polaritonic XY spin Hamiltonian was realized in halide perovskites confined within nanostructured microcavities.[61] This work employed a solution-based nanoconfinement growth strategy, in which two DBR mirrors were thermally pressed together using patterned gold pillars as spacers. The resulting nanocavity simultaneously functioned as an optical resonator and a confined growth environment, enabling the formation of smooth, large-area single-crystalline perovskite layers.

In summary, 2D halide perovskites have proven to be promising platforms for studying exciton-polaritons, nevertheless, several challenges remain. Material instability, particularly under ambient conditions, continues to limit device reproducibility and lifetime. Film uniformity and thickness control must be further improved to minimize inhomogeneous broadening of excitonic resonances.[62] Additionally, achieving higher cavity Q-factors, which is crucial for extending polariton lifetimes and enabling condensation, remains difficult due to scattering and interface losses. Finally, a comprehensive understanding of relaxation dynamics, reservoir interactions, and loss mechanisms in 2D perovskite polariton systems is still lacking. Given that polariton condensation has only been observed under highly controlled cryogenic conditions, systematic studies are required to clarify the factors that govern condensation thresholds and stability.

References

1 T. Niu, J. Lu, R. Munir, J. Li, D. Barrit, X. Zhang, H. Hu, Z. Yang, A. Amassian, K. Zhao, and S. (Frank) Liu, "Stable High-Performance Perovskite Solar Cells via Grain Boundary Passivation," Advanced Materials 30(16), 1706576 (2018).

2 S.D. Stranks, G.E. Eperon, G. Grancini, C. Menelaou, M.J.P. Alcocer, T. Leijtens, L.M. Herz, A. Petrozza, and H.J. Snaith, "Electron-hole diffusion lengths exceeding 1 micrometer in an organometal trihalide perovskite absorber," Science 342(6156), 341–344 (2013).

3 N. Arora, M.I. Dar, A. Hinderhofer, N. Pellet, F. Schreiber, S.M. Zakeeruddin, and M. Grätzel, "Perovskite solar cells with CuSCN hole extraction layers yield stabilized efficiencies greater than 20," Science 358(6364), 768–771 (2017).

4 W.S. Yang, B.-W. Park, E.H. Jung, N.J. Jeon, Y.C. Kim, D.U. Lee, S.S. Shin, J. Seo, E.K. Kim, J.H. Noh, and S.I. Seok, "Iodide management in formamidinium-lead-halide-based perovskite layers for efficient solar cells," Science 356(6345), 1376–1379 (2017).

5 Y. Cao, N. Wang, H. Tian, J. Guo, Y. Wei, H. Chen, Y. Miao, W. Zou, K. Pan, Y. He, H. Cao, Y. Ke, M. Xu, Y. Wang, M. Yang, K. Du, Z. Fu, D. Kong, D. Dai, Y. Jin, G. Li, H. Li, Q. Peng, J. Wang, and W. Huang, "Perovskite light-emitting diodes based on spontaneously formed submicrometre-scale structures," Nature 562(7726), 249–253 (2018).

6 K. Lin, J. Xing, L.N. Quan, F.P.G. de Arquer, X. Gong, J. Lu, L. Xie, W. Zhao, D. Zhang, C. Yan, W. Li, X. Liu, Y. Lu, J. Kirman, E.H. Sargent, Q. Xiong, and Z. Wei, "Perovskite light-emitting diodes with external quantum efficiency exceeding 20 per cent," Nature 562(7726), 245–248 (2018).

7 Y. He, L. Matei, H.J. Jung, K.M. McCall, M. Chen, C.C. Stoumpos, Z. Liu, J.A. Peters, D.Y. Chung, B.W. Wessels, M.R. Wasielewski, V.P. Dravid, A. Burger, and M.G. Kanatzidis, "High spectral resolution of gamma-rays at room temperature by perovskite CsPbBr3 single crystals," Nat Commun 9(1), 1609 (2018).

8 H. Wei, Y. Fang, P. Mulligan, W. Chuirazzi, H.-H. Fang, C. Wang, B.R. Ecker, Y. Gao, M.A. Loi, L. Cao, and J. Huang, "Sensitive X-ray detectors made of methylammonium lead tribromide perovskite single crystals," Nature Photonics 10, 333–339 (2016).

9 S.W. Eaton, M. Lai, N.A. Gibson, A.B. Wong, L. Dou, J. Ma, L.-W. Wang, S.R. Leone, and P. Yang, "Lasing in robust cesium lead halide perovskite nanowires," Proc Natl Acad Sci U S A 113(8), 1993–1998 (2016).

10 H. Zhu, Y. Fu, F. Meng, X. Wu, Z. Gong, Q. Ding, M.V. Gustafsson, M.T. Trinh, S. Jin, and X.-Y. Zhu, "Lead halide perovskite nanowire lasers with low lasing thresholds and high quality factors," Nat Mater 14(6), 636–642 (2015).

11 H. Tsai, W. Nie, J.-C. Blancon, C.C. Stoumpos, R. Asadpour, B. Harutyunyan, A.J. Neukirch, R. Verduzco, J.J. Crochet, S. Tretiak, L. Pedesseau, J. Even, M.A. Alam, G. Gupta, J. Lou, P.M. Ajayan, M.J. Bedzyk, and M.G. Kanatzidis, "High-efficiency two-dimensional Ruddlesden-Popper perovskite solar cells," Nature 536(7616), 312–316 (2016).

12 L. Mao, C.C. Stoumpos, and M.G. Kanatzidis, "Two-Dimensional Hybrid Halide Perovskites: Principles and Promises," J Am Chem Soc 141(3), 1171–1190 (2019).

13 B. Saparov, and D.B. Mitzi, "Organic-Inorganic Perovskites: Structural Versatility for Functional Materials Design," Chem Rev 116(7), 4558–4596 (2016).

14 Y. Fu, H. Zhu, J. Chen, M.P. Hautzinger, X.-Y. Zhu, and S. Jin, “Metal halide perovskite nanostructures for optoelectronic applications and the study of physical properties,” Nat Rev Mater 4(3), 169–188 (2019).

15 E. Kirstein, D.R. Yakovlev, M.M. Glazov, E.A. Zhukov, D. Kudlacik, I.V. Kalitukha, V.F. Sapega, G.S. Dimitriev, M.A. Semina, M.O. Nestoklon, E.L. Ivchenko, N.E. Kopteva, D.N. Dirin, O. Nazarenko, M.V. Kovalenko, A. Baumann, J. Höcker, V. Dyakonov, and M. Bayer, “The Landé factors of electrons and holes in lead halide perovskites: universal dependence on the band gap,” Nat Commun 13(1), 3062 (2022).

16 A. Walsh, “Principles of Chemical Bonding and Band Gap Engineering in Hybrid Organic-Inorganic Halide Perovskites,” J Phys Chem C Nanomater Interfaces 119(11), 5755–5760 (2015).

17 K.X. Steirer, P. Schulz, G. Teeter, V. Stevanovic, M. Yang, K. Zhu, and J.J. Berry, “Defect Tolerance in Methylammonium Lead Triiodide Perovskite,” ACS Energy Lett. 1(2), 360–366 (2016).

18 M.U. Rothmann, J.S. Kim, J. Borchert, K.B. Lohmann, C.M. O’Leary, A.A. Sheader, L. Clark, H.J. Snaith, M.B. Johnston, P.D. Nellist, and L.M. Herz, “Atomic-scale microstructure of metal halide perovskite,” Science 370(6516), eabb5940 (2020).

19 R.E. Brandt, V. Stevanović, D.S. Ginley, and T. Buonassisi, “Identifying defect-tolerant semiconductors with high minority-carrier lifetimes: beyond hybrid lead halide perovskites,” MRS Communications 5(2), 265–275 (2015).

20 X. Wu, M.T. Trinh, and X.-Y. Zhu, “Excitonic Many-Body Interactions in Two-Dimensional Lead Iodide Perovskite Quantum Wells,” J. Phys. Chem. C 119(26), 14714–14721 (2015).

21 J.-C. Blancon, A.V. Stier, H. Tsai, W. Nie, C.C. Stoumpos, B. Traoré, L. Pedesseau, M. Kepenekian, F. Katsutani, G.T. Noe, J. Kono, S. Tretiak, S.A. Crooker, C. Katan, M.G. Kanatzidis, J.J. Crochet, J. Even, and A.D. Mohite, "Scaling law for excitons in 2D perovskite quantum wells," Nat Commun 9(1), 2254 (2018).

22 L. Pedesseau, J.-M. Jancu, A. Rolland, E. Deleporte, C. Katan, and J. Even, "Electronic properties of 2D and 3D hybrid organic/inorganic perovskites for optoelectronic and photovoltaic applications," Optical and Quantum Electronics 46, 1225–1232 (2014).

23 M. Kepenekian, R. Robles, C. Katan, D. Sapori, L. Pedesseau, and J. Even, "Rashba and Dresselhaus Effects in Hybrid Organic-Inorganic Perovskites: From Basics to Devices," ACS Nano 9(12), 11557–11567 (2015).

24 J. Even, L. Pedesseau, C. Katan, M. Kepenekian, J.-S. Lauret, D. Sapori, and E. Deleporte, "Solid-State Physics Perspective on Hybrid Perovskite Semiconductors," J. Phys. Chem. C 119(19), 10161–10177 (2015).

25 D.G. Billing, and A. Lemmerer, "Synthesis, characterization and phase transitions of the inorganic–organic layered perovskite-type hybrids [(CnH2n+1NH3)2PbI4] (n = 12, 14, 16 and 18)," New J. Chem. 32(10), 1736–1746 (2008).

26 M.D. Smith, L. Pedesseau, M. Kepenekian, I.C. Smith, C. Katan, J. Even, and H.I. Karunadasa, "Decreasing the electronic confinement in layered perovskites through intercalation," Chem. Sci. 8(3), 1960–1968 (2017).

27 Y. Li, I. Allegro, M. Kaiser, A.J. Malla, B.S. Richards, U. Lemmer, U.W. Paetzold, and I.A. Howard, "Exciton versus free carrier emission: Implications for photoluminescence efficiency and amplified spontaneous emission thresholds in quasi-2D and 3D perovskites," Materials Today 49, 35–47 (2021).

28 Q. Jiang, Y. Zhao, X. Zhang, X. Yang, Y. Chen, Z. Chu, Q. Ye, X. Li, Z. Yin, and J. You, "Surface passivation of perovskite film for efficient solar cells," Nature Photonics 13, 460–466 (2019).

29"Improvement Performance of Planar Perovskite Solar Cells by Bulk and Surface Defect Passivation," ACS Sustainable Chemistry & Engineering, (2021).

30 V. Savona, L.C. Andreani, P. Schwendimann, and A. Quattropani, "Quantum well excitons in semiconductor microcavities: Unified treatment of weak and strong coupling regimes," Solid State Communications 93(9), 733–739 (1995).

31"Born, M. and Wolf, E. (2013) Principles of Optics Electromagnetic Theory of Propagation, Interference and Diffraction of Light. Elsevier. - References - Scientific Research Publishing," (n.d.).

32 G. Panzarini, L.C. Andreani, A. Armitage, D. Baxter, M.S. Skolnick, V.N. Astratov, J.S. Roberts, A.V. Kavokin, M.R. Vladimirova, and M.A. Kaliteevski, "Cavity-polariton dispersion and polarization splitting in single and coupled semiconductor microcavities," Phys. Solid State 41(8), 1223–1238 (1999).

33 D. Kang, C. Onwukaeme, K. Park, K. Jeon, H.-Y. Ryu, and S. Yoo, "Nanophotonic route to control electron behaviors in 2D materials," Nanophotonics 13(16), 2865–2878 (n.d.).

34 V. Savona, L.C. Andreani, P. Schwendimann, and A. Quattropani, "Quantum well excitons in semiconductor microcavities: Unified treatment of weak and strong coupling regimes," Solid State Communications 93(9), 733–739 (1995).

35 D.G. Lidzey, D.D.C. Bradley, M.S. Skolnick, T. Virgili, S. Walker, and D.M. Whittaker, “Strong exciton–photon coupling in an organic semiconductor microcavity,” Nature 395(6697), 53–55 (1998).

36 V. Savona, C. Piermarocchi, A. Quattropani, P. Schwendimann, and F. Tassone, “Optical properties of microcavity polaritons,” Phase Transitions 68(1), 169–279 (1999).

37 H. Deng, H. Haug, and Y. Yamamoto, “Exciton-polariton Bose-Einstein condensation,” Rev. Mod. Phys. 82(2), 1489–1537 (2010).

38 S. Klembt, S. Betzold, and S. Höfling, “4 - Cavity quantum electrodynamics and polaritons: The physics of exciton-polaritons,” in Quantum Photonics, (Elsevier, 2024), pp. 145–187.

39 M. Fox, and M. Fox, Optical Properties of Solids, Second Edition, Second Edition (Oxford University Press, Oxford, New York, 2010).

40 A.E. Siegman, Lasers (University Science Books, 1986).

41 H. Miesner, D.M. Stamper-Kurn, M.R. Andrews, D.S. Durfee, S. Inouye, and W. Ketterle, “Bosonic stimulation in the formation of a bose-einstein condensate,” Science 279(5353), 1005–1007 (1998).

42 A. Imamog¯lu, R.J. Ram, S. Pau, and Y. Yamamoto, “Nonequilibrium condensates and lasers without inversion: Exciton-polariton lasers,” Phys. Rev. A 53(6), 4250–4253 (1996).

43 Bose, “Plancks Gesetz und Lichtquantenhypothese,” Zeitschrift Fur Physik 26, 178–181 (1924).

44 T. Byrnes, N.Y. Kim, and Y. Yamamoto, “Exciton–polariton condensates,” Nature Phys 10(11), 803–813 (2014).

45 J. Kasprzak, M. Richard, S. Kundermann, A. Baas, P. Jeambrun, J.M.J. Keeling, F.M. Marchetti, M.H. Szymańska, R. André, J.L. Staehli, V. Savona, P.B. Littlewood, B. Deveaud, and L.S. Dang, "Bose–Einstein condensation of exciton polaritons," Nature 443(7110), 409–414 (2006).

46 A. Das, J. Heo, M. Jankowski, W. Guo, L. Zhang, H. Deng, and P. Bhattacharya, "Room temperature ultralow threshold GaN nanowire polariton laser," Phys Rev Lett 107(6), 066405 (2011).

47 R. Su, C. Diederichs, J. Wang, T.C.H. Liew, J. Zhao, S. Liu, W. Xu, Z. Chen, and Q. Xiong, "Room-Temperature Polariton Lasing in All-Inorganic Perovskite Nanoplatelets," Nano Lett 17(6), 3982–3988 (2017).

48 R. Balili, V. Hartwell, D. Snoke, L. Pfeiffer, and K. West, "Bose-Einstein condensation of microcavity polaritons in a trap," Science 316(5827), 1007–1010 (2007).

49 E. del Valle, D. Sanvitto, A. Amo, F.P. Laussy, R. André, C. Tejedor, and L. Viña, "Dynamics of the formation and decay of coherence in a polariton condensate," Phys Rev Lett 103(9), 096404 (2009).

50 F. Tassone, C. Piermarocchi, V. Savona, A. Quattropani, and P. Schwendimann, "Bottleneck effects in the relaxation and photoluminescence of microcavity polaritons," Phys. Rev. B 56(12), 7554–7563 (1997).

51 A. Imamog¯lu, R.J. Ram, S. Pau, and Y. Yamamoto, "Nonequilibrium condensates and lasers without inversion: Exciton-polariton lasers," Phys. Rev. A 53(6), 4250–4253 (1996).

52 H. Deng, G. Weihs, D. Snoke, J. Bloch, and Y. Yamamoto, "Polariton lasing vs. photon lasing in a semiconductor microcavity," Proc Natl Acad Sci U S A 100(26), 15318–15323 (2003).

53 Q. Zhang, R. Su, X. Liu, J. Xing, T.C. Sum, and Q. Xiong, “High-Quality Whispering-Gallery-Mode Lasing from Cesium Lead Halide Perovskite Nanoplatelets,” (2016).

54 T. Fujita, Y. Sato, T. Kuitani, and T. Ishihara, “Tunable polariton absorption of distributed feedback microcavities at room temperature,” Phys. Rev. B 57(19), 12428–12434 (1998).

55 G. Lanty, S. Zhang, J.S. Lauret, E. Deleporte, P. Audebert, S. Bouchoule, X. Lafosse, J. Zuñiga-Pérez, F. Semond, D. Lagarde, F. Médard, and J. Leymarie, “Hybrid cavity polaritons in a ZnO-perovskite microcavity,” Phys. Rev. B 84(19), 195449 (2011).

56 Y. Wei, J.S. Lauret, L. Galmiche, P. Audebert, and E. Deleporte, “Strong exciton-photon coupling in microcavities containing new fluorophenethylamine based perovskite compounds,” Opt. Express, OE 20(9), 10399–10405 (2012).

57 Y. Wei, J.S. Lauret, L. Galmiche, P. Audebert, and E. Deleporte, “Strong exciton-photon coupling in microcavities containing new fluorophenethylamine based perovskite compounds,” Opt. Express, OE 20(9), 10399–10405 (2012).

58 R. Su, A. Fieramosca, Q. Zhang, H.S. Nguyen, E. Deleporte, Z. Chen, D. Sanvitto, T.C.H. Liew, and Q. Xiong, “Perovskite semiconductors for room-temperature exciton-polaritonics,” Nat. Mater. 20(10), 1315–1324 (2021).

59 J. Wang, R. Su, J. Xing, D. Bao, C. Diederichs, S. Liu, T.C.H. Liew, Z. Chen, and Q. Xiong, “Room Temperature Coherently Coupled Exciton-Polaritons in Two-Dimensional Organic-Inorganic Perovskite,” ACS Nano 12(8), 8382–8389 (2018).

60 L. Polimeno, A. Fieramosca, G. Lerario, M. Cinquino, M. De Giorgi, D. Ballarini, F. Todisco, L. Dominici, V. Ardizzone, M. Pugliese, C.T. Prontera, V. Maiorano, G. Gigli, L. De Marco, and

D. Sanvitto, “Observation of Two Thresholds Leading to Polariton Condensation in 2D Hybrid Perovskites,” Advanced Optical Materials 8(16), 2000176 (2020).

61 R. Tao, K. Peng, L. Haeberlé, Q. Li, D. Jin, G.R. Fleming, S. Kéna-Cohen, X. Zhang, and W. Bao, “Halide perovskites enable polaritonic XY spin Hamiltonian at room temperature,” Nat Mater 21(7), 761–766 (2022).

62 G.E. Eperon, V.M. Burlakov, P. Docampo, A. Goriely, and H.J. Snaith, “Morphological Control for High Performance, Solution-Processed Planar Heterojunction Perovskite Solar Cells,” Advanced Functional Materials 24(1), 151–157 (2014).

Chapter 3

Experimental Methods

This chapter outlines the experimental techniques employed throughout the subsequent three chapters of this thesis, including the fabrication, optical, and morphological characterization methods used to prepare and investigate the perovskite thin films and microcavity structures.

3.1. Fabrication Techniques

3.1.1. Thin Film Fabrication

Solution-processed techniques are widely employed in materials science because they are cost-effective, scalable, and relatively simple compared to vacuum-based deposition methods. Among these, spin coating is one of the most common approaches for preparing thin films, especially for optoelectronic applications. In this method, a liquid precursor solution is dispensed onto a substrate, which is then rapidly rotated to spread the solution evenly by centrifugal force. The thickness and uniformity of the resulting film are controlled by several factors, including solution concentration, viscosity, spin speed, spin time, and ambient conditions (e.g., temperature, humidity).

In this thesis, spin coating was primarily used to fabricate two-dimensional (2D) perovskite films (e.g., BA_2PbI_4) as well as organic polymer films (e.g., PMMA). The schematic process of spin-coating is shown in **Figure 3.1**. The same procedure throughout this thesis is as follows:

1. Substrate preparation: Quartz-coated glass substrates sourced from Ossila were cleaned by sequential ultrasonication in deionized water with and without Hallmenax, as well as isopropanol for 15 mins, respectively, followed by nitrogen drying. After this, substrates were treated with UV-ozone to improve surface wettability.

2. Solution preparation: The precursor solutions were prepared at controlled concentrations to define the final film thickness. For BA_2PbI_4, the perovskite precursors (butylammonium iodide (BAI) and lead iodide (PbI_2) with a ratio of 2 :1) were dissolved in different solvents of dimethyl sulfoxide (DMSO), dimethylformamide (DMF) without or with 18-crown-6 (a crown ether additive). For polymer films, poly(methyl methacrylate) (PMMA) was dissolved in chlorobenzene at a concentration of 50 mg/mL.

3. Spin-coating process: For 2D perovskite films, a 2 steps spin-coating was applied. The substrate was accelerated to a lower rotation speed eg.1000 rpm for 10s and then a higher speed e.g. 4000 revolutions per minute (rpm) for 40–60 s, allowing the solution to spread uniformly and excess solvent to be ejected. Here, we spin coat dynamically i.e. A 100 μL volume of solution was pipetted onto the substrate surface after the first 5s. While for organic films, a single step spin-coating was used. The final film thickness depends on both the spin speed (higher speed → thinner film) and the solution concentration (higher concentration → thicker film).

4. Post-deposition treatment: For perovskite films, thermal annealing was performed (100 °C for 15 min) in a N_2 filled glovebox to promote crystallization and solvent removal. For polymer layers, films were annealed at 70 °C for 1 min to remove residual solvent.

5. Thickness measurement: The resulting film thickness was measured using a Bruker DektakXT stylus profilometer. Thickness control was essential for cavity fabrication, where the optical

resonance conditions depend sensitively on the thickness of both the perovskite layer and the polymer spacer.

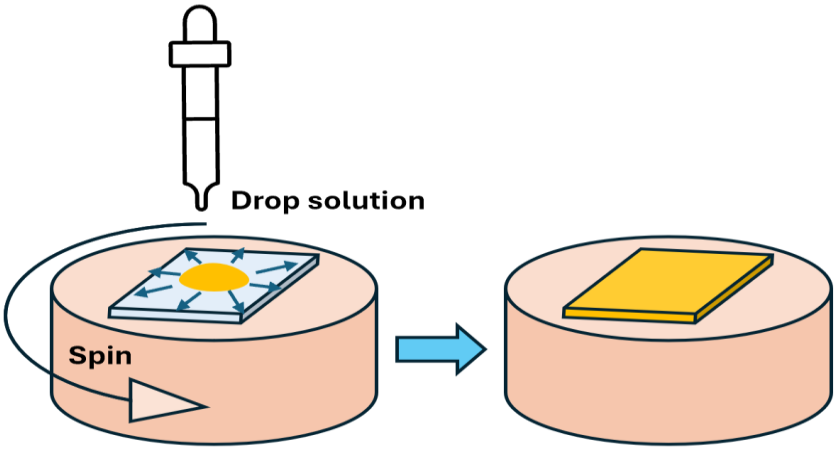

Figure 3.1 *schematic process of spin coating for thin films*

Spin coating offers several advantages for thin film fabrication: it is rapid, reproducible, and compatible with a wide range of materials. However, it also has limitations, including waste of precursor solution and difficulties in scaling to large-area uniform films. Despite these, it remains a highly versatile method and was therefore chosen for the fabrication of all thin films in this work.

3.1.2. Microcavity Design and Fabrication

The fabrication of microcavities in this work followed a design-simulation-fabrication workflow to ensure that the resulting structures exhibited the desired resonance conditions and detuning.

The process began with the preparation of a thin film of the active material (e.g., BA_2PbI_4) by spin coating at a selected precursor concentration. The film thickness was measured using a Bruker

DektakXT profilometer, and its optical absorption spectrum was recorded by a Horiba Fluoromax 4 Fluorometer with a Xe lamp. From the absorption data, the wavelength-dependent extinction coefficient of the film was calculated. To parameterize the excitonic contribution, the extinction coefficient was fitted using either a single or multiple Lorentzian peaks (depending on the number of excitonic transitions present). The fitting provided the exciton peak energy, linewidth, and oscillator strength (amplitude), which were used as inputs for the optical modelling.

3.1.2.1. Transfer Matrix Reflectivity (TMR) Model

A transfer matrix reflectivity (TMR) model was then constructed to simulate the multilayer optical response of the microcavity. In this model, the active layer film was combined with distributed Bragg reflector (DBR) mirrors, whose optical properties were defined by the number of layer pairs, thickness of each SiO_2/TiO_2 layer, and refractive index values obtained from ellipsometry, as indicated in **Figure 3.2a** and **b**, respectively.

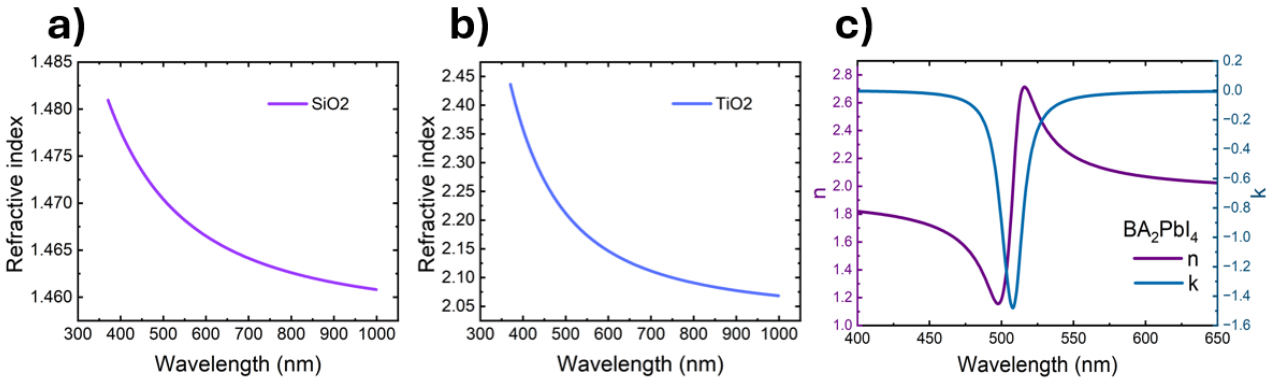

Figure 3.2 *Refractive index of* ***a)*** *SiO_2* ***b)*** *TiO_2 as a function of wavelength measured by ellipsometry, and* ***c)*** *the simulated n and k value of BA_2PbI_4 as a function of wavelength.*

To accurately incorporate the excitonic response of the BA_2PbI_4 active layer, absorption spectra were first measured from standalone films with known thickness, as determined using a Dektak profilometer. From the measured absorbance, the absorption coefficient $\alpha(E)$ was extracted and converted into the extinction coefficient $k(E)$ using[1]

$$\alpha(E) = \frac{4\pi k(E)}{\lambda} \tag{3.1}$$

The excitonic absorption feature in the extinction spectrum was then fitted using a Lorentz oscillator model to obtain the exciton resonance energy, linewidth, and oscillator strength. The dielectric response of the active layer was expressed as[2]

$$\varepsilon(E) = \varepsilon_{bg} + \sum_j \frac{f_j}{E_j^2 - E^2 - i\gamma_j E} \tag{3.2}$$

where $\varepsilon_{\mathrm{bg}}$ is the background dielectric constant, E_j is the exciton resonance energy, γ_j is the exciton linewidth, and f_j is the oscillator strength of the optical transition. The background dielectric constant is related to the background refractive index through

$$\varepsilon_{bg} = {n_{bg}}^2 \tag{3.3}$$

In the present model, a constant background refractive index of $n_{\mathrm{bg}} = 1.9$ was used for the BA_2PbI_4 active layer. This value was taken from previously reported experimental $n(\lambda)$ and $k(\lambda)$ spectra of BA_2PbI_4 and corresponds to the measured refractive index near the exciton resonance wavelength of approximately 510 nm.[3] The Lorentz oscillator term was then used to introduce the resonant excitonic contribution to the dielectric function, thereby reproducing both the dispersive and absorptive components of the excitonic response self-consistently within the TMR simulations.

The complex refractive index used in the simulations was obtained through[1]

$$\tilde{n}(E) = n(E) + ik(E) = \sqrt{\varepsilon(E)} \tag{3.4}$$

allowing both the real and imaginary parts of the refractive index (see **Figure 3.2c**) to evolve naturally from the excitonic dielectric response. The extracted excitonic parameters were incorporated directly into the multilayer cavity model, enabling the experimentally measured absorbance spectrum of the bare BA_2PbI_4 film to be reproduced accurately. After validation of the active-layer dielectric function, the full cavity structure, including the distributed Bragg reflectors (DBRs), was simulated to calculate the angle-dependent reflectivity, transmission, absorption, and electromagnetic field distributions of the cavity.

Within the cavity simulations, the dispersive cavity photon mode interacted with the excitonic resonance through the complex dielectric response of the active layer. By varying the active-layer thickness and DBR design parameters within the model, the cavity mode energy and field confinement could be tuned to overlap with the exciton resonance, thereby enabling access to the strong coupling regime. Once strong coupling conditions were achieved, the layer thicknesses were further optimized to obtain the desired cavity detuning, including both positive and negative detuning configurations.

3.1.2.2. Cavity fabrication

The optimized design was then transferred into fabrication. The bottom DBR mirror was deposited directly onto a quartz substrate and designed to have a higher reflectivity and lower transmission than the top mirror, ensuring asymmetric outcoupling of the cavity mode. The active layer and/or spacer layer were subsequently deposited on top of the bottom mirror by spin coating under the

same conditions described in Section 3.1.1. Finally, the top DBR mirror was deposited over the active layer to complete the cavity structure.

3.1.2.3. Distributed Bragg Reflector Fabrication

Distributed Bragg reflectors (DBRs) were fabricated using an Ångstrom Engineering electron-beam (e-beam) evaporation system (see **Figure 3.3**). In this method, a high-energy electron beam is focused onto a crucible containing the source material, causing localized heating and evaporation. The vapor then condenses onto the substrate under high vacuum, enabling precise deposition of thin films with well-controlled thickness and optical quality.

For the DBRs, alternating layers of silicon dioxide (SiO_2, refractive index $n \approx 1.5$) and titanium dioxide (TiO_2, $n \approx 2.5$) were deposited to form the low- and high-refractive-index materials, respectively. Each layer was deposited with an optical thickness of $\lambda/4$ at the target cavity wavelength, ensuring constructive interference between reflected beams and thus high reflectivity.

Deposition was carried out under a base pressure of $\sim 1 \times 10^{-6}$ mBar to minimize contamination and scattering during film growth. The deposition rates were kept about 2 Å/s, monitored using a quartz crystal microbalance (QCM) for real-time thickness control. The number of layer pairs was adjusted according to the cavity design. Top DBRs were fabricated with 4-8 pairs to allow partial transmission of the cavity mode, while bottom DBRs employed 6-12 pairs to achieve higher reflectivity and ensure asymmetric outcoupling of the cavity mode.

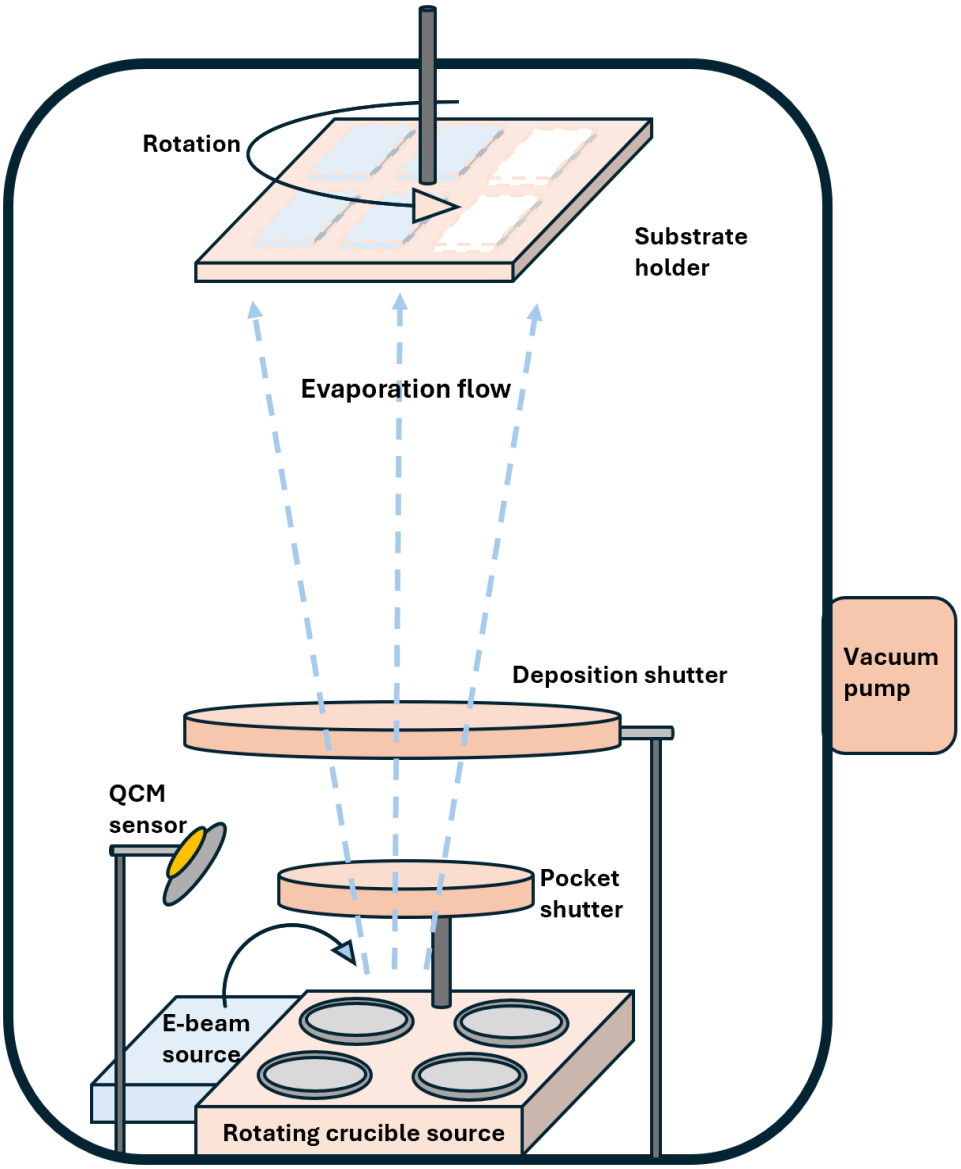

Figure 3.3 *schematic diagram of Ångstrom Engineering electron-beam (e-beam) evaporation system*

3.2. Optical Characterisation Techniques

3.2.1. Steady-state UV-Vis Transmission and Photoluminescence

Steady-state transmission and photoluminescence (PL) measurements of thin-film samples were performed using a Horiba Fluoromax-4 spectrofluorometer. The system is equipped with a vertically mounted, continuous-wave (CW) 150 W ozone-free xenon (Xe) arc lamp as the broadband excitation source. The excitation wavelength was selected using a monochromator incorporating a 1200 lines/mm blazed diffraction grating, providing wavelength-resolved excitation with high spectral purity. Transmission and emission spectra were acquired using an F3031 transmission accessory, allowing accurate collection of transmitted and emitted light from thin-film samples.

For transmission measurements (**Figure 3.4a**), the monochromated light was directed through the thin-film sample mounted on a J1933 solid-sample holder at normal incidence. The transmitted light was then collected directly by the detector, allowing acquisition of the wavelength-dependent transmission spectrum of the film. These measurements were subsequently used to determine the optical absorbance and excitonic absorption features of the BA_2PbI_4 layers.

For photoluminescence measurements (**Figure 3.4b**), the sample was excited using the monochromated Xe lamp beam, while the emitted PL signal from the sample was collected perpendicular to the excitation path to minimize detection of scattered excitation light. The emitted light was subsequently dispersed by a second monochromator before detection using a photomultiplier tube (PMT)-based detector, enabling spectrally resolved PL measurements with high sensitivity.

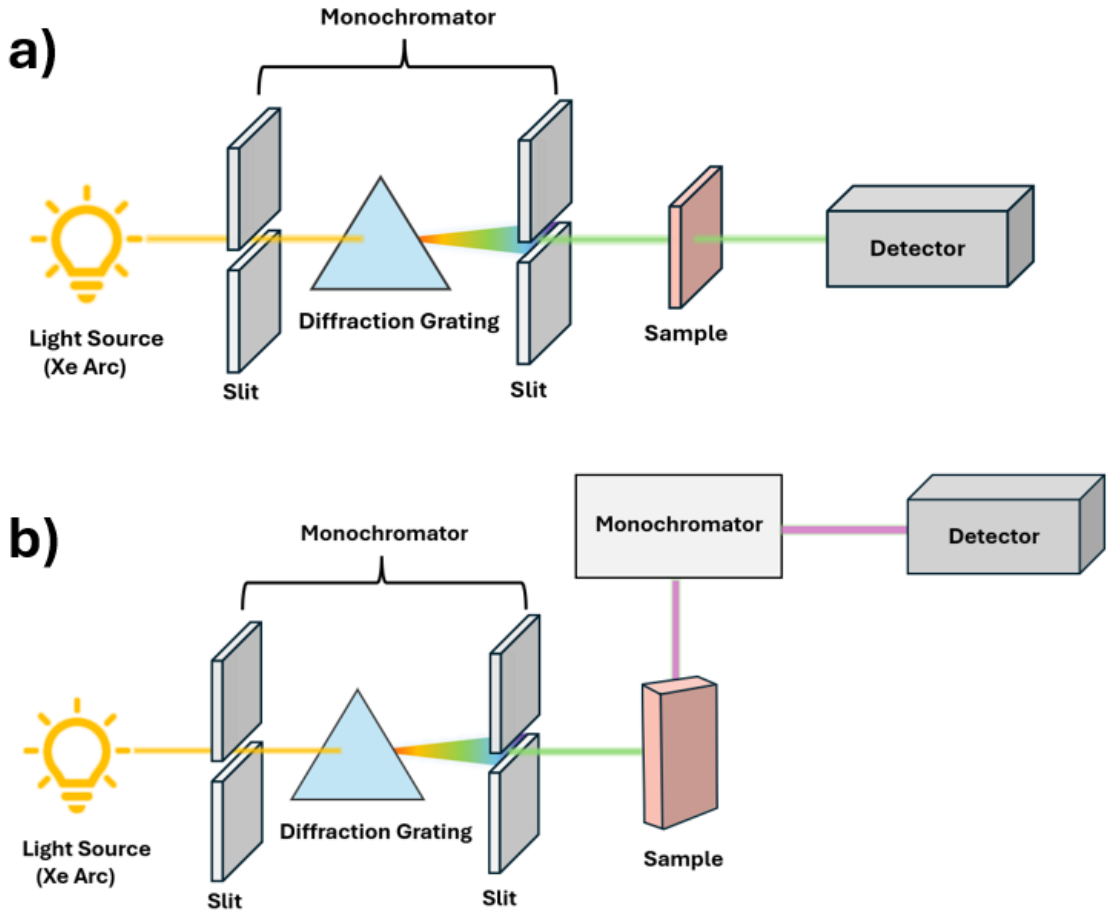

Figure 3.4 *Schematic setup of fluoromax spectrometer for* ***a)*** *UV-Vis transmission and* ***b)*** *emission.*

3.3.2. Optical Constant Measurements

The wavelength-dependent refractive indices of TiO_2 and SiO_2 thin films were determined using spectroscopic ellipsometry. Measurements were performed with a J.A. Woollam ellipsometer system (BASE-160) equipped with EC-400 and M-2000V ellipsometry modules, enabling broadband spectral analysis over the visible range relevant to the DBR stopband.

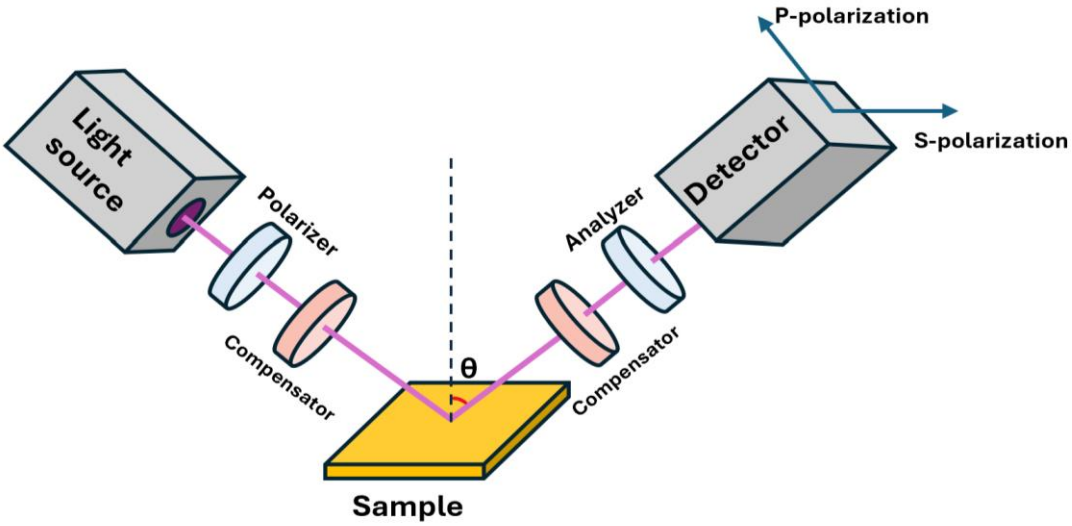

Figure 3.5 *Schematic* configuration *of an ellipsometry for wavelength-dependent refractive index of TiO2 and SiO2.*

Spectroscopic ellipsometry is a non-destructive optical technique that measures changes in the polarization state of light upon reflection from a sample surface. As illustrated schematically in **Figure 3.5**, linearly polarized light is directed onto the sample at an angle of incidence. Upon reflection, the relative amplitude and phase changes between the p-polarized (parallel to the plane of incidence) and s-polarized (perpendicular) components are analyzed. The measured spectra were fitted using an appropriate dispersion model to extract the wavelength-dependent refractive index values of TiO_2 and SiO_2. These optical constants were subsequently used as input parameters for TMR simulations to accurately design the DBR mirrors employed in the microcavity structures.

3.2.3. Low Temperature Photoluminescence

Low-temperature photoluminescence (PL) measurements were performed using an Oxford Instruments Optistat Dry BLV cryostat. Samples were mounted inside the cryostat and cooled to the desired temperature under vacuum conditions. Optical excitation was provided by a CW 405 nm diode laser. The emitted PL was collected at normal incidence using a free-space fibre-coupled collection optics and directed to an Ocean Optics Flame spectrometer for spectral analysis.

3.2.4. Angle-dependent Reflectivity and Photoluminescence

In the strong coupling regime, the interaction between the cavity photon mode and the excitonic transition leads to a characteristic anticrossing, observable as two distinct polariton branches: the lower polariton branch (LPB) and the upper polariton branch (UPB).

In this thesis, angle-dependent reflectivity and photoluminescence (PL) measurements were carried out using a motorized goniometer setup, which allowed automated scanning of the detection angle with high precision. A schematic of the setup is shown in **Figure 3.6**. For reflectivity, broadband illumination was provided by a deuterium-halogen white light source (DH-2000-BAL, Ocean Optics). The output was coupled through an optical fiber to the excitation arm of the goniometer, where a pair of lenses was used to first collimate and then focus the beam onto the sample. The sample was carefully aligned so that its surface was positioned at the intersection of the excitation and collection arms, ensuring that the illuminated spot was also at the focal point of both optical paths. The collection arm contained a pair of lenses to collimate the reflected light and focus it into an optical fiber, which was coupled to an Andor Shamrock SR-303i-A spectrometer with a CCD detector. A linear polarizer could be introduced into the detection path to selectively analyze transverse magnetic (TM) or transverse electric (TE) polarization

components, which is particularly useful for distinguishing mode anisotropy in layered perovskites.

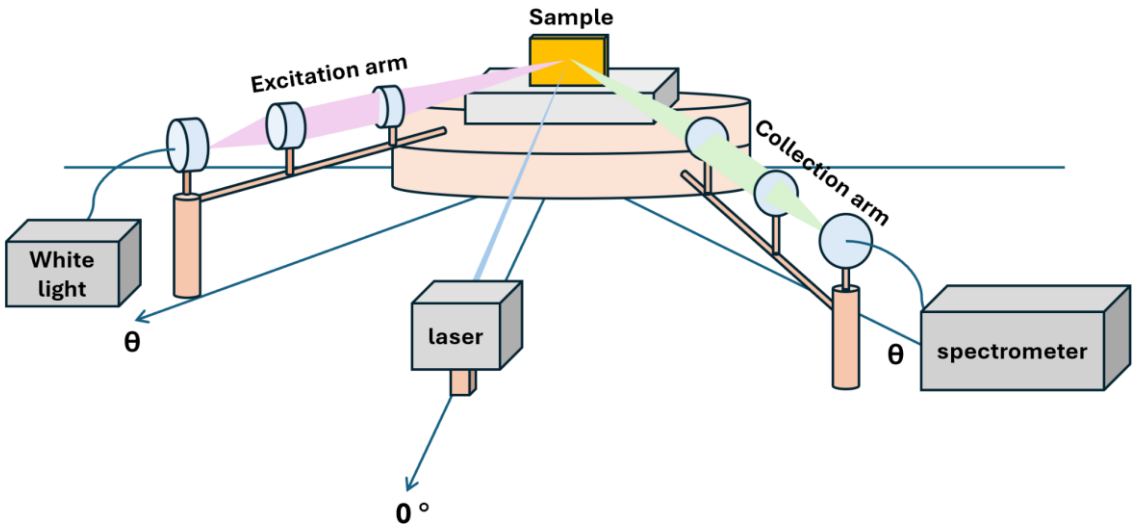

Figure 3.6 *Schematic setup of goniometer for angle-resolved reflectivity and PL of microcavities.*

For PL measurements, a CW 405nm diode laser was used as the excitation source. The laser beam was focused onto the sample from above, i.e., outside the collection path of the goniometer, to avoid direct reflection of the excitation light into the detection fiber. This geometry ensured that only the sample's PL was collected by the spectrometer. This combined setup enabled acquisition of both angle-dependent reflectivity and PL spectra, providing complementary information about the polariton dispersion and verifying the presence of strong coupling.

3.2.5. Time Correlated Single Photon Counting Measurements

Time-resolved photoluminescence (TRPL) measurements were performed using a time-correlated single-photon counting (TCSPC)-based fluorescence lifetime imaging microscopy (FLIM) setup. Samples were excited by a pulsed 485 nm diode laser (PicoQuant) operated at a repetition rate of 1 kHz. The excitation beam was directed into a laser-scanning confocal microscope and focused onto the sample using a 20× air objective, providing both spatial confinement of the excitation spot and effective rejection of out-of-focus emission via the confocal pinhole.

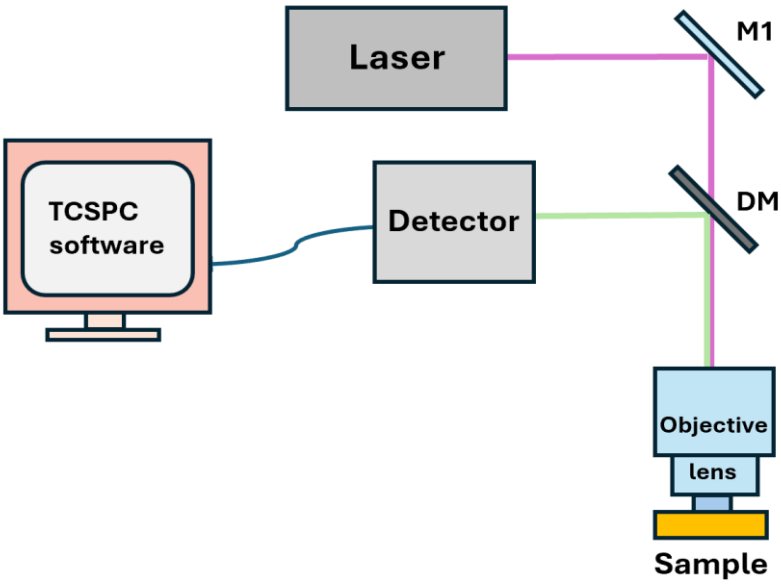

Figure 3.7 *Schematic setup of TCSPC measurements for fluorescence time of 2D perovskite thin films and microcavity.*

The emitted photoluminescence was collected through the same objective and separated from the excitation light using appropriate dichroic mirrors (DM, Semrock FF495-Di03-25×36) and emission filters. The fluorescence signal was then directed to a single-photon-sensitive photomultiplier tube for TCSPC detection. Photon arrival times were recorded relative to the laser trigger and accumulated using TCSPC electronics and software to construct the PL decay traces.

A schematic of the TCSPC/FLIM experimental configuration is shown in **Figure 3.7**. This measurement was done by Dr. Tingxiang Yang (School of Bioscience, The University of Sheffield).

3.2.6. Amplified Spontaneous Emission Measurements

Amplified spontaneous emission (ASE) measurements were performed using a stripe-excitation geometry, as shown in **Figure 3.8**. Excitation was provided by a Teem Photonics Q-switched Nd:YAG laser operating at 355 nm (100 Hz repetition rate, ~350 ps pulse duration). The laser beam was expanded using an aspherical UV lens (f = 100 mm) and shaped into a stripe using a cylindrical lens (CL, f = 25 mm). The excitation stripe was focused onto the sample surface and aligned parallel to the sample edge to enable in-plane waveguiding of the emitted light.

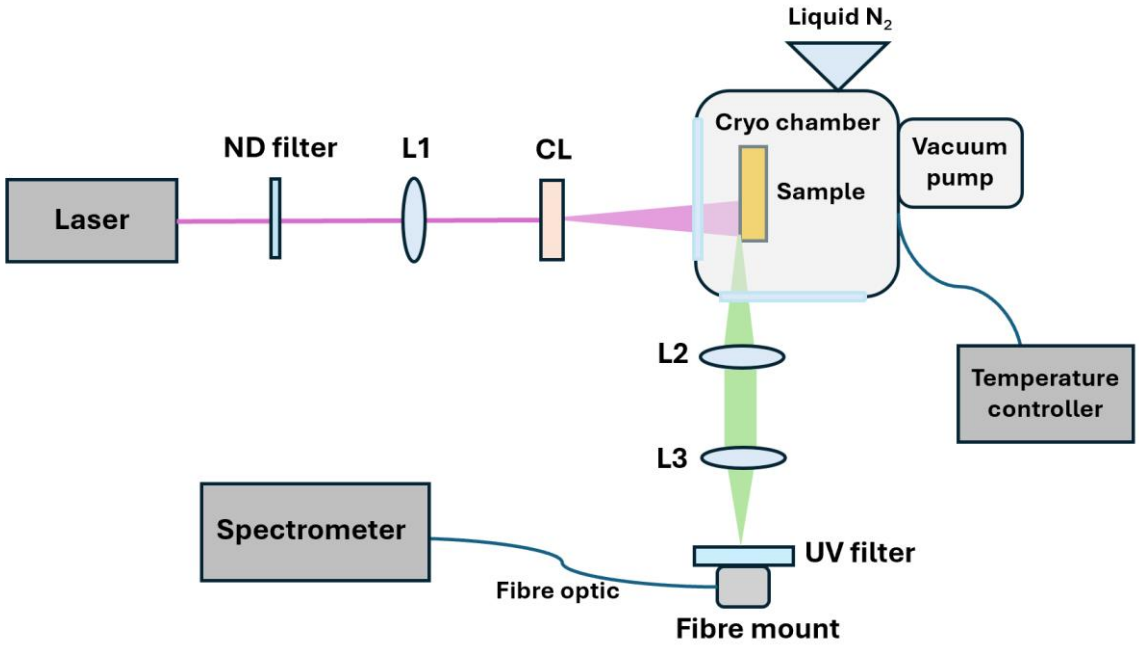

Figure 3.8 *Schematic setup of ASE measurements for 2D perovskite thin films.*

Samples were mounted inside a vacuum cryogenic chamber and cooled using liquid nitrogen, with temperature controlled via an external temperature controller. Emission generated within the pumped stripe region was guided laterally in the thin film and collected from the sample edge using a fibre-coupled collection system. The collected signal was directed into an Andor Shamrock SR-303i spectrograph equipped with a CCD detector, using a 300 lines/mm grating and a 50 μm entrance slit.

Pump fluence was controlled using a variable neutral-density (ND) filter wheel placed in the excitation beam path and calibrated with a Thorlabs power meter. Power-dependent measurements were performed to determine ASE thresholds. These measurements were done with the assistance of Dr. Peter Claronino and Dr. Kyriacos Georgiou (University of Cyprus).

3.2.7. Transient Absorption Measurements

Ultrafast transient absorption (TA) measurements were carried out using a typical pump-probe optical setup in a non-collinear configuration where differential transmission was measured as a function of optical delay between the pump and the probe. The schematic of the setup is shown in **Figure 3.9**. These measurements were carried out at the University of Cyprus in a collaboration with Dr. Emmanouil Lioudakis, Prof. Andreas Othonos, and Dr. Kyriacos Georgiou.

A mode-locked Ti:Sapphire amplifier (Spectra-Physics Spitfire) with a repetition rate of 1 kHz and output energy of 1.3 mJ per pulse generating 100 fs pulses at 800 nm was used as the fundamental beam. A non-linear β-barium borate (BBO) crystal was used to frequency-double the amplifier's output at 400 nm (3.1 eV). A fraction of the fundamental beam was used to generate a supercontinuum light for probing in the ~ 1.1 - 3.1 eV range. An ultrathin high reflector at 800 nm was used to reject the residual fundamental light from the generated white light to eliminate the

possibility of effects by the probe light. Optical elements such as focusing mirrors were utilized to minimize dispersion effects and thus avoid broadening the laser pulse.

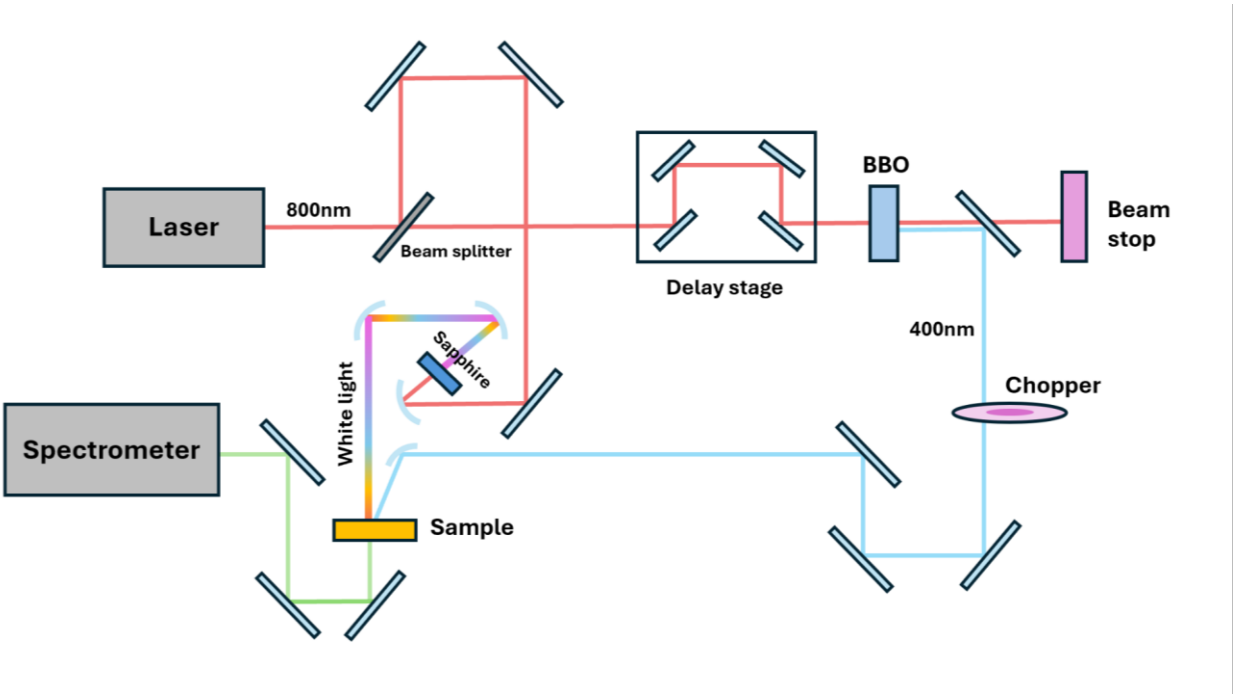

Figure 3.9 *The schematic of the setup of TA measurements.*

In the transmission configuration, the transient signal is expressed as the fractional change in the probe transmission, ΔT/T, as a function of the pump-probe delay time, *t*. This quantity compares the transmitted probe intensity measured with the pump to that obtained in its absence:

$$\frac{\Delta T}{T} = \frac{T_{pump\ on} - T_{pump\ off}}{T_{pump\ off}} \tag{3.5}$$

Here, $T_{pump\ on}$ and $T_{pump\ off}$ denote the transmitted probe signal with and without the pump pulse, respectively.

3.3. Morphology Characterisation Techniques

3.3.1. Dektak Thin Film Thickness Measurements

Film thickness was measured using a Bruker Dektak surface profilometer. **Figure 3.10** presents a schematic of the profilometer setup. Prior to measurement, the thin film was carefully scratched with a razor blade to expose the underlying substrate, and the sample was then mounted on the stage. The Dektak stylus scanned across the scratch under a constant applied force. Changes in the stylus deflection, reflected in variations of the restoring force, were used to determine the film thickness. For each sample, measurements were performed at two separate scratches to evaluate the standard deviation. The resulting thickness values were used to calibrate the deposition process and achieve the target film thicknesses.

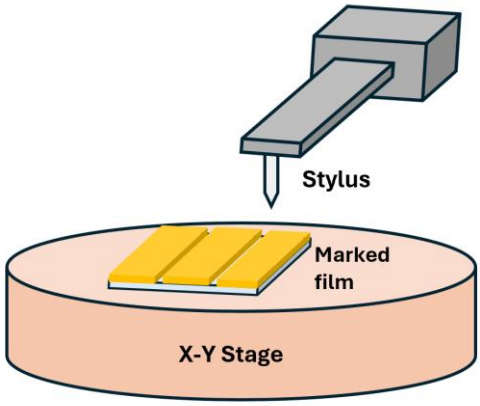

Figure 3.10 *The schematic of the setup of Bruker Dektak surface profilometer.*

3.3.2. Atomic Force Microscopy (AFM)

Surface morphology was characterized using atomic force microscopy (AFM) performed on a Veeco Dimension 3100 system operated in intermittent-contact (tapping) mode. Measurements were carried out using a NuNano Scout 350 silicon cantilever with a nominal spring constant of 42 N m^{-1} and a resonant frequency of approximately 350 kHz. For each sample, two separate regions of 10 × 10 μm^2 were scanned with a lateral resolution of 512 × 512 pixels to ensure representative surface statistics.

Figure 3.11 illustrates a schematic of the AFM operating principle. In tapping mode, an oscillating cantilever periodically interacts with the sample surface. A laser beam is focused onto the backside of the cantilever and reflected onto a four-quadrant photodiode detector, which monitors changes in the oscillation amplitude as the tip scans across the surface topography. The surface morphology is reconstructed by recording the vertical displacement of the cantilever at each lateral (x, y) position, producing a high-resolution topographic AFM image.

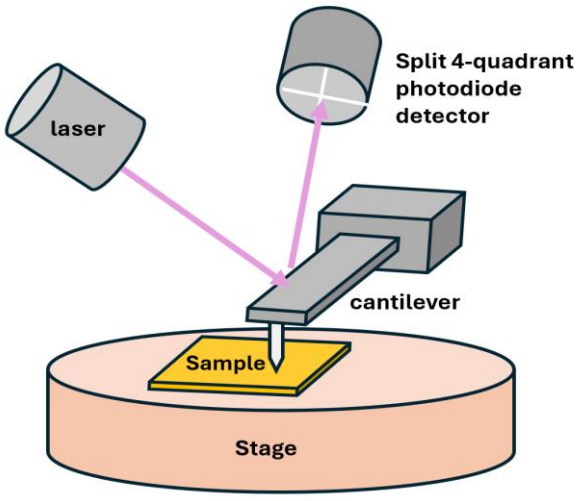

Figure 3.11 *The schematic of the setup of AFM measurements.*

3.3.3. X-Ray Diffraction (XRD)

X-ray diffraction (XRD) measurements were carried out using a PANalytical X'Pert Pro diffractometer equipped with a copper line-focus X-ray tube operated at 45 kV and 40 mA. Diffraction patterns were collected in Bragg-Brentano (θ-2θ) geometry using a one-dimensional detector. The raw data used for perovskite thin films in Chapter 4 was collected by Timothy Thornber.

XRD probes the long-range crystalline order of materials through the coherent scattering of X-rays by electrons in the periodic lattice. Constructive interference occurs when the Bragg condition is satisfied,

$$2dsin\theta = n\lambda \tag{3.6}$$

where d is the lattice plane spacing, θ is the incident (and reflected) angle, λ is the X-ray wavelength, and n is an integer. As the incident angle is scanned, diffraction peaks appear at specific angles corresponding to the allowed lattice spacings of the crystal, providing information on crystal phase, orientation, and structural ordering within the perovskite films.

References

1 M. Fox, and M. Fox, Optical Properties of Solids, Second Edition, Second Edition (Oxford University Press, Oxford, New York, 2010).

2 H. Fujiwara, Spectroscopic Ellipsometry: Principles and Applications (John Wiley & Sons, 2007).

3 J. Tian, D. Cortecchia, Y. Wang, H. Liu, E. Feltri, H. Liu, G. Adamo, and C. Soci, "Phase-change perovskite metasurfaces for dynamic color tuning," Nanophotonics 11(17), 3961–3968 (n.d.).

Chapter 4

Investigating 2D Perovskite Thin Films for Strong Coupling in DBR Microcavities

This chapter focuses on the optimization of BA_2PbI_4 thin films and their integration into optical microcavities to establish a reliable strong-coupling platform. Control over film morphology, crystallinity, and thickness is first addressed, followed by the design and fabrication of DBR cavities spectrally matched to the excitonic resonance. The carrier recombination dynamics in both film and cavity are also examined. These results provide the foundation for the subsequent investigation of amplified spontaneous emission and potential polariton lasing.

4.1. Introduction

Exciton-polaritons are hybrid light-matter quasi-particles formed via strong coupling between cavity photons and excitons, combining a low effective mass inherited from photons and a strong nonlinearity from excitons. These properties enable phenomena like polariton lasing and Bose-Einstein condensation, positioning them as transformative for optoelectronics even at elevated temperatures when using organic semiconducting materials,[1–7] rendering polaritons as good candidates for practical optoelectronic applications.

Two-dimensional (2D) lead halide perovskites, with inorganic $[PbI_6]^{4-}$ layers separated by organic cations (e.g., BA^+, PEA^+), can also be considered as promising candidates due to their unique quantum-well-like layered structure. Their quantum confinement enhances exciton binding

energies up to 200 - 400meV[8,9], stabilizing robust excitons at room temperature - a prerequisite for studying room temperature strong light-matter interactions. Recent reports have demonstrated a variety of nonlinear polariton effects in these materials, underscoring their potential for polariton lasers and quantum optoelectronic devices.[10–16] Despite these advances, achieving room-temperature polariton condensation in 2D perovskites remains elusive. To date, condensation has only been observed at cryogenic temperatures.[17] The main challenge is achieving high film uniformity and reproducibility.

In particular, the fabrication of high-quality perovskite quantum wells (QWs) with atomically precise thickness control and homogeneous composition remains nontrivial due to intrinsic material roughness, which leads to inhomogeneous broadening and interfacial scattering losses, thereby degrading oscillator strength and undermining the strong-coupling regime required for pronounced cavity-enhanced phenomena.[18–20] In addition to material quality, efficient cavity-enhanced light-matter interaction critically depends on precise spectral alignment between the photonic cavity mode and the excitonic transition of the perovskite. The exciton energy in layered perovskites is sensitive to the factors such as composition, lattice strain, and layer thickness[21], placing stringent requirements on both material synthesis and cavity design. Addressing these challenges requires refined synthesis routes for ultra-thin perovskite layers and advanced cavity engineering to ensure stable and reproducible mode confinement.

In this work, we focus on the pure phase n=1 layered perovskite BA_2PbI_4 as the active medium. Although this material is well established as a model 2D perovskite system, its strong light-matter coupling behavior in optical microcavities remains relatively unexplored. Importantly, BA_2PbI_4 offers significant advantages arising from solution-processable fabrication. Here, we enable systematic control over film morphology and thickness through solvent and additive engineering,

and these attributes make BA_2PbI_4 an ideal platform for optimizing excitonic properties and investigating strong coupling and polariton condensation phenomena in perovskite microcavities.

4.2. Results and Discussions

4.2.1. Solvent effect on perovskite thin films for strong coupling

The crystal structure of the Ruddlesden-Popper phase n = 1 BA_2PbI_4 is shown in **Figure 4.1a**, illustrating the layered perovskite framework consisting of corner-sharing $[PbI_6]^{4-}$ octahedra separated by insulating butylammonium (BA^+) spacer cations. The precursor solution was prepared by dissolving PbI_2 (> 99.99%, TCI) and BAI (> 99.99%, Sigma-Aldrich) with a molar ratio 2:1 in dimethylformamide (DMF, > 99.8%, Sigma-Aldrich) and dimethyl sulfoxide (DMSO, > 99.8%, Sigma-Aldrich), respectively, to explore solvent-dependent effects. An incorporation of 18-crown-6 (> 99%, Sigma-Aldrich) at a concentration of 4 mg/mL, a crown ether additive previously demonstrated to enhance the morphological and optoelectronic quality of perovskite films (structure shown in **Figure 4.1b**)[22], was explored in the DMF-based system. Films were deposited using a two-step spin-coating process (1000 rpm for 10 s followed by 4500 rpm for 40 s and subsequently annealed at 100 °C for 15 min to remove residual solvent) inside a N_2 filled glovebox. All films investigated here were fabricated using the same spin-coating protocol described above and exhibit a thickness of approximately 190 nm, as measured using a Dektak profilometer. A relatively higher precursor concentration (0.4M) was intentionally employed to produce thicker films with stronger optical absorption and more clearly resolved surface features. This facilitates a more reliable comparison of solvent-dependent effects on both optical response and morphological characteristics, while also ensuring sufficient signal quality in spectroscopic measurements.

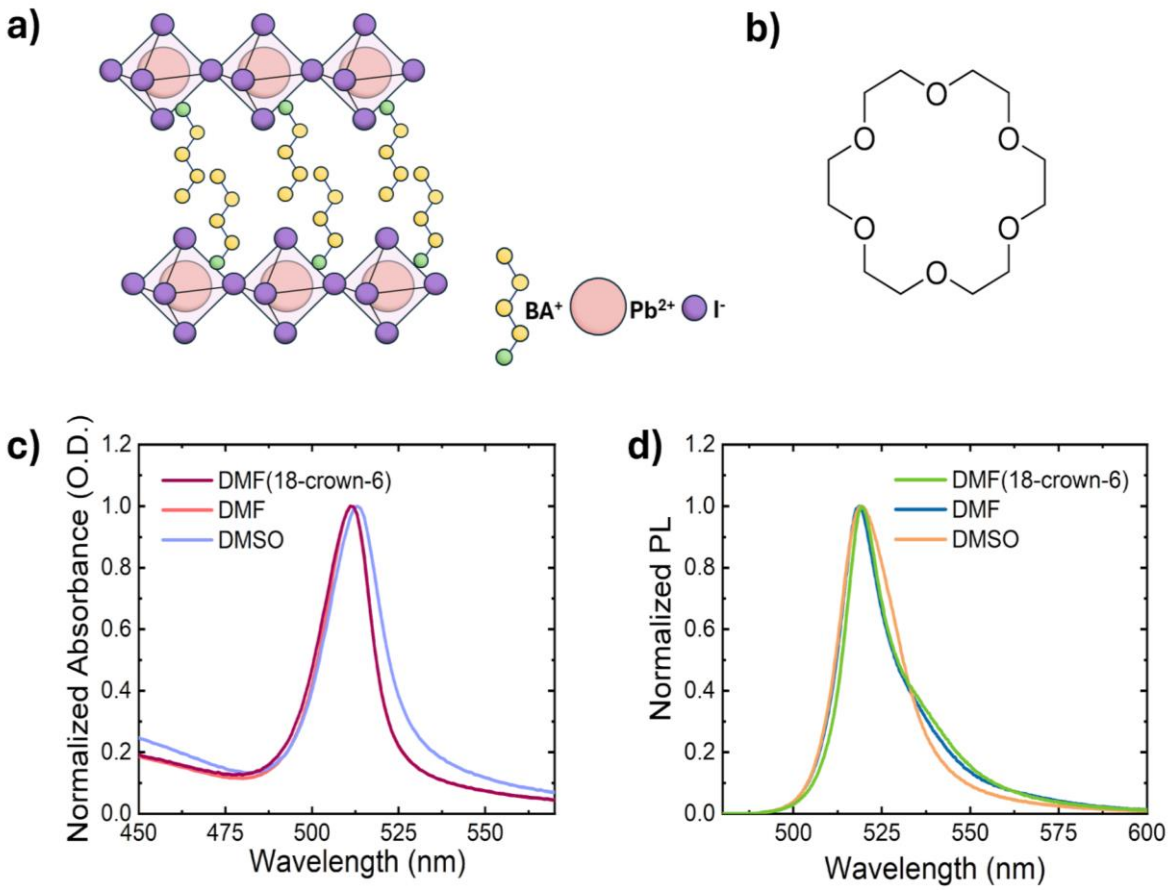

Figure 4.1 a) *Crystal structure of n = 1 BA_2PbI_4;* ***b)*** *chemical structure of 18-crown-6; Normalized* ***c)*** *Absorbance and* ***d)*** *PL of 0.4M n=1 BA_2PbI_4 film using different solvents*

The normalized absorbance and photoluminescence (PL) spectra for the three solvent conditions (DMF, DMF/18-crown-6, and DMSO) are presented in **Figures 4.1c-d.** All films exhibit a pronounced excitonic absorption peak at ~510 nm and a PL maximum at ~ 522 nm, corresponding to a small Stokes shift of ~ 12 nm, indicative of strongly bound excitons and minimal non-radiative relaxation prior to recombination. Notably, the DMF-processed films display a narrower absorbance linewidth compared with those prepared from DMSO, suggesting reduced inhomogeneous disorder and a more well-defined excitonic transition. This indicates that the

solvent environment plays an important role in governing the excitonic quality of BA_2PbI_4 films, which is a key requirement for achieving strong coupling in microcavity structures.

While the optical spectra demonstrates that all solvent systems produce films with well-defined excitonic features, the differences in linewidth and spectral sharpness suggest variations in microstructural quality and crystallization behaviour. To further investigate the solvent-dependent optical properties with surface morphology, grain structure, and crystallographic orientation, Atomic Force Microscopy (AFM) with an area of 10 × 10 μm^2 (**Figure 4.2a–c**) were performed on perovskite films fabricated in DMSO and DMF (with/without 4 mg/mL 18-crown-6), respectively. Furthermore, X-ray diffraction (XRD) measurements were performed only on films in the DMF system to further investigate the additive effect, as discussed in the following section.

From the AFM results, the film processed from DMSO exhibits a highly corrugated surface with pronounced height variations and a dense distribution of small grains, resulting in the largest root-mean-square (RMS) roughness among the three samples (**Figure 4.2a, Table 4.1**). When DMF is used as the processing solvent (**Figure 4.2b, Table 4.1**), the surface becomes noticeably smoother, and the morphology transitions to larger, better-connected crystalline domains, although residual nanoscale height fluctuations remain visible. The introduction of the complexing additive 18-crown-6 into the DMF precursor solution leads to a further suppression of local height inhomogeneities and the formation of substantially larger plate-like grains with well-defined boundaries (**Figure 4.2c, Table 4.1**), which is due to the hydrogen bond between the ammonium of BA and the oxygen atom on the 18-crown-6 results in steric hindrance[23]. This sample exhibits the lowest roughness while simultaneously displaying enlarged lateral grain dimensions, indicating improved grain coalescence and a reduction in intra-grain disorder.

For each sample, AFM measurements were performed over three different surface regions (10 × 10 μm²), and the images presented in **Figure 4.2a–c** represent one representative scan for each condition. The raw AFM data were processed using the software **Gwyddion**, where standard procedures were applied prior to roughness analysis. These included plane leveling to remove sample tilt, line-by-line flattening to correct for scanner drift, and removal of artefacts such as background curvature. The RMS roughness (R_q) was then calculated from the processed height data using[24]

$$R_q = \sqrt{\frac{1}{N}\sum_{i=1}^{N}(z_i - \bar{z})^2} \qquad (4.1)$$

where z_i represents the height at each pixel, $\bar{z}$ is the mean surface height, and N is the total number of data points in the scan. The RMS values reported in **Table 4.1** correspond to the average of the three measured areas for each sample, providing a more reliable assessment of overall surface morphology.

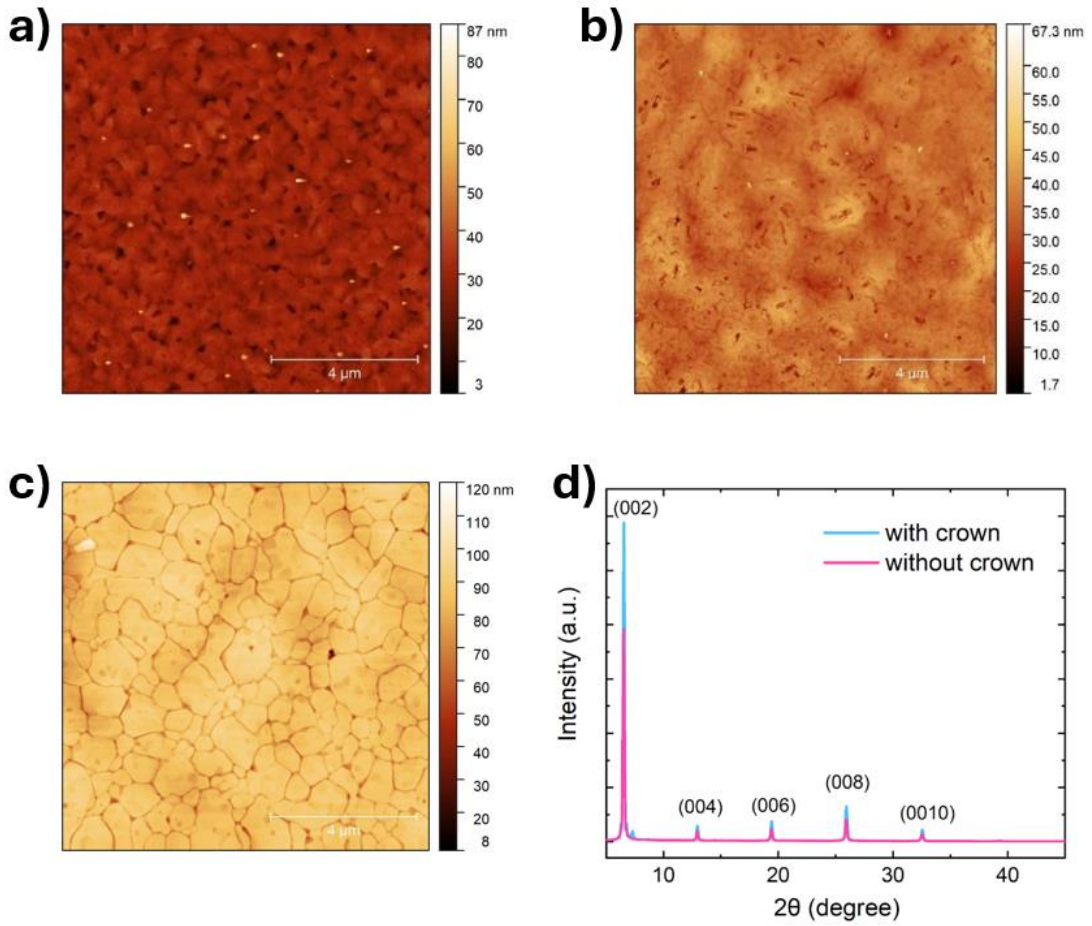

Figure 4.2 *10 x 10 µm^2 AFM on 0.4M n=1 BA_2PbI_4 film using different solvents,* ***a)*** *DMSO,* ***b)*** *DMF,* ***c)*** *DMF with 18-crown-6* ***d)*** *XRD of 0.4M n=1 BA_2PbI_4 film in DMF with/without 18-crown-6.*

Table 4.1. *RMS of the BA_2PbI_4 films using different solvents*

Solvent	RMS
DMSO	4.1nm
DMF	3.74nm
DMF with 18-crown-6	2.1nm

The structural characteristics of the films were further investigated by X-ray diffraction (**Figure 4.2d**). All samples display a dominant (00l) diffraction series, confirming the expected out-of-plane layered orientation of the Ruddlesden-Popper perovskite. However, the film prepared with 18-crown-6 shows markedly stronger (002), (004), (006), and (008) reflections compared with the additive-free DMF film. The enhanced peak intensity and reduced background scattering indicate higher crystallinity, improved layer stacking coherence, and a more uniform orientation distribution. Taken together, the AFM and XRD results demonstrate that 18-crown-6 acts as an effective crystallisation modulator, promoting enlarged grain domains, smoother surfaces, and a more ordered layered structure.

In summary, by comparing the BA_2PbI_4 films with different solvent conditions, we get the most promising spin-coating perovskite recipe for microcavities to achieve strong coupling is DMF with 4mg/ml 18-crown-6. Such sharp excitonic transitions and high crystallinity are favourable for achieving uniform optical fields and enabling strong exciton-photon coupling under ambient conditions in the DBR microcavities studied in the subsequent section, underscoring the synergistic role of solvent selection and additive engineering in optimizing perovskite thin-film properties.

4.2.2. Strong coupling in 2D BA_2PbI_4 microcavities at room temperature

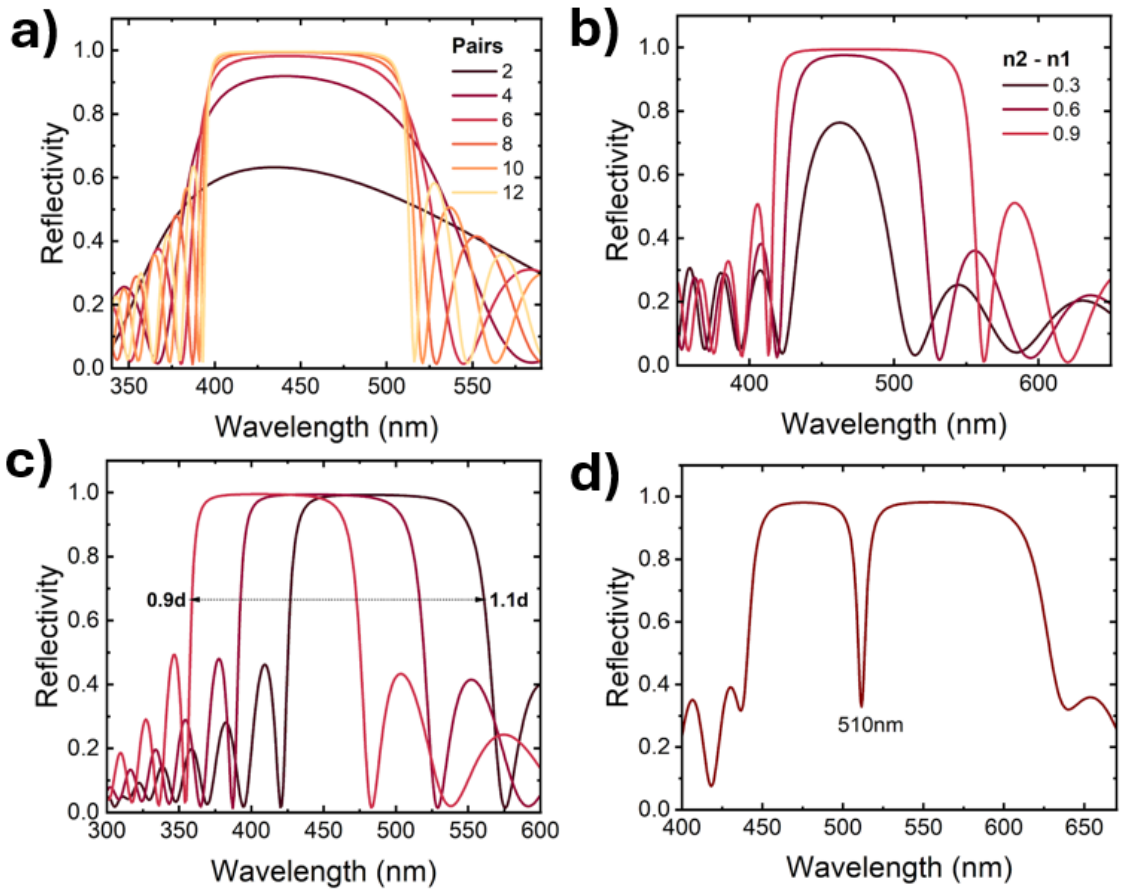

Figure 4.3 a) *Effect of DBR pair number on the mirror stopband;* ***b)*** *Dependence on refractive-index contrast (n_2-n_1);* ***c)*** *Thickness change effect by a factor of 0.9-1.1;* ***d)*** *Optimized DBR design for strong coupling with BA_2PbI_4. All the figures are simulated by the TMR model.*

In a distributed Bragg reflector (DBR) cavity, the confined photon mode arises from constructive interference between multiple reflections at the alternating high- and low-index layers, where maximum reflectance is achieved when each layer satisfies the quarter-wave condition $n_i d_i = \lambda_0/4$, with n_i and d_i being the refractive index and thickness of layer i, and λ_0 the design

wavelength. The DBR stopband width and peak reflectivity are therefore determined by both the index contrast ($n_2 - n_1$) and the number of mirror pairs. To quantitatively evaluate these dependencies, the reflectivity spectra as a function of DBR structural parameters were simulated by the Transfer Matrix Reflectance (TMR) model.

As shown in **Figure 4.3a**, increasing the number of DBR pairs leads to a progressive enhancement of the stopband reflectivity and flattening of the high-reflectance plateau, with 2-pair mirrors exhibiting only weak spectral modulation, whereas ≥ 8 pairs produce reflectivities approaching unity over a broad spectral range. This increases the cavity Quality Factor and photon lifetime, both essential for entering the strong coupling regime. The simulations further demonstrate that the stopband width strongly depends on the refractive-index contrast between the two constituent materials (see **Figure 4.3b**). Larger ($n_2 - n_1$) values generate broader and deeper photonic stopband, thereby providing more robust mode confinement and improved spectral overlap tolerance with the excitonic transition. The effect of thickness (*d*) deviation by a factor of 0.9 - 1.1 were also examined (see **Figure 4.3c**), which shows how the reflectivity of DBR mirrors is shifted to higher or lower wavelengths by altering layer thickness *d*. More details of DBR mirrors were discussed in Chapter 2.

To design a cavity capable of achieving the strong coupling regime, the cavity length must be optimized to ensure the wavelength of the confined photon resonates with the excitonic transition energy of the perovskite material. The optimized DBR structure (**Figure 4.3d**) was designed such that the cavity photon mode is positioned at ~ 510 nm, closely matching the excitonic absorption of BA_2PbI_4. This spectral alignment maximizes the spatial and energetic overlap between the optical field and the excitonic dipole, thereby enhancing the light-matter interaction strength. Here, the high- and low- n materials we used are SiO_2 and TiO_2, whose refractive index values are obtained from ellipsometry, as discussed in 3.1.2.1. At designed wavelength (510 nm), the

refractive index of these two materials is ~ 1.47 and ~ 2.19, respectively. The excitonic contribution was described by fitting a single-peak Lorentz profile to the BA_2PbI_4 extinction coefficient, derived from UV-Vis absorption spectra. Here, the background refractive index of n_{bg} = 1.9 used in the TMR model to generated refractive index for the perovskite was taken from the ref.[25] (The details of how exciton is incorporated into the TMR model were discussed in 3.1.2.1). Once strong coupling was predicted, the layer thicknesses were further optimized to achieve the desired cavity detuning (positive or negative). The model was also used to extract cavity detuning and Rabi splitting values.

A series of 0.1M n = 1 BA_2PbI_4 thin films were fabricated at different spin-coating speeds to optimize the active layer thickness for achieving strong light-matter coupling in practical. The absorbance and PL spectra for films deposited at 3000 - 6000 rpm are shown in **Figures 4.4a-b**. A clear systematic trend is observed: both the optical density and PL intensity increase with decreasing spin speed, confirming that slower spin-coating produces thicker films with a larger optical path length and stronger excitonic absorption. Conversely, higher spin speeds yield thinner films with reduced absorption and weaker emission intensity.

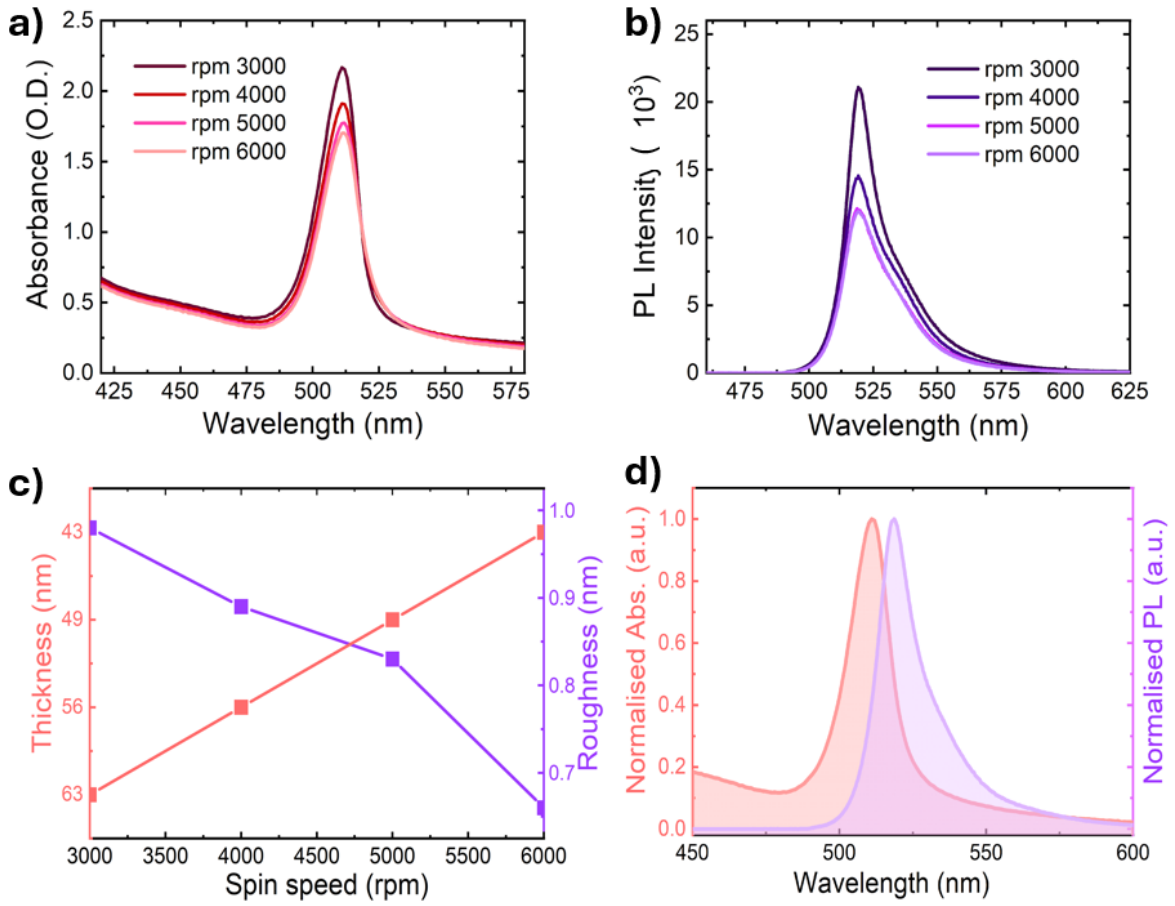

Figure 4.4 a) *Absorbance of BA_2PbI_4 film with different spin-speed;* ***b)*** *PL of 0.1M n=1 BA_2PbI_4 films with different spin-speed;* ***c)*** *thickness and roughness of 0.1M n=1 BA_2PbI_4 films vs. spin-speed;* ***d)*** *Norm abs & PL of 0.1M n=1 BA_2PbI_4 film.*

Figure 4.4c summarises the extracted thickness and RMS surface roughness as a function of spin speed. The film thickness decreases approximately linearly with increasing spin speed, while the roughness shows only modest variation, remaining below ~ 1 nm across all samples. This demonstrates that thickness can be tuned reproducibly through spin-coating without compromising film morphology. Such control is essential for cavity design, as the perovskite layer must be matched to the optical field profile to maximise the spatial overlap between the excitonic oscillator

strength and the cavity photon mode. The absorbance and PL spectra were normalised and plotted in **Figure 4.4d**. The emission linewidth remains narrow (FWHM ≈ 17 nm), which is characteristic of strongly bound Wannier-Mott excitons and is consistent with a high degree of crystallinity and low inhomogeneous disorder in the films.

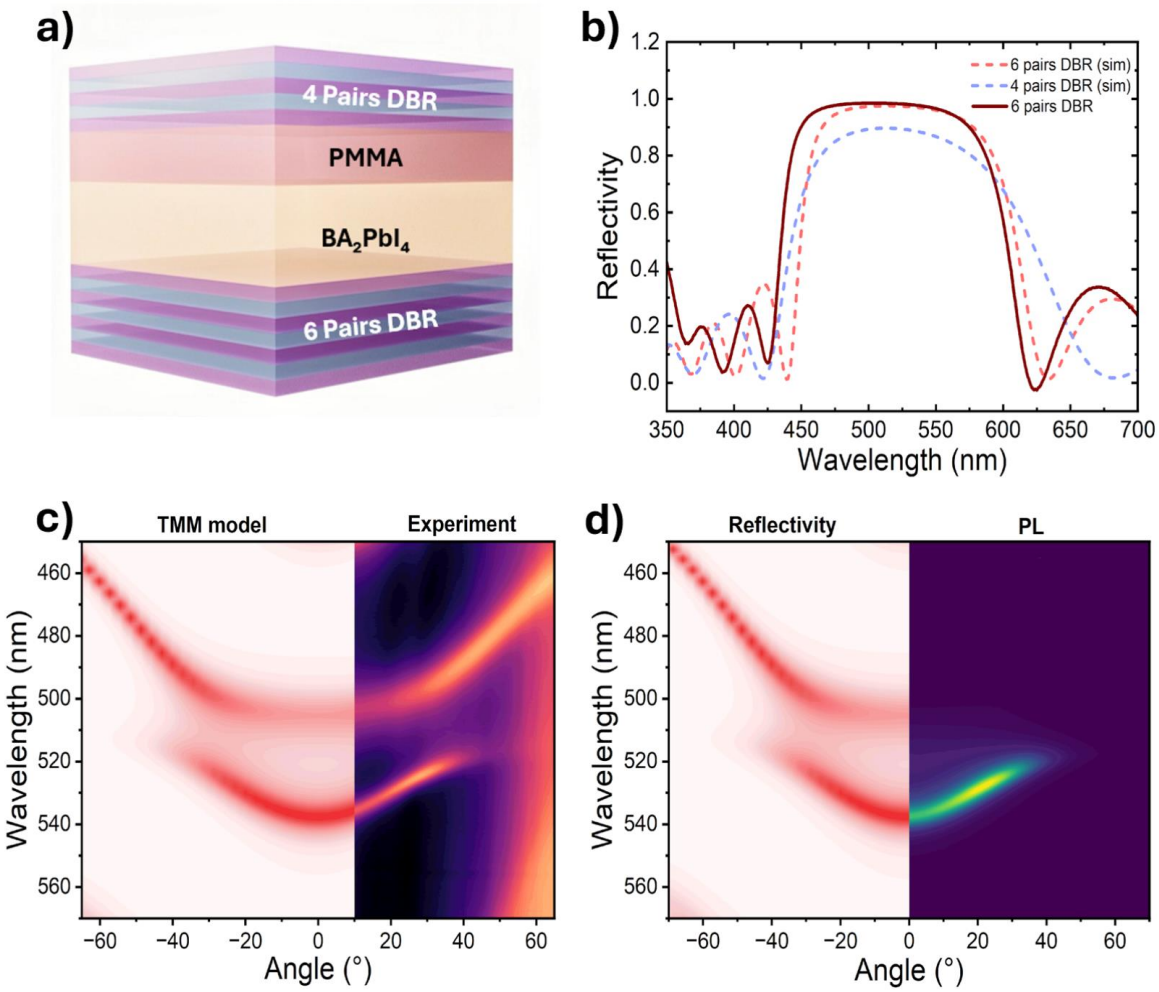

Figure 4.5 ***a)*** *Schematic structure of the cavity* ***b)*** *simulation vs. experiment reflectivity of DBR;* ***c)*** *simulation vs. experiment of angle-resolved reflectivity* ***d)*** *and PL. (The left panel is simulated by the TMR model, the right panel is the experimental data.*

After obtaining the suitable recipe of BA_2PbI_4 thin film for achieving strong coupling, the microcavity were fabricated comprises a spin-coated BA_2PbI_4 active layer, and a poly(methyl methacrylate) (PMMA) layer, sandwiched between top and bottom DBR mirrors, and its structure is shown in **Figure 4.5a**. The thickness of PMMA layer and BA_2PbI_4 used are ~ 123 nm and ~ 54 nm, respectively.

It is worth noting that, the PMMA layer serves multiple critical roles in the device structure. Primarily, it acts as a protective barrier, preserving the integrity of the perovskite film during the deposition of the top DBR mirror. In particular, during ebeam evaporation of the dielectric layers, elevated substrate temperatures can induce degradation of the perovskite layer. This degradation manifests as a significant broadening of the excitonic absorption features and a complete quenching of photoluminescence, indicating disruption of the crystalline structure and increased non-radiative recombination. The introduction of the PMMA layer effectively mitigates these effects by physically isolating the perovskite from direct exposure to the deposition environment. In addition to its protective function, the PMMA layer also contributes to the optical design of the cavity, acting as part of the spacer that defines the effective cavity length and resonance condition. Its inclusion therefore allows for fine-tuning of the cavity mode to achieve the desired exciton–photon detuning, which is essential for exploring polaritonic behaviour in the fabricated microcavities.

Those DBR mirrors were fabricated by electron-beam evaporation (Ångstrom Engineering) of alternating λ/4 layers of SiO_2 (> 99.99%, Sigma–Aldrich) and TiO_2 (> 99.99%, Sigma–Aldrich), with 6 and 4 mirror pairs used to construct the bottom and top DBRs, respectively. The thickness of the alternate layers was carefully designed to allow for a DBR stopband centered at the wavelength of the perovskite's excitonic resonance (~ 510 nm). The simulated reflectivity of the 4 and 6 pairs and experimental for 6 pairs DBRs have shown in **Figure 4.5b**, both stopbands are

from ~ 450 - 600 nm, confirming suitable spectral confinement of the cavity photon mode within the excitonic region.

Angle-resolved white-light reflectivity from the completed microcavity (**Figure 4.5c,** right panel**)** exhibits a pronounced anti-crossing between the angularly dispersive cavity mode and the nearly dispersionless exciton resonance at room temperature, demonstrating the formation of upper and lower polariton branches (UPB/LPB). At normal incidence, the UPB and LPB are observed at approximately 505 nm and 537 nm, respectively, corresponding to a Rabi splitting of ~ 352 meV. The experimental dispersion agrees closely with the corresponding TMR model simulation (**Figure 4.5c**, left panel), indicating that the cavity optical response is well described by the designed structure. **Figure 4.5d** presents the simulated reflectivity dispersion alongside angle-resolved PL, where the emission predominantly follows the LPB, consistent with radiative relaxation into the LPB manifold.

Interestingly, a noticeable difference in linewidth is observed between the simulated and experimental reflectivity spectra (see **Figure 4.5c**). The simulated polariton branches exhibit broader linewidths compared to the experimental data. By extracting the resonance wavelength and full width at half maximum (FWHM) at 10 degrees, the corresponding Q-factors were calculated using $Q = \lambda/\Delta\lambda$, yielding values of ~ 60 for the simulation and ~ 80 for the experiment. This discrepancy likely arises from the excitonic parameters used in the TMR simulation, which were extracted from a thicker (~ 190 nm) BA_2PbI_4 film, whereas the actual cavity contains a much thinner (~ 54 nm) perovskite layer. Although the inhomogeneous broadening term was set to zero in the model, the homogeneous linewidth and oscillator strength were still based on the thicker-film optical response, which may overestimate the excitonic broadening of the thinner cavity film. Therefore, the simulated polariton linewidth can differ from the experimental linewidth, although

the good agreement in dispersion and Rabi splitting indicates that the model captures the essential strong-coupling behaviour.

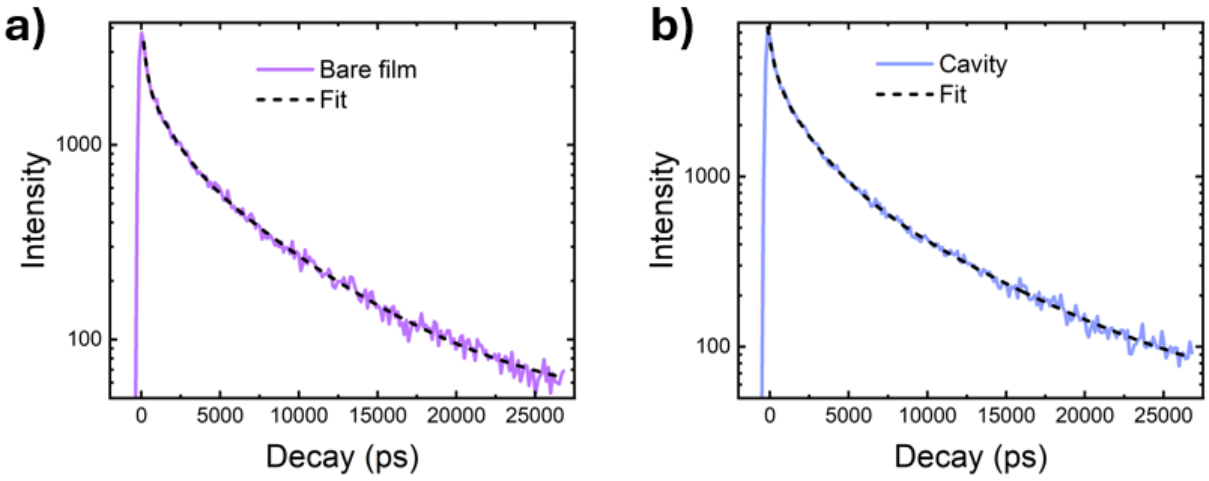

Figure 4.6 *Kinetic trace of the* ***a)*** *bare film and* ***b)*** *the 4/6p DBR cavity in log-scale.*

Time-correlated single-photon counting (TCSPC) measurements were performed to assess the time resolved photoluminescence (TRPL) in both the bare BA_2PbI_4 film and the shown microcavity excited by a 485nm diode laser with a pulse width of 80 ps from Picoquant. The TRPL decay traces and the fitted lifetime are shown in **Figure 4.6a-b**.

The decay curves are best fit with biexponential decay model with a function represented by

$$I = I_0 + \mathrm{A}_1 * exp\left(-\frac{t}{t_1}\right) + \mathrm{A}_2 * exp\left(-\frac{t}{t_2}\right) \qquad (4.2)$$

indicating the presence of at least two characteristic recombination channels: a fast component on the sub-nanosecond timescale (t_1) and a slower dominant component on the few-nanosecond timescale (t_2). To enable quantitative comparison between samples, an intensity-weighted mean lifetime t_{av} was applied, which provides a physically meaningful measure of the mean photon

emission time and appropriately accounts for the dominant contribution of the longer-lived decay component to the total emitted intensity, given by

$$t_{av} = \frac{A_1 t_1^2 + A_2 t_2^2}{A_1 t_1 + A_2 t_2} \tag{4.3}$$

The extracted fitting parameters together with their associated uncertainties are summarized in **Table 4.2**. The reported errors correspond to the standard fitting uncertainties obtained from the nonlinear least-squares biexponential fitting procedure and reflect the confidence of the extracted amplitudes and lifetimes.

	t_1 (ps)	A_1	t_2 (ps)	A_2
film	459.59 ± 14.10	2246.73 ± 34.18	4714.29 ± 104.71	1497.22 ± 24.78
cavity	502.94 ± 14.17	3287.36 ± 60.22	4166.77 ± 84.81	2873.71 ± 49.06

***Table 4.2**. Fitting parameters of the decay kinetics of the film and the cavity.*

Using this approach, the bare BA_2PbI_4 film exhibits an average lifetime of ~ 4.17 ns. In contrast, the microcavity sample shows a reduced average lifetime of ~ 3.14 ns, indicating an acceleration of the radiative decay process when the perovskite layer is embedded within the optical cavity, consistent with the Purcell effect.

Interestingly, in our transient absorption (TA) measurements (discussed in Chapter 6), all optically active exciton and polariton populations decay within ~ 100 ps, after which no bleach signal is observed. The nanosecond-scale PL decay detected by TCSPC therefore likely originates from relaxed excitonic populations that remain weakly emissive but no longer contribute significantly to the TA bleach signal. In this context, the fast decay component (t_1) is unlikely to arise from

direct polariton recombination and may instead be associated with radiative recombination of weakly localized or shallow trapped excitons that persist beyond the ultrafast relaxation regime. The slower component (t_2) is more consistent with longer-lived localized excitonic states, dark excitons, or defect-assisted radiative recombination pathways. Consequently, the long-lived emission observed in TCSPC is unlikely to originate from delayed reservoir-to-polariton scattering or direct LPB radiative decay. It should be noted that TCSPC is limited by the instrument response function (IRF), meaning that ultrafast processes occurring on timescales shorter than ~ 200 ps cannot be resolved. Consequently, TCSPC does not capture the initial carrier thermalization, exciton formation, or early-time many-body interactions, which are instead probed using the femtosecond pump-probe measurements discussed in Chapter 6.

4.3. Conclusion

In this chapter, a systematic strategy has been developed to optimize pure phase n = 1 BA_2PbI_4 thin films and DBR microcavities for achieving strong exciton-photon coupling. By combining solvent engineering, additive-assisted crystallization, and thickness control through spin-coating, highly uniform BA_2PbI_4 films with sharp excitonic resonances and low surface roughness were obtained. In particular, DMF-processed films incorporating 18-crown-6 exhibit enlarged grain sizes, improved crystallinity, and reduced inhomogeneous broadening, providing an optimal excitonic platform for cavity integration.

Using these optimized films, high-quality DBR microcavities were designed via transfer-matrix modelling and experimentally realized with well-defined photonic stopbands matched to the BA_2PbI_4 excitonic transition. Angle-resolved reflectivity measurements reveal a clear anti-crossing between the cavity photon mode and the exciton resonance at room temperature, demonstrating

the formation of upper and lower polariton branches and confirming that the system operates in the strong-coupling regime. The excellent agreement between experiment and simulation highlights the reliability of the cavity design and validates the chosen material and structural parameters.

TRPL measurements further show that embedding BA_2PbI_4 within the microcavity modifies the recombination dynamics, leading to a modest but reproducible reduction in the average PL lifetime compared to the bare film. This lifetime shortening reflects an altered photonic density of states and Purcell-enhanced radiative decay efficiency within the cavity environment. Importantly, when considered alongside ultrafast transient absorption measurements discussed in Chapter 6, the nanosecond-scale PL decay is likely attributed to long-lived emissive excitonic reservoirs (including free, dark, or weakly localized excitons) rather than to polariton population dynamics.

Taken together, these results establish a robust strong-coupling platform based on BA_2PbI_4 microcavities, while simultaneously revealing intrinsic limitations in carrier relaxation and population redistribution that hinder the buildup of a macroscopic polariton population. This finding motivates a complementary investigation of optical gain and stimulated emission in the absence of a cavity, where excitonic amplification can be examined without the constraints imposed by polariton relaxation pathways.

References

1 J.D. Plumhof, T. Stöferle, L. Mai, U. Scherf, and R.F. Mahrt, "Room-temperature Bose–Einstein condensation of cavity exciton–polaritons in a polymer," Nature Mater 13(3), 247–252 (2014).

2 K.E. McGhee, A. Putintsev, R. Jayaprakash, K. Georgiou, M.E. O'Kane, R.C. Kilbride, E.J. Cassella, M. Cavazzini, D.A. Sannikov, P.G. Lagoudakis, and D.G. Lidzey, "Polariton condensation in an organic microcavity utilising a hybrid metal-DBR mirror," Sci Rep 11(1), 20879 (2021).

3 S. Kéna-Cohen, and S.R. Forrest, "Room-temperature polariton lasing in an organic single-crystal microcavity," Nature Photon 4(6), 371–375 (2010).

4 J. Keeling, and S. Kéna-Cohen, "Bose–Einstein Condensation of Exciton-Polaritons in Organic Microcavities," Annual Review of Physical Chemistry 71(Volume 71, 2020), 435–459 (2020).

5 Z. Jiang, A. Ren, Y. Yan, J. Yao, and Y.S. Zhao, "Exciton-Polaritons and Their Bose–Einstein Condensates in Organic Semiconductor Microcavities," Advanced Materials 34(4), 2106095 (2022).

6 K.S. Daskalakis, S.A. Maier, and S. Kéna-Cohen, "Spatial Coherence and Stability in a Disordered Organic Polariton Condensate," Phys. Rev. Lett. 115(3), 035301 (2015).

7 T. Cookson, K. Georgiou, A. Zasedatelev, R.T. Grant, T. Virgili, M. Cavazzini, F. Galeotti, C. Clark, N.G. Berloff, D.G. Lidzey, and P.G. Lagoudakis, "A Yellow Polariton Condensate in a Dye Filled Microcavity," Advanced Optical Materials 5(18), 1700203 (2017).

8 K. Tanaka, T. Takahashi, T. Kondo, T. Umebayashi, K. Asai, and K. Ema, “Image charge effect on two-dimensional excitons in an inorganic-organic quantum-well crystal,” Phys. Rev. B 71(4), 045312 (2005).

9 T. Ishihara, X. Hong, J. Ding, and A.V. Nurmikko, “Dielectric confinement effect for exciton and biexciton states in PbI4-based two-dimensional semiconductor structures,” Surface Science 267(1), 323–326 (1992).

10“Structural and spectral dynamics of single-crystalline Ruddlesden-Popper phase halide perovskite blue light-emitting diodes,” Science Advances, (n.d.).

11 T. Wang, Z. Zang, Y. Gao, C. Lyu, P. Gu, Y. Yao, K. Peng, K. Watanabe, T. Taniguchi, X. Liu, Y. Gao, W. Bao, and Y. Ye, “Electrically Pumped Polarized Exciton-Polaritons in a Halide Perovskite Microcavity,” Nano Lett. 22(13), 5175–5181 (2022).

12 R. Tao, K. Peng, L. Haeberlé, Q. Li, D. Jin, G.R. Fleming, S. Kéna-Cohen, X. Zhang, and W. Bao, “Halide perovskites enable polaritonic XY spin Hamiltonian at room temperature,” Nat. Mater. 21(7), 761–766 (2022).

13 R. Su, A. Fieramosca, Q. Zhang, H.S. Nguyen, E. Deleporte, Z. Chen, D. Sanvitto, T.C.H. Liew, and Q. Xiong, “Perovskite semiconductors for room-temperature exciton-polaritonics,” Nat. Mater. 20(10), 1315–1324 (2021).

14 Y. Liang, Q. Shang, Q. Wei, L. Zhao, Z. Liu, J. Shi, Y. Zhong, J. Chen, Y. Gao, M. Li, X. Liu, G. Xing, and Q. Zhang, “Lasing from Mechanically Exfoliated 2D Homologous Ruddlesden–Popper Perovskite Engineered by Inorganic Layer Thickness,” Advanced Materials 31(39), 1903030 (2019).

15 L. Lei, Q. Dong, K. Gundogdu, and F. So, “Metal Halide Perovskites for Laser Applications,” Advanced Functional Materials 31(16), 2010144 (2021).

16 I. Georgakilas, D. Tiede, D. Urbonas, R. Mirek, C. Bujalance, L. Caliò, V. Oddi, R. Tao, D.N. Dirin, G. Rainò, S.C. Boehme, J.F. Galisteo-López, R.F. Mahrt, M.V. Kovalenko, H. Miguez, and T. Stöferle, “Room-temperature cavity exciton-polariton condensation in perovskite quantum dots,” Nat Commun 16(1), 5228 (2025).

17 L. Polimeno, A. Fieramosca, G. Lerario, M. Cinquino, M. De Giorgi, D. Ballarini, F. Todisco, L. Dominici, V. Ardizzone, M. Pugliese, C.T. Prontera, V. Maiorano, G. Gigli, L. De Marco, and D. Sanvitto, “Observation of Two Thresholds Leading to Polariton Condensation in 2D Hybrid Perovskites,” Advanced Optical Materials 8(16), 2000176 (2020).

18 A. Brehier, R. Parashkov, J.S. Lauret, and E. Deleporte, “Strong exciton-photon coupling in a microcavity containing layered perovskite semiconductors,” Appl. Phys. Lett. 89(17), 171110 (2006).

19 M. Laitz, A.E.K. Kaplan, J. Deschamps, U. Barotov, A.H. Proppe, I. García-Benito, A. Osherov, G. Grancini, D.W. deQuilettes, K.A. Nelson, M.G. Bawendi, and V. Bulović, “Uncovering temperature-dependent exciton-polariton relaxation mechanisms in hybrid organic-inorganic perovskites,” Nat Commun 14(1), 2426 (2023).

20 T. Fujita, Y. Sato, T. Kuitani, and T. Ishihara, “Tunable polariton absorption of distributed feedback microcavities at room temperature,” Phys. Rev. B 57(19), 12428–12434 (1998).

21 K. As’ham, A.M. Berhe, I.A.M. Al-Ani, H.T. Hattori, and A.E. Miroshnichenko, “Recent advances in exciton-polariton in perovskite,” OES 4(9), 250001–20 (2025).

22 J.H. Warby, B. Wenger, A.J. Ramadan, R.D.J. Oliver, H.C. Sansom, A.R. Marshall, and H.J. Snaith, “Revealing Factors Influencing the Operational Stability of Perovskite Light-Emitting Diodes,” ACS Nano 14(7), 8855–8865 (2020).

23 Y. Cao, N. Wang, H. Tian, J. Guo, Y. Wei, H. Chen, Y. Miao, W. Zou, K. Pan, Y. He, H. Cao, Y. Ke, M. Xu, Y. Wang, M. Yang, K. Du, Z. Fu, D. Kong, D. Dai, Y. Jin, G. Li, H. Li, Q. Peng, J. Wang, and W. Huang, “Perovskite light-emitting diodes based on spontaneously formed submicrometre-scale structures,” Nature 562(7726), 249–253 (2018).

24“Characterization Of Membrane Distillation Membranes By Tapping Mode Atomic Force Microscopy,” in Recent Advances in Multidisciplinary Applied Physics, (Elsevier Science Ltd, 2005), pp. 141–148.

25 J. Tian, D. Cortecchia, Y. Wang, H. Liu, E. Feltri, H. Liu, G. Adamo, and C. Soci, “Phase-change perovskite metasurfaces for dynamic color tuning,” Nanophotonics 11(17), 3961–3968 (n.d.).

Chapter 5

Amplified Spontaneous Emission: Towards Polariton Condensation in Strongly Coupled BA_2PbI_4 Microcavities

In this chapter, amplified spontaneous emission (ASE) measurements in pure phase $n = 1$ BA_2PbI_4 thin films with 2 different geometries and power-dependent PL in strongly coupled microcavities are investigated at low temperatures. While clear ASE behavior is observed in BA_2PbI_4 films, no signatures of polariton condensation are detected in microcavity structures, even with increased cavity quality factors. These results highlight the critical role of polariton relaxation dynamics and motivate the ultrafast spectroscopic studies presented in the following chapter.

5.1. Introduction

Ruddlesden-Popper layered perovskites have emerged as promising materials for strongly coupled light-matter systems owing to their large exciton binding energies, strong oscillator strengths, and robust excitonic character. In the previous chapter, we demonstrated that carefully optimised BA_2PbI_4 films embedded in DBR cavities support strong exciton-photon coupling, confirming the formation of exciton-polaritons. However, the onset of polariton lasing is not guaranteed by strong coupling alone, but is instead governed by carrier relaxation, exciton reservoir dynamics, and the

competition between stimulated emission pathways. To understand these processes, it is first necessary to examine how gain and stimulated emission develop in the uncoupled thin-film regime.

Lasing and ASE in layered quasi-2D perovskites have been reported across a variety of material systems[1–4], establishing that these materials are capable of supporting optical gain. However, in pure phase 2D perovskite, the ASE and lasing demonstrations were only realised in high-quality single crystals of BA_2PbI_4 so far[5]. Leyden *et al.* reported ASE in spin-coated quasi-2D $(PEA)_2(MA)_{n-1}Pb_nI_{3n+1}$ thin films, where ASE was observed only in samples containing large-n domains ($n > 12$) and the threshold decreased with increasing n.[6] This behaviour was attributed to cascade energy and charge transfer from wide-bandgap small-n domains into lower-bandgap large-n phases, where population inversion is preferentially established. Similar observations have been reported in other quasi-2D systems, particularly at room temperature, where efficient inter-phase carrier funneling enables ASE only in mixed-phase or high-n films.[7–9]

In contrast, low-n 2D perovskites are difficult to exhibit ASE especially at ambient temperature, which researchers believe this is attributed to the presence of bulky organic spacer layers that inhibit out-of-plane carrier transport and restrict carrier delocalisation across the inorganic perovskite layers[9]. Temperature-dependent ASE studies have further shown that the threshold is strongly influenced by exciton localisation and exciton-phonon scattering, while morphology-controlled films reveal that smoother, highly oriented thin films display significantly lower thresholds due to faster and more complete population build-up[10,11]. These results collectively highlight that ASE formation is governed by the interplay between materials composition, exciton relaxation, and structural disorder - all of which are also central to polariton relaxation and condensation in strongly coupled microcavities.

Architectural approaches have also been explored to enhance gain and modify guided-mode confinement. Polymer-perovskite multilayers and membrane structures have been shown to exhibit

lower ASE thresholds and enhanced emission intensity due to slab-waveguide confinement and increased modal overlap with the gain region[12]. The multilayer stacks of $CsPbBr_3$ and cellulose acetate deposited on quartz substrates in particular display a minimum ASE threshold near approximately 2.5 pairs, attributed to enhanced optical absorption and more efficient confinement of guided modes within the active region. Employing these optimized waveguide structures also ensures that the optical properties remain unaffected by electronic interactions between the perovskite emitter layers.

Within this broader context, the present chapter investigates ASE in pure phase n = 1 2D BA_2PbI_4 thin films in two different geometries (single layer and bilayer), and power-dependent PL in its DBR-based microcavities at cryogenic temperature, in order to probe optical nonlinear response in both uncoupled and strongly coupled regimes.

5.2. Results and Discussion

5.2.1. Temperature-dependent Photoluminescence and Amplified Spontaneous Emission in BA_2PbI_4 films

We firstly performed the temperature-dependent photoluminescence (PL) measurements on the bare BA_2PbI_4 thin film to examine the evolution of excitonic emission across different structural regimes by using a 405 nm diode laser (see **Figure 1a**). At room temperature, the PL band is at ~ 523 nm (RT) which is attributed to free-exciton emission. As the temperature decreases, the main excitonic emission undergoes a pronounced blueshift to ~ 490 nm (LT). This phase change behavior is consistent with the expected increase in bandgap at low temperature, driven by the increase in PbI_6^{4-} octahedral tilting, which has been observed in many previous 2D perovskite

studies.[13–15] In 2D BA_2PbI_4, the valence band maximum (VBM) originates from the antibonding interaction between Pb 6s and I 5p orbitals, as discussed in Chapter 2, Section 2.2. As the Pb-I-Pb bond angle increases, the overlap and consequently the antibonding coupling between the Pb 6s and I 5p orbitals decreases. This reduction stabilizes the VBM, shifting it to lower energy and resulting in a less dispersive valence band.[16]

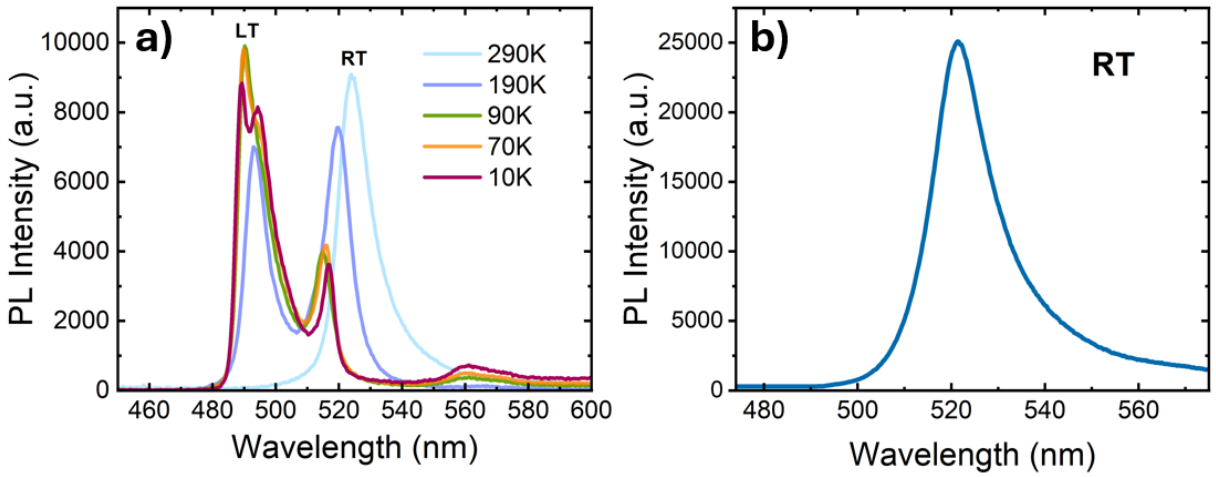

Figure 5.1 a) *Temperature-dependent PL of n = 1 BA_2PbI_4 thin films. PL spectra measured from 290 K to 10 K, showing a progressive blueshift of the main excitonic emission from ~ 523 nm to ~ 490 nm.* ***b)*** *ASE measurement on n = 1 BA_2PbI_4 thin film at RT under 300uW pump, no ASE peak was observed.*

Notably, the peak at around 515 nm remains even down to 10 K, which we believe this peak belongs to the RT phase due to an incomplete phase transition, and this has also been observed in previous research[17]. Here, a clear broad band at around 560 nm has been attributed to self-trapped exciton states in other studies, due to strong phonon coupling with the distorted soft crystal structure and/or in extrinsic defect states.[18–21] The emission from those self-trapped excitons are more pronounced as the temperature decreased. Interestingly, below ~ 70 K, the emission feature

near 490 nm further splits into two distinct peaks at ~ 488 nm and ~ 494 nm. The reason for emergence of this fine structure is unclear, however we suggest it could result from the enhanced anisotropy in the low-temperature phase.

To investigate the optical gain properties, Amplified Spontaneous Emission (ASE) on bare $n = 1$ BA_2PbI_4 thin films were firstly carried out at room temperature by using a Teem Photonics pulsed Q-switched 355 nm Nd:YAG laser (PNV-M02510-1×0). However, only single PL was observed, and no ASE peak or threshold behavior were detected at room temperature as expected, even at the maximum pump power (~ 300 μW), as shown in **Figure 5.1b**.

We then performed ASE measurements at 77 K where the excitonic transitions are better resolved. Here, two sample geometries are used: a bare BA_2PbI_4 thin film (~ 210 nm) and a 2.5-pair BA_2PbI_4 (~ 150 nm)/PMMA (~ 80 nm) bilayer, as shown in **Figure 5.2a, b**. The bilayer structure functions as a planar waveguide, consistent with previous reports in the literature[12], and is expected to enhance in-plane optical confinement and stimulated emission.

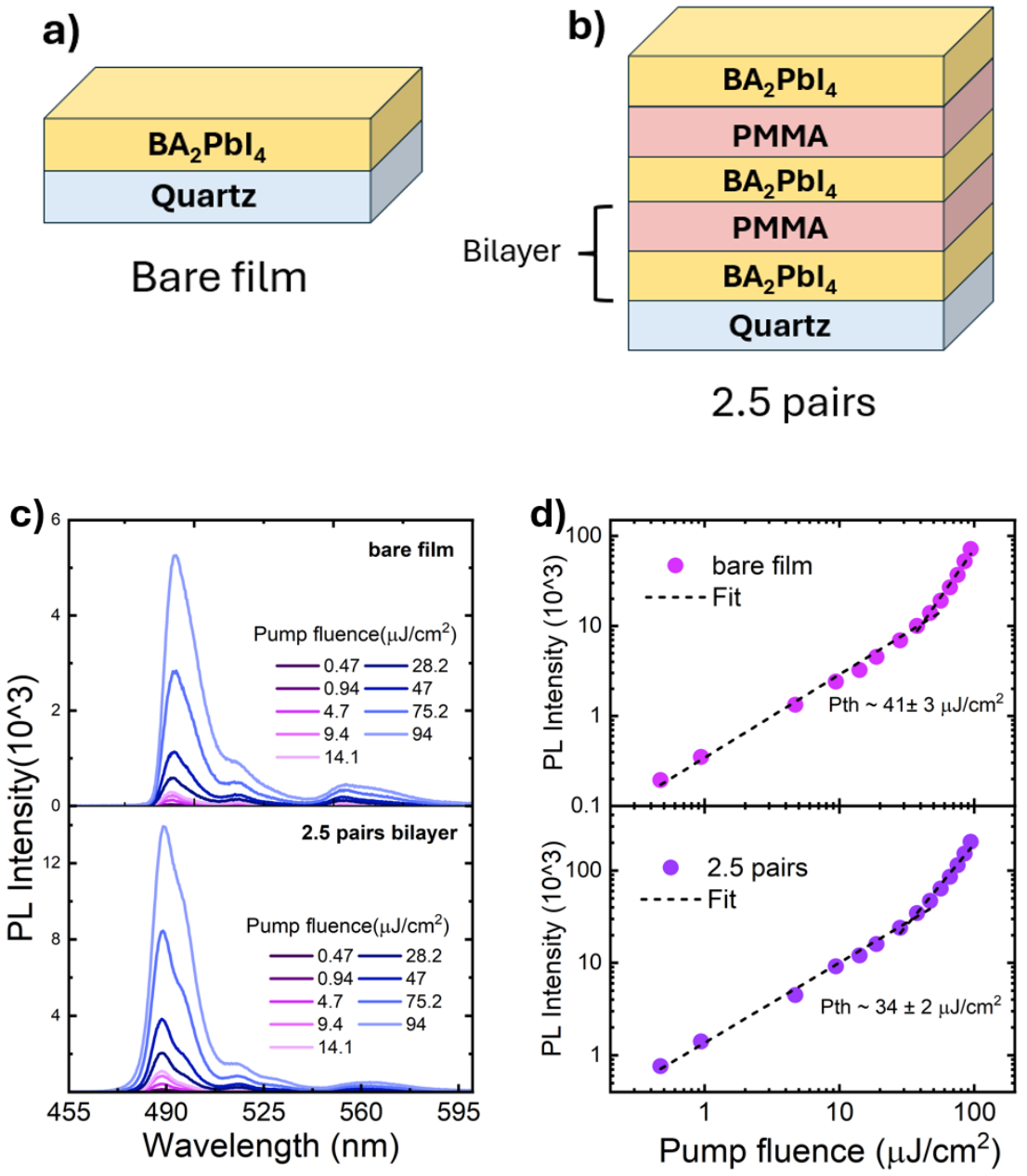

Figure 5.2 a-b) *Schematic figure of bare BA_2PbI_4 film and 2.5 pairs BA_2PbI_4/PMMA bilayer.* ***c)*** *Pump-dependent PL of bare film and 2.5 pairs bilayer at 77 K.* ***d)*** *Log-scale integrated PL intensity as a function of pump fluence. A clear nonlinear transition occurs at ~ 41 ± 3 μJ/cm² for the bare film and ~ 34 ± 2 μJ/cm² for the bilayer, marking the ASE threshold, P_{th}.*

A series of power-dependent PL spectra was collected for both samples (**Figure. 5.2c**). In each case, the emission is dominated by a strong excitonic band near 490 nm, accompanied by a smaller shoulder near ~ 515 nm which we believe it is a transition state from higher temperature exciton state, and a weak, broader low-energy band around ~ 560 nm from defects which becomes clearer at low temperature. To evaluate the onset of ASE, the main excitonic emission band was isolated and integrated over the range 480-504 nm. The resulting integrated intensity in log-scale was plotted as a function of pump fluence (**Figure 5.2d**). In both structures, the intensity initially follows a near-linear dependence on excitation density (slope ≈ 0.92 for the bare film and 0.87 for the 2.5-pair bilayer), characteristic of spontaneous radiative recombination. Above a critical excitation flux, however, the response transitions into a superlinear regime (slope ≈ 2.15 for the bare film and 1.76 for the bilayer), signalling the emergence of stimulated emission and optical gain. The ASE threshold fluence (P_{th}) was determined from the intersection of the linear fits below and above threshold, yielding values of ~ 41 ± 3 μJ/cm² for the bare film and ~ 34 ± 2 μJ/cm² for the bilayer. The reported uncertainties were estimated from variations in the extracted intersection point when slightly adjusting the fitting ranges used for the linear regressions. The reduced threshold in the bilayer is attributed to the enhanced optical confinement and extended in-plane propagation length provided by the waveguiding geometry.

The evolution of the emission band near 480-505 nm in the bare film and 2.5-pair BA_2PbI_4/PMMA bilayer was analysed by decomposing the spectra into two Gaussian components (labelled as peak 1, peak 2) as a function of excitation fluence, as shown in **Figure 5.3a-b**. The intensity (A), linewidth (w) and peak centre (λ) of these 2 peaks are extracted and plotted in **Figure 5.3c-d**. The ASE threshold (P_{th}) for both structures is indicated by the vertical line.

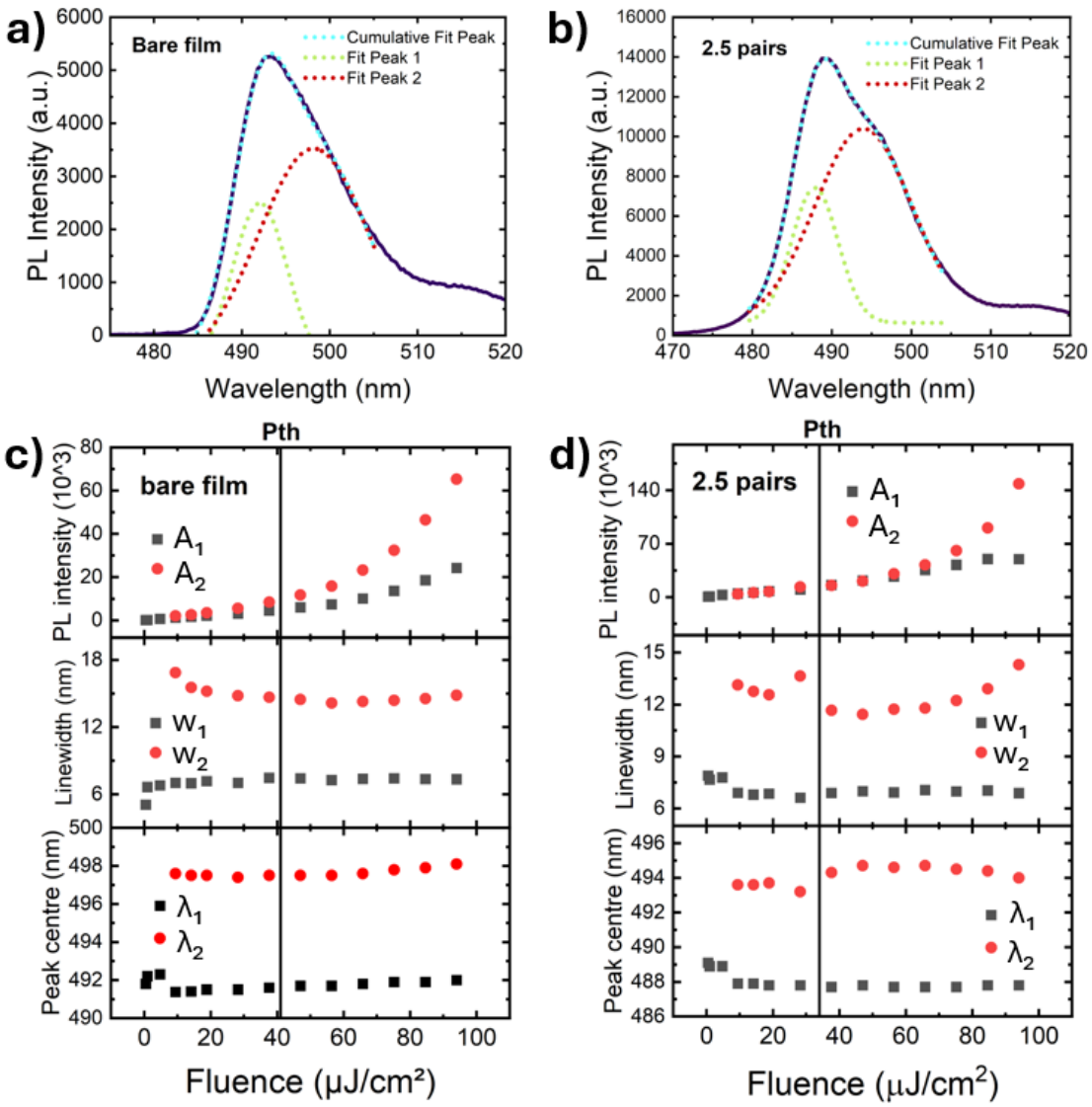

Figure 5.3 *Two-Gaussian fits of the main emission band (480–505 nm) of* ***a)*** *bare BA_2PbI_4 thin film* ***b)*** *2.5-pair BA_2PbI_4/PMMA bilayer under 94μJ/cm² pump. here, green dotted line is labelled as peak 1 and red dotted line is labelled as peak 2 ; Pump fluence-dependent spectral decomposition of ASE emission in* ***c)*** *bare BA_2PbI_4 thin film2.5-pair and* ***d)*** *BA_2PbI_4/PMMA bilayer and at 77 K. Integrated peak amplitudes (A_1, A_2), linewidths (w_1, w_2), and peak centres (λ_1, λ_2) are extracted from two-Gaussian fits. The vertical line marks the ASE threshold (P_{th}).*

In the bare BA_2PbI_4 film, the emission is dominated by a peak centred at ~ 492 nm (λ_1) at low excitation flux, which scales almost linearly with pump flux and exhibits only a weak linewidth evolution. This behaviour is characteristic of a spontaneous PL background that does not participate in stimulated amplification. Upon increasing the excitation density to around P_{th}, a second peak emerges at ~ 498 nm (λ_2), whose intensity increases superlinearly and is accompanied by a modest linewidth narrowing (~ 17 nm to ~ 14nm) across the ASE threshold (~ 41± 3 μJ/cm²). The combination of nonlinear intensity growth and spectral sharpening identifies Peak 2 (498 nm) as the ASE band in the bare film. In contrast, Peak 1 (492 nm) remains weakly dependent on fluence and does not display signatures of optical gain, confirming its assignment as excitonic PL.

As for the 2.5-pair BA_2PbI_4/PMMA bilayer waveguide structure, the peak 1 (centred at ~ 488 nm) is also present across the entire fluence range and increases only gradually with pump fluence, with a nearly constant linewidth of ~ 7 nm, consistent with spontaneous excitonic recombination. In contrast, the peak 2 (centred at ~ 494 nm) undergoes a pronounced superlinear increase in integrated intensity once the pump fluence exceeds P_{th}, which we identify as the onset of ASE. This transition is accompanied by a clear narrowing of the A_2 linewidth from ~ 14 nm to ~ 11nm at the threshold. It should be noted that at high excitation fluxes, the linewidth of A_2 broadens again, which might be attributed to local heat effects. Meanwhile, the ASE peak wavelength λ_2 remains relatively stable above threshold, indicating that amplification occurs at a well-defined region of the excitonic gain spectrum, whereas the spontaneous PL component λ_1 remains fixed at ~ 488 nm. The combined intensity nonlinearity, linewidth narrowing, and spectral stabilization of the A_2 component provide reasonable evidence that the 2.5-pair bilayer supports ASE emission originating from the lower-energy excitonic transition near 494 nm, with A_1 acting as a residual spontaneous emission background.

Notably, even this similar two-peak behaviour is observed in both structures, the peaks exhibit blue-shifted in the bilayer sample relative to the bare film, which is likely due to the modified dielectric environment and waveguided optical mode dispersion. Additionally, in both samples the ASE peak (Peak 2) is consistently red-shifted by ~ 6 nm (~ 30 meV) with respect to the excitonic PL (Peak 1). This behaviour indicates that stimulated emission originates from the lower-energy side of the exciton manifold where the net optical gain is maximised. The red-shifted ASE position might be attributed to reduced re-absorption losses and preferential population of relaxed, lower-energy exciton states, which together favour amplification at slightly lower photon energies.

Overall, although both the bare film and the 2.5-pair bilayer exhibit two emissive components, only the higher-wavelength band (Peak 2) displays the characteristic signatures of stimulated emission, which shows nonlinear intensity scaling and linewidth narrowing above threshold. This ASE band appears consistently on the red side of the excitonic PL maximum, reflecting preferential gain at lower photon energies where re-absorption losses are reduced and excitons relax into energetically favourable states prior to amplification. The bilayer structure exhibits a lower ASE threshold and stronger gain compared to the bare film, which we attribute to enhanced in-plane optical confinement and improved modal overlap arising from the BA_2PbI_4/PMMA waveguide geometry. These results suggest that the exciton reservoir in BA_2PbI_4 funnels population into a lower-energy emissive channel capable of supporting stimulated emission at cryogenic temperature.

In the following section, we investigate power-dependent PL in DBR-based cavity structures, where the same excitonic population dynamics is the foundation for bosonic final-state stimulation.

5.2.2. Power-Dependent Photoluminescence and Absence of Polariton Condensation

5.2.2.1. Mechanism of polariton condensation

Polariton condensation, also referred to as polariton lasing, occurs when a macroscopic population of polaritons occupies the ground state ($k = 0$) with identical momentum, energy, and phase once the excitation density exceeds a critical threshold. This leads to the spontaneous formation of a coherent light field without requiring population inversion, distinguishing it from conventional photon lasing and allowing a significantly lower threshold.

Under non-resonant excitation, most photogenerated carriers initially populate the high-energy exciton reservoir. Subsequent relaxation into the LPB and redistribution toward the $k = 0$ ground state enable the build-up of a coherent condensate. The relaxation dynamics governing this process are commonly described using a semiclassical kinetic model[22], which captures the interplay between scattering, stimulated processes, and losses. This approach provides a convenient framework for assessing the physical parameters that determine the condensation threshold, particularly the balance between exciton-polariton scattering, photon leakage, and polariton-polariton interactions.

The rate equation governing the temporal evolution of the polariton population $n_{pol}(t)$ at the LPB minimum can be written as:

$$\dot{n_{pol}} = -\Gamma_{pol} n_{pol} + W^{ex-pol} n_{ex} \left(1 + \frac{n_{pol}}{{n_{pol}}^{th}}\right) - \gamma' \left(n_{ex} + |X|^2 n_{pol}\right) |X|^2 n_{pol} \quad (5.1)$$

Where Γ_{pol} is the decay rate of polaritons which determined by the polariton lifetime and Q factor of the cavity and n_{pol} is the number of polaritons. W^{ex-pol} is population transfer rate from the exciton reservoir to the LPB, which governs efficient feeding of the polariton ground state, n_{ex} is

the population of excitons in the reservoir. The additional term with the ratio $\frac{n_{pol}}{{n_{pol}}^{th}}$ accounts for the bosonic stimulation of exciton scattering into the LPB. γ' represents the thermalization and polariton-polariton scattering losses, while $|X|^2$ is the Hopfield coefficient corresponding to the excitonic fraction of the polariton.

5.2.2.2. Low Temperature Power-dependent Photoluminescence

Following the demonstration of room-temperature strong coupling in Chapter 4 and the observation of ASE at low temperature (77K) in the previous section, we next investigate whether polariton condensation can be achieved in the BA_2PbI_4 microcavity system. Here, we examined two negatively detuned microcavities employing different DBR mirror configurations, namely 8 (top)/6 (bottom) and 8 (top)/12 (bottom) DBR cavities. These structures were intentionally designed with an increased number of DBR layers compared to the cavity discussed in Chapter 4, resulting in higher cavity quality (Q) factors and, in principle, stronger optical confinement. Such improvements in photon lifetime and mode confinement are expected to enhance light-matter interaction and increase the likelihood of reaching the polariton condensation regime.

Figure 5.4a and **5.4c** show the angle-resolved white-light reflectivity of these two microcavities at room temperature. For the 8/6 cavity, the UPB is located at 503 nm and the LPB at 536 nm at normal incidence, corresponding to a Rabi splitting of 282.4 meV. In contrast, the 8/12 cavity exhibits the UPB at 498 nm and the LPB at 532 nm, with a larger Rabi splitting of 351.8 meV, consistent with the increased photonic confinement provided by the thicker bottom DBR. In both cases, the experimental angle-resolved reflectivity maps show clear anticrossing behavior and are in good agreement with simulations based on the TMR model (**Figure 5.4a, c, left panels**), confirming that both cavities remain in the strong-coupling regime.

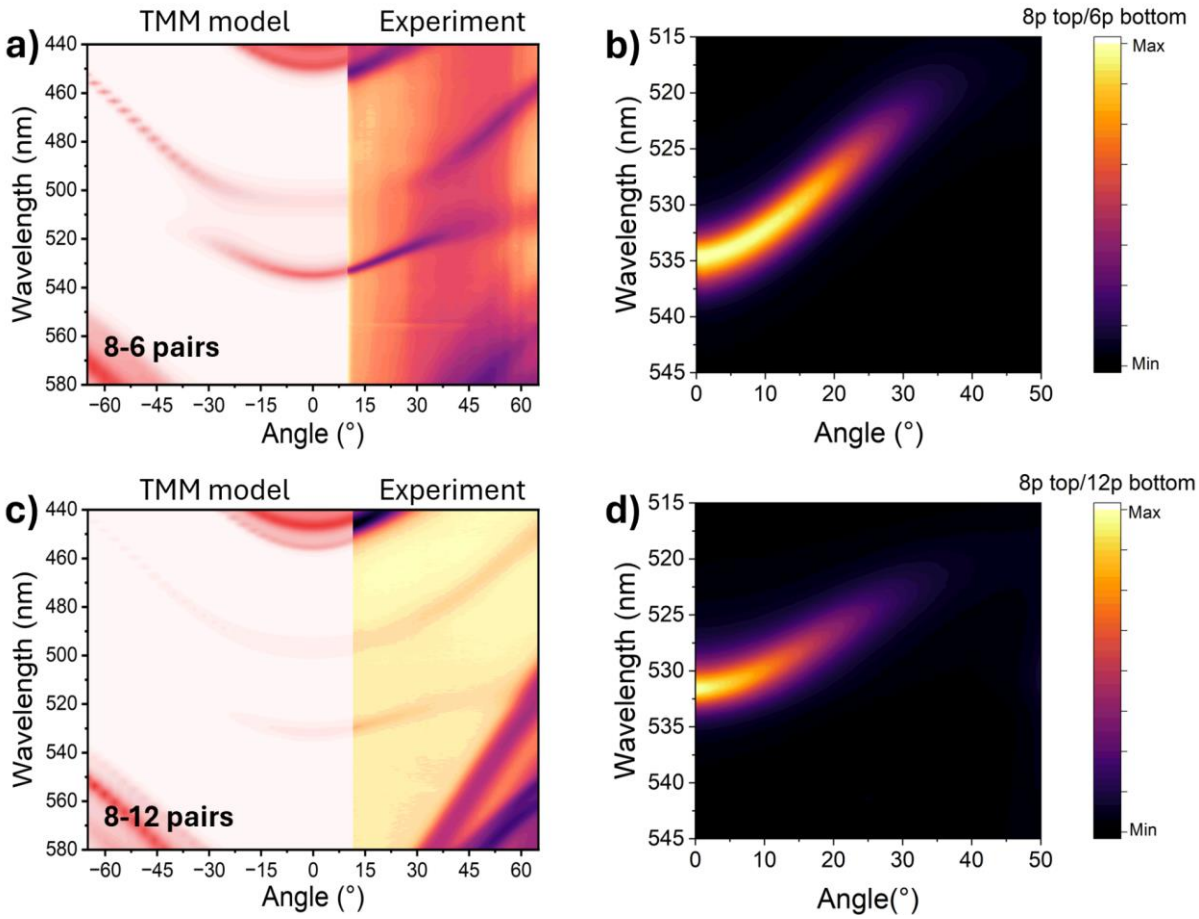

Figure 5.4 *Angle-resolved reflectivity and PL of* ***a-b)*** *8/6 and* ***c-d)*** *8/12 DBR cavities. For reflectivity spectra, the left panel are simulations from the TMR model, the right panel are the experimental data.*

Angle-resolved PL emissions under low-power continuous-wave (CW) excitation at 405 nm (~ 6.25 W/m²) are shown in **Figure 5.4b** for the 8/6 cavity and **Figure 5.4d** for the higher-Q 8/12 cavity. In both structures, the emission predominantly follows the dispersion of the LPB, with maximum intensity at or near normal incidence ($\theta \approx 0°$). Notably, no emission from the UPB is observed under these conditions. This suggests that UPB polaritons relax efficiently toward lower-energy states via scattering processes to the exciton reservoir and ultimately populating the LPB.

To quantify the cavity performance, the Q factors were extracted from the normal-incidence PL spectra. The emission peak at $\theta = 0°$ was fitted with a Lorentzian function to obtain the full width at half maximum (FWHM, $\Delta\lambda$), and the Q factor was calculated using $Q = \lambda/\Delta\lambda$. As shown in **Figure 5.5** and summarized in **Table 5.1**, the 8/6 cavity exhibits an emission centred at ~ 535 nm and a Q factor of approximately 162, whereas the LPB emission is at ~ 531 nm in 8/12 cavity which reaches a higher value of about 190. The increased Q factor in the latter cavity reflects enhanced optical confinement and reduced photon leakage resulting from the thicker bottom DBR mirror, consistent with the increased reflectivity expected for a larger number of DBR pairs.

To further assess the intrinsic photonic confinement supported by the cavity design, TMR simulations were performed without inclusion of the BA_2PbI_4 excitonic oscillator response. This approach isolates the purely photonic cavity linewidth from additional exciton-induced broadening and therefore provides an estimate of the ideal cavity performance determined primarily by the DBR structure. The simulated normal-incidence cavity resonances were analysed using the same Lorentzian fitting procedure, yielding Q-factors of ~ 480 and ~ 530 for the 8/6 and 8/12 cavities, respectively. These values are substantially larger than the experimentally measured LPB Q-factors.

The discrepancy between simulated and experimental Q-factors indicates that fabrication-related losses significantly reduce the effective photon lifetime in the real structures. In particular, surface roughness and thickness inhomogeneity in the spin-coated perovskite and PMMA layers can introduce additional scattering losses that are not captured in the idealized TMR model. Furthermore, absorption losses associated with trap states or defects within the perovskite layer can contribute to linewidth broadening and reduced cavity finesse. These non-idealities likely limit the achievable polariton lifetime and hinder efficient polariton relaxation toward the ground state, thereby suppressing the formation of a macroscopic condensate. This naturally motivates further

investigation using power-dependent photoluminescence measurements to determine whether polariton lasing or condensation can nevertheless be achieved in these cavity structures under higher excitation densities.

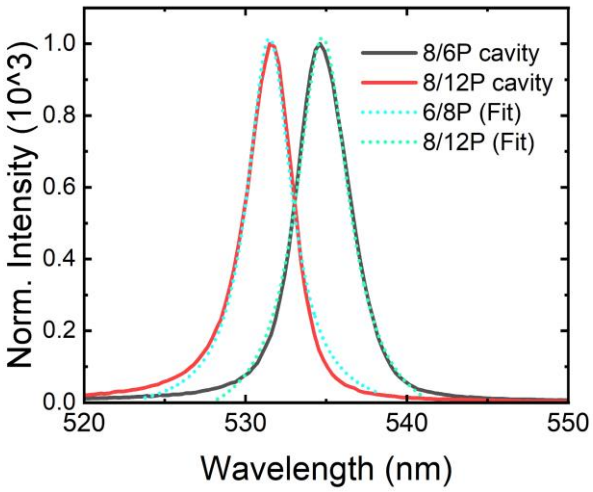

Figure 5.5 *Lorentz fit of emission of LPB at incident angle of 8/6 and 8/12 cavities*

	Peak centre (nm)	**FWHM (nm)**	**Q factor**	**Q factor (Sim.)**
8/6 cavity	534.75 ± 0.02	4.0 ± 0.08	~ 162	~ 480
8/12 cavity	531.48 ± 0.02	3.3 ± 0.09	~ 190	~ 530

Table 5.1 *Fitting parameters Lorentz fit of emission of LPB and Q factor of the cavities calculated from the fitting data and the simulation.*

To further assess whether these BA_2PbI_4 microcavities can support polariton condensation as described in Section 5.2.2.1, we performed power-dependent PL measurements under pulsed excitation at cryogenic temperatures. These experiments were done by the group in IBM Research Zurich and carried out at 4 K on the two negatively detuned microcavities shown above (8/6 and 8/12 cavity), using a 400 nm, 150 fs amplified laser pulse with a beam diameter of approximately

150 µm (FWHM). The choice of non-resonant excitation was intended to create a high-density exciton reservoir (n_{ex}), which, according to the kinetic model in **Eq. 5.1**, should feed the LPB via the exciton-polariton scattering rate W^{ex-pol}, potentially leading to bosonic stimulation once the polariton population approaches the threshold ${n_{pol}}^{th}$.

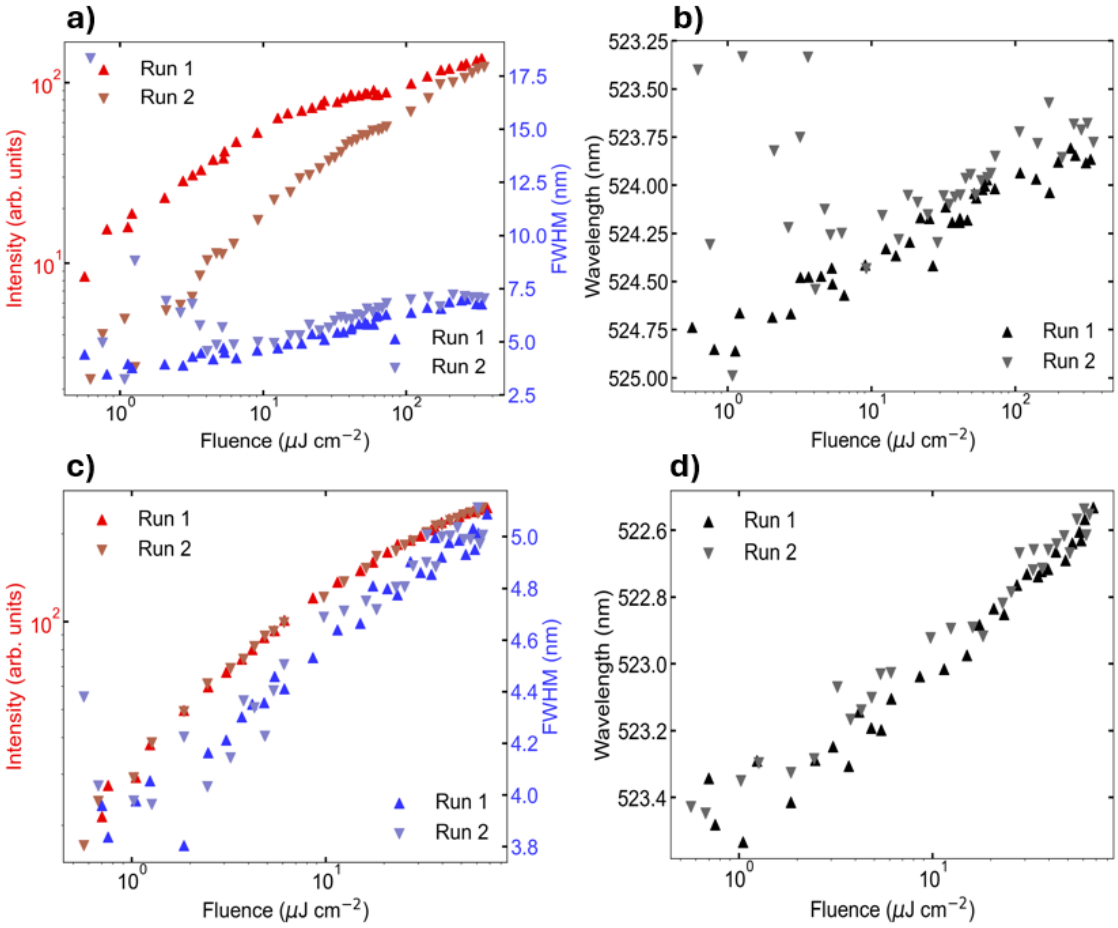

Figure 5.6 *Logscale fluence-dependent PL intensity, linewidth, and emission wavelength of* ***a-b)*** *8/6 and* ***c-d)****8/12 cavities at liquid-helium temperature*

Figure 5.6 (provided by the IBM group) presents the fluence-dependent integrated PL intensity, linewidth, and emission energy for both cavities at liquid-helium temperature. Over the entire

excitation range investigated, the integrated PL intensity increases approximately linearly with pump fluency for both the 8/6 and 8/12 cavities. Crucially, no threshold-like superlinear increase is observed in either structure. Furthermore, the LPB linewidth does not exhibit the characteristic narrowing expected from macroscopic occupation of the $k = 0$ state, and the emission energy shows only a modest blueshift of ~ 2 nm with increasing fluence. This small shift seems more consistent with exciton screening, phase-space filling, or thermal effects rather than polariton-polariton repulsion at a condensation threshold.

Within the framework of the rate equation introduced in Section 5.2.2.1, these observations indicate that the system does not reach the regime where the stimulated scattering term $(1+\frac{n_{pol}}{{n_{pol}}^{th}})$ dominates over losses. In other words, although non-resonant pumping successfully populates the exciton reservoir, the transfer rate $W^{ex-pol}\mathrm{n_{ex}}$ appears insufficient to overcome the polariton decay rate $\Gamma_{pol}n_{pol}$ and thermalization losses $\gamma'\mathrm{n_{ex}}$ required to trigger bosonic stimulation at the LPB minimum. As a result, the polariton population remains below the critical density needed for condensation.

The absence of condensation signatures must also be considered in light of the cavity Q factors. Although the 8/12 cavity exhibits a higher Q factor (≈190) than the 8/6 cavity (≈162), both values remain relatively modest compared to those typically reported for robust polariton condensation (up to a few hundred to thousand). A limited Q factor corresponds to a shorter polariton lifetime (higher Γ_{pol}), which reduces the probability of polaritons accumulating at $k = 0$ before radiative leakage occurs. In solution-processed perovskite microcavities, additional losses from surface roughness, structural disorder, and scattering further increase effective damping, making it even more difficult for the polariton population to reach ${n_{pol}}^{th}$.

5.3. Conclusion

The optical gain properties and nonlinear emission behavior of pure phase $n = 1$ BA_2PbI_4 were systematically investigated at low temperatures, both in bare thin films and in DBR-based microcavity structures. ASE measurements at 77 K revealed that BA_2PbI_4 can support optical gain, with a clear superlinear increase in emission intensity and linewidth narrowing above threshold. Spectral decomposition further identified the ASE as originating from a lower-energy emission band, consistent with gain formation following exciton relaxation and spectral red-shifting relative to spontaneous photoluminescence. These results establish BA_2PbI_4 as a viable low-temperature gain medium and provide an important benchmark for comparison with cavity-based polaritonic systems.

Building upon these findings, power-dependent PL measurements were performed on strongly coupled BA_2PbI_4 microcavities with increased DBR mirror pairs to enhance optical confinement. Despite clear evidence of strong exciton-photon coupling and well-defined lower polariton branches, no signatures of polariton condensation were observed under pulsed excitation at 4 K. The absence of polariton condensation, even in higher-Q cavities, indicates that the balance between polariton formation, relaxation, and loss remains unfavorable in the present system. While ASE demonstrates that population inversion and stimulated emission are achievable in BA_2PbI_4, the microcavity environment introduces additional constraints, including finite photon lifetimes, scattering losses, and incomplete relaxation from the exciton reservoir into the lower polariton ground state. These limitations likely prevent the accumulation of a macroscopic polariton population at $k = 0$, a prerequisite for condensation.

Overall, Chapter 5 highlights a critical distinction between conventional optical gain and polariton condensation in two-dimensional perovskite systems. Although BA_2PbI_4 exhibits strong excitonic

character, low-temperature gain, and robust strong coupling, the dynamical processes governing exciton relaxation and polariton feeding appear to limit the emergence of coherent polaritonic states. These results motivate a deeper investigation of ultrafast carrier and exciton dynamics, which is the focus of Chapter 6, where pump-probe spectroscopy is employed to elucidate the relaxation pathways, reservoir dynamics, and loss mechanisms that ultimately govern the feasibility of polariton condensation in $n = 1$ BA_2PbI_4 microcavities.

References

1 G. Xing, N. Mathews, S.S. Lim, N. Yantara, X. Liu, D. Sabba, M. Grätzel, S. Mhaisalkar, and T.C. Sum, "Low-temperature solution-processed wavelength-tunable perovskites for lasing," Nat Mater 13(5), 476–480 (2014).

2 K. Wang, S. Wang, S. Xiao, and Q. Song, "Recent Advances in Perovskite Micro- and Nanolasers," Advanced Optical Materials 6(18), 1800278 (2018).

3 J.R. Harwell, G.L. Whitworth, G.A. Turnbull, and I.D.W. Samuel, "Green Perovskite Distributed Feedback Lasers," Sci Rep 7(1), 11727 (2017).

4 P. Brenner, O. Bar-On, M. Jakoby, I. Allegro, B.S. Richards, U.W. Paetzold, I.A. Howard, J. Scheuer, and U. Lemmer, "Continuous wave amplified spontaneous emission in phase-stable lead halide perovskites," Nat Commun 10(1), 988 (2019).

5 C.M. Raghavan, T.-P. Chen, S.-S. Li, W.-L. Chen, C.-Y. Lo, Y.-M. Liao, G. Haider, C.-C. Lin, C.-C. Chen, R. Sankar, Y.-M. Chang, F.-C. Chou, and C.-W. Chen, "Low-Threshold Lasing from 2D Homologous Organic-Inorganic Hybrid Ruddlesden-Popper Perovskite Single Crystals," Nano Lett 18(5), 3221–3228 (2018).

6 M.R. Leyden, T. Matsushima, C. Qin, S. Ruan, H. Ye, and C. Adachi, "Amplified spontaneous emission in phenylethylammonium methylammonium lead iodide quasi-2D perovskites," Phys. Chem. Chem. Phys. 20(22), 15030–15036 (2018).

7 M. Cui, C. Qin, Y. Jiang, M. Yuan, L. Xu, D. Song, Y. Jiang, and Y. Liu, "Direct Observation of Competition between Amplified Spontaneous Emission and Auger Recombination in Quasi-Two-Dimensional Perovskites," J Phys Chem Lett 11(14), 5734–5740 (2020).

8 M. Li, Q. Gao, P. Liu, Q. Liao, H. Zhang, J. Yao, W. Hu, Y. Wu, and H. Fu, “Amplified Spontaneous Emission Based on 2D Ruddlesden–Popper Perovskites,” Advanced Functional Materials 28(17), 1707006 (2018).

9 H. Zhang, Q. Liao, Y. Wu, Z. Zhang, Q. Gao, P. Liu, M. Li, J. Yao, and H. Fu, “2D Ruddlesden-Popper Perovskites Microring Laser Array,” Adv Mater 30(15), e1706186 (2018).

10 M.L.D. Giorgi, A. Cretì, M.-G. La-Placa, P.P. Boix, H.J. Bolink, M. Lomascolo, and M. Anni, “Amplified spontaneous emission in thin films of quasi-2D BA3MA3Pb5Br16 lead halide perovskites,” Nanoscale 13(19), 8893–8900 (2021).

11 L. Gu, M. Li, J. Lai, D. Qian, K. Wen, L. Xu, G. Wang, S. Guan, Y. Zhang, X. Huang, J. Zhao, G. Xing, N. Wang, L. Zhu, Q. Peng, W. Huang, and J. Wang, “High Q-Factor and Low Threshold Continuous-Wave Near-Infrared Lasing with Quasi-2D Perovskites,” Advanced Functional Materials 33(44), 2303900 (2023).

12 M. Athanasiou, A. Manoli, P. Papagiorgis, K. Georgiou, Y. Berezovska, A. Othonos, M.I. Bodnarchuk, M.V. Kovalenko, and G. Itskos, “Flexible, Free-Standing Polymer Membranes Sensitized by CsPbX3 Nanocrystals as Gain Media for Low Threshold, Multicolor Light Amplification,” ACS Photonics 9(7), 2385–2397 (2022).

13 S. Ghosh, B. Pradhan, Y. Zhang, J. Hofkens, K.J. Karki, and A. Materny, “Nature of the different emissive states and strong exciton–phonon couplings in quasi-two-dimensional perovskites derived from phase-modulated two-photon micro-photoluminescence spectroscopy,” Phys. Chem. Chem. Phys. 23(6), 3983–3992 (2021).

14 M. Jamshidi, and J.M. Gardner, “Temperature-dependent excited states for detecting reversible phase transitions in 2D lead(II) iodide perovskites,” Dalton Trans. 53(25), 10544–10552 (2024).

15 Z. Yin, J. Leng, C. Zhao, J. Liu, B. Wu, and S. Jin, “Defect-Induced Inhomogeneous Phase Transition in 2D Perovskite Single Crystals at Low Temperatures,” ACS Omega 6(51), 35427–35432 (2021).

16 Z. Xiao, W. Meng, J. Wang, D.B. Mitzi, and Y. Yan, “Searching for promising new perovskite-based photovoltaic absorbers: the importance of electronic dimensionality,” Mater. Horiz. 4(2), 206–216 (2017).

17 T. Sheikh, A. Shinde, S. Mahamuni, and A. Nag, “Possible Dual Bandgap in (C4 H9 NH3)2 PbI4 2D Layered Perovskite: Single-Crystal and Exfoliated Few-Layer,” ACS Energy Lett. 3(12), 2940–2946 (2018).

18 Q. Zhang, Y. Ji, Z. Chen, D. Vella, X. Wang, Q.-H. Xu, Y. Li, and G. Eda, “Controlled Aqueous Synthesis of 2D Hybrid Perovskites with Bright Room-Temperature Long-Lived Luminescence,” J Phys Chem Lett 10(11), 2869–2873 (2019).

19 X. Wu, M.T. Trinh, D. Niesner, H. Zhu, Z. Norman, J.S. Owen, O. Yaffe, B.J. Kudisch, and X.-Y. Zhu, “Trap states in lead iodide perovskites,” J Am Chem Soc 137(5), 2089–2096 (2015).

20 S. Kahmann, E.K. Tekelenburg, H. Duim, M.E. Kamminga, and M.A. Loi, “Extrinsic nature of the broad photoluminescence in lead iodide-based Ruddlesden–Popper perovskites,” Nat Commun 11(1), 2344 (2020).

21 H. Duim, S. Adjokatse, S. Kahmann, G.H. ten Brink, and M.A. Loi, “The Impact of Stoichiometry on the Photophysical Properties of Ruddlesden–Popper Perovskites,” Advanced Functional Materials 30(5), 1907505 (2020).

22 L. Blackham, A. Manjalingal, S.R. Koshkaki, and A. Mandal, “Microscopic Theory of Polaron-Polariton Dispersion and Propagation,” Nano Lett 25(44), 15874–15882 (n.d.).

Chapter 6

Mapping Polariton Relaxation and Kinetic Bottlenecks to Condensation in 2D BA_2PbI_4 Microcavities

In this Chapter, we employed femtosecond transient absorption (TA) spectroscopy in BA_2PbI_4 microcavities to directly probe the underlying exciton–polariton relaxation dynamics. Global analysis of the TA spectra reveals three distinct characteristic timescales. The decay-associated spectra (DAS) further indicate that population transfer from the exciton reservoir to the LPB is limited, preventing significant polariton accumulation. These results provide a comprehensive ultrafast spectroscopic analysis and evidence of the relaxation bottlenecks governing two-dimensional perovskite polariton formation.

6.1. Introduction

In the last chapter, we have shown no condensation signal in BA_2PbI_4 microcavities even down to 4K. The difficulty arises largely from incomplete understanding of polariton relaxation dynamics, this includes how excitons scatter, thermalize, and populate the LPB. Nonradiative losses such as exciton-exciton annihilation (EEA), trap-assisted recombination, and exciton reservoir bottlenecks often dominate relaxation pathways, preventing sufficient accumulation of polaritons at the ground state.

Recent studies have begun to shed light on this complex picture. Liu *et al.* demonstrated that spin-dependent polariton-polariton interactions in 2D perovskite microcavities are highly sensitive to

detuning and polarization, revealing strong many-body exchange processes that shape polariton scattering.[1] Fieramosca *et al.* identified that dark-state reservoirs and Coulomb-mediated interactions dominate the nonlinear response, emphasizing the role of non-emissive states in polariton decay.[2] Similarly, the other work observed a pronounced polariton relaxation bottleneck, which could only be suppressed at temperatures below 60 K with the activation of dark exciton and biexciton channels.[3] Most recently, Fei *et al.* used ultrafast spectroscopy to demonstrate that strong light-matter coupling can suppress exciton-exciton annihilation by nearly an order of magnitude, as the photonic component of polaritons dilutes the exciton density and reduces scattering.[4] Together, these studies underline the complex interplay between bright polaritons, exciton reservoirs, and dark states, all of which govern energy relaxation and scattering in 2D perovskite systems. However, the ultrafast timescales and spectral overlap of these processes have made direct observation challenging.

In this chapter, we employ femtosecond transient absorption (TA) spectroscopy to directly probe exciton-polariton relaxation in BA_2PbI_4 microcavities - a system that exhibits clear strong coupling we have shown in Chapter 4 and 5 yet has not previously been explored using ultrafast spectroscopy. By employing a global lifetime analysis, we compare bare films and strongly coupled cavities with different detuning and identify distinct temporal regimes corresponding to carrier thermalization, exciton-polariton scattering, and long-lived dark-state dynamics. These results provide direct spectroscopic evidence for energy transfer from the exciton reservoir to the LPB and reveal the kinetic bottlenecks that hinder polariton condensation in 2D perovskite microcavities.

6.2. Results and Discussion

6.2.1 Detuned Strongly Coupled BA_2PbI_4 Microcavities

The 2D BA_2PbI_4 microcavities investigated in this chapter share the same fundamental architecture as those introduced in Chapter 4. Specifically, an n = 1 BA_2PbI_4 thin film, synthesized with 4 mg/mL 18-crown-6, is embedded between bottom (6-pair) and top (4-pair) DBRs consisting of alternating λ/4-thick SiO_2 and TiO_2 layers. This DBR configuration was chosen to provide sufficient optical confinement while maintaining enhanced transmission for pump-probe measurements. Here, we focus on experiments undertaken on two different cavities that were characterised by a different exciton-photon detuning. In the first cavity ($\boldsymbol{P_{cav}}$), the photon mode was tuned to be at a higher energy as compared to the exciton energy (positively detuned cavity) while in the second cavity, the photon mode was negatively detuned with respect to the exciton energy ($\boldsymbol{N_{cav}}$). In both structures, a poly(methyl methacrylate) (PMMA) layer, spin-coated on top of the perovskite, further stabilized the architecture and acted as a spacer layer to directly adjust cavity length. Indeed, by changing the thickness of this layer between 92 and 127 nm, we can directly modify the exciton-photon detuning as we demonstrate below.

Angle-resolved white-light reflectivity from the microcavity samples shown in **Figure 6.1a-b,** right panel, reveals clear anti-crossing behaviour between the cavity mode and the exciton resonance at room temperature, with the LPB wavelength at normal incidence being located at 521 nm (537 nm) in $\boldsymbol{P_{cav}}$ ($\boldsymbol{N_{cav}}$). We have described this reflectivity dispersion using a TMR model (see **Figure 6.1a-b,** left panel), with excellent agreement between model and measurement obtained.

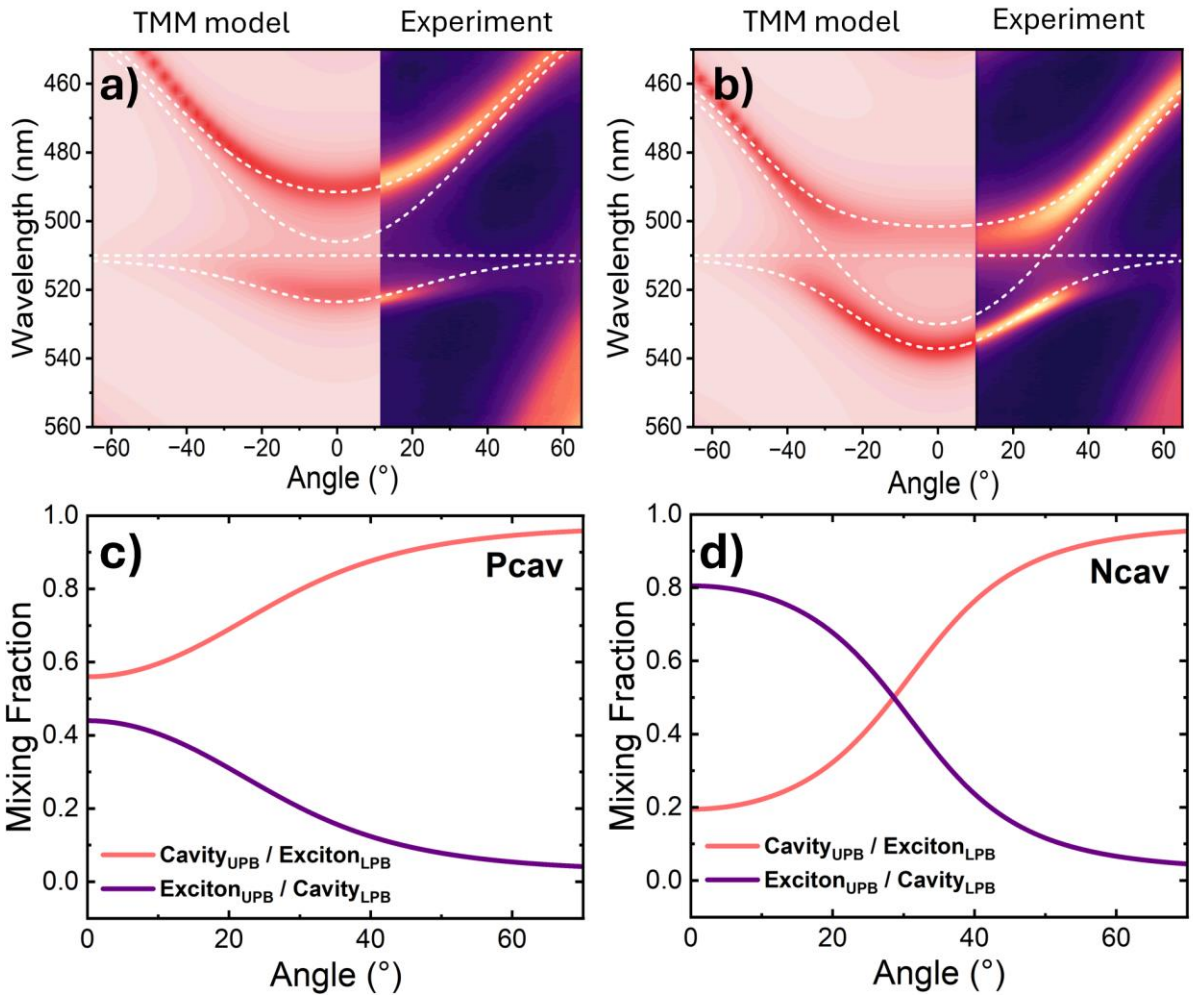

Figure 6.1 a-b) *simulation vs. experiment of angle-resolved reflectivity of* $\boldsymbol{P_{cav}}$ *and* $\boldsymbol{N_{cav}}$*, respectively. (The left panel is simulated by the TMR model, the right panel is the experimental data. Dash line overlapped with the colormap are the simulation of the energy of cavity photon, exciton, and UPB/LPB produced by coupled oscillator model.) Hopfield coefficient of* ***c)*** $\boldsymbol{P_{cav}}$ *and* ***d)*** $\boldsymbol{N_{cav}}$

We have also modelled exciton-photon hybridization in the microcavities using a two-level coupled oscillator Hamiltonian that is summarised in **Equation 6.1**. The model was used to fit the energy of the polariton modes as identified in the angular dependent reflectivity spectra of **Figure 6.1a, b** and is plotted using white dashed lines superimposed on the contour maps.

$$H = \begin{pmatrix} E_{cav}(\theta) & g \\ g & E_{ex}(\theta) \end{pmatrix} \begin{pmatrix} C\pm \\ X\pm \end{pmatrix} \quad (6.1)$$

Here, E_{cav} (θ) is the cavity photon dispersion as a function of angle θ, E_{ex} is the peak exciton energy, and g is the exciton-photon coupling constant. Note that in this material system, the change in the peak exciton energy E_{ex} as a function of angle is expected to be negligible if any, therefore we have used a fixed value of the peak absorption energy of the excitons of E_{ex} = 2.43eV for the range of angles modelled. C± and X± are the angle-dependent photon and exciton mixing coefficients, respectively, of the upper (+) and lower (–) polaritons. Diagonalization of this Hamiltonian yields the energy of the upper (UPB) and lower (LPB) polariton branches. We can quantify cavity detuning D using $D = E_{cav} - E_{ex}$, where E_{ex} is the fixed peak absorption energy of the excitons, and E_{cav} is the energy of the photon mode at normal incidence. From this, we calculate a detuning D for $\boldsymbol{P_{cav}}$ and $\boldsymbol{N_{cav}}$ giving the value of 20 and -100 meV respectively.

Using **Equation 6.1**, we can also calculate the polariton eigenvectors corresponding to the Hopfield coefficients which quantify the exciton and photon fractions of each polariton state:

$$|C(\theta)\pm|^2 = \frac{E_{cav}(\theta) - E(\theta)\pm}{E_{cav}(\theta) + E_{ex} - 2E(\theta)\pm} \quad (6.2)$$

$$|X(\theta)\pm|^2 = 1 - \frac{E_{cav}(\theta) - E(\theta)\pm}{E_{cav}(\theta) + E_{ex} - 2E(\theta)\pm} \quad (6.3)$$

with $|C(\theta)\pm|^2$ and $|X(\theta)\pm|^2$ being the photon and exciton weights as a function of angle, respectively. $E(\theta)\pm$ correspond to the energy of the UPB/LPB as a function of angle. These coefficients were computed as a function of incidence angle and indicate that in $\boldsymbol{P_{cav}}$ (see **Figure 6.1c**) the LPB is more exciton-like with a fraction of between 56% and 96% across all angles, while in $\boldsymbol{N_{cav}}$ (see **Figure 6.1d**), the LPB has a smaller exciton fraction (19% at normal incidence). The UPB of $\boldsymbol{P_{cav}}$ has a dominant photonic character, having a photon fraction between 56% and

96%. In contrast, the UPB of N_{cav}, is characterised by a greater excitonic weight compared to P_{cav} at normal incidence (81% compared to 44%). As we describe below, the difference between these two structures allows us to provide a microscopic explanation for the detuning-dependent relaxation pathways observed in their TA dynamics.

6.2.2 Transient Absorption and Global Fitting

To understand the processes that limit polariton relaxation and prevent polariton condensation, we have performed a detailed study on such structures using transient absorption spectroscopy, examining a range of time-windows, ranging from 1.3 ps before the arrival of the pump pulse to 500 ps after the pulse. Before describing the results of our study, however, we firstly outline the range of effects that can be expected following the photoexcitation of a semiconductor and their influence on a transient absorption spectrum. Here **Figure 6.3** plots a range of possible changes to the absorption-transition of a localised excitonic material; these include reduction in oscillator strength (photo-induced bleaching [PB]), spectral shifts (red- and blue-shifts) and spectral broadening. Here, excitonic bleaching (**Figure 6.3a**) results in the appearance of a peak in the normalised differential transmission (ΔT/T) spectrum, caused by the increased transparency of the film. Spectral shifts (see **Figure 6.3b-c**) similarly result in a new, positive ΔT/T peak, as a spectral region has been created in which optical transmission is increased. However, this is also accompanied by a negative feature caused by the fact that at some parts of the spectrum, optical transmission is reduced (photo-induced absorption [PA]). The relative order of the PB and PA features is determined by the direction in which the excitonic feature has moved. Finally, spectral broadening (see **Figure 6.3d**), results in both a central PB peak and two PA wings, caused as a result of additional induced absorption on either side of the main excitonic peak. In the samples

we discuss below, we show that a number of such effects can act together to create complex TA spectra.

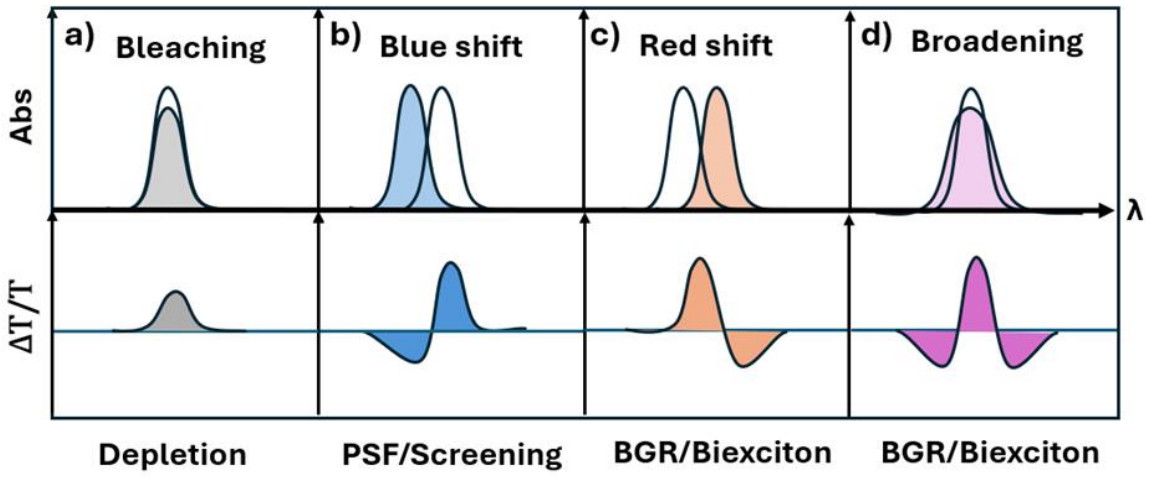

Figure 6.3. *Parts* ***a)*** *to* ***d)*** *indicate the general effects that are expected to contribute to a transient absorption spectrum.*

We note that there are a number of different excitonic processes that lead to the types of spectral changes illustrated in **Figure 6.3**. Photobleaching is observed when an electronic ground-state is depleted by an optical pump, with carriers promoted to a higher-lying state. Phase-space filling (PSF) originates from the Pauli exclusion principle; here states near the band edges ($k \approx 0$) become occupied by high density of hot photocarriers (see **Figure 6.4a**). This pushes optical transitions to higher energy (causing a blue shift) which reduces the possibility of forming excitons (reducing effective oscillator strength[5]). Spectral blue-shifts can also result from Coulomb screening. This occurs when there are many pump-induced free carriers which screen the Coulomb attraction between electrons and holes, thereby reducing the exciton binding energy (E_b)[6]. As the exciton energy (E_x) can be described using $E_x = E_g - E_b$ (where E_g is the electronic bandgap), a reduced E_b effectively pushes the apparent excitonic edge to higher energies. Red shifts can result from the

formation of biexciton states. These form when hot-excitons initially generated by the pump laser rapidly relax to the band-edge. Such cooled excitons then bind, forming a biexciton with the energy of this state being smaller than the neutral exciton energy by the biexciton binding energy[7]. Red-shifts and broadening effects can also result from band-gap renormalisation (BGR). Here, BGR can variously result from many-body interactions between photo-excited carriers that reduces the E_g together with exciton-phonon coupling (see **Figure 6.4b**).[6]

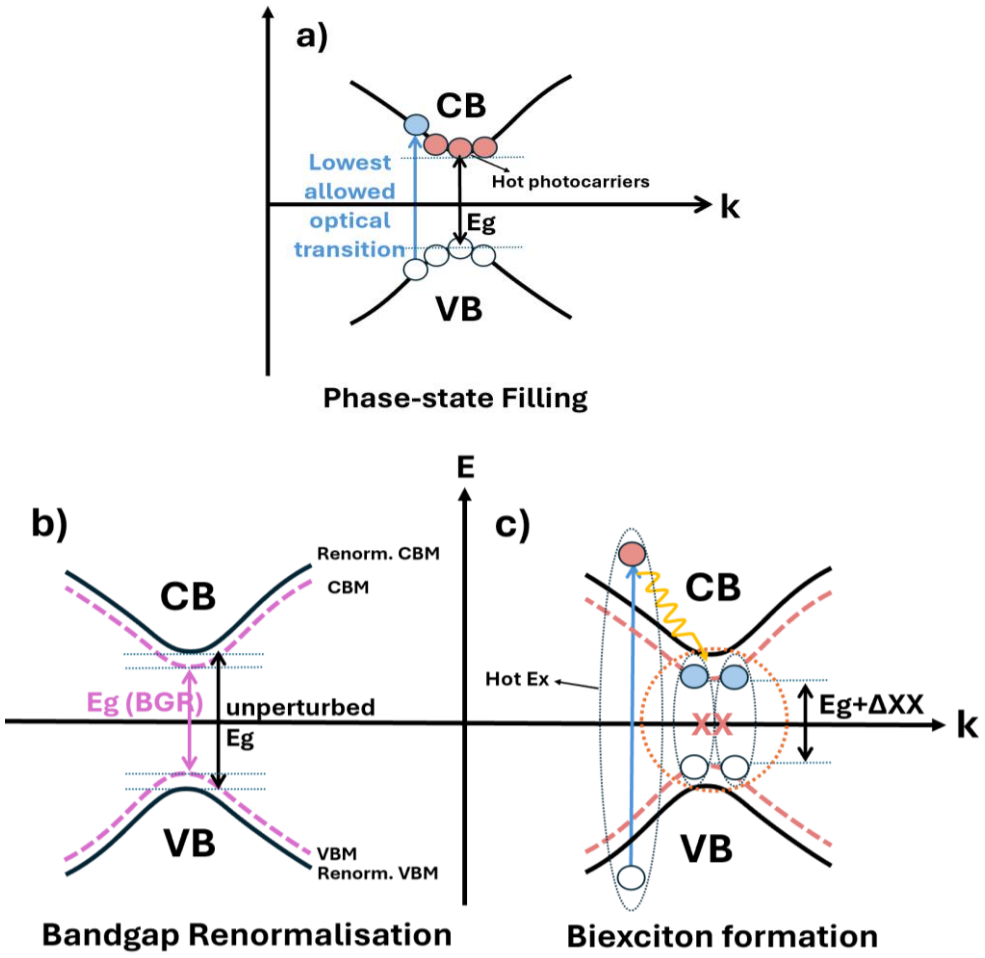

Figure 6.4 *Schematic process of* ***a)*** *phase-state filling (PSF),* ***b)*** *bandgap renormalisation (BGR), and* ***c)*** *biexciton formation (ΔXX < 0). Here, PSF causes blue-shift while BGR/biexciton induce red-shift where they both result in derivative-like features in the transient absorption spectrum.*

We now discuss the spectral response of thin films and cavities following optical pumping. Here, TA spectra were recorded following 400 nm non-resonant femtosecond excitation at two different pump fluences of 14 and 28 μJ cm^{-2}, with the pump beam incident at 5 degrees to the sample's normal (the pump-probe measurements were carried out at the University of Cyprus in collaboration with Dr. Emmanouil Lioudakis, Prof. Andreas Othonos, and Dr. Kyriacos Georgiou. See **3.2.7** in Chapter 3 for full details). This pump wavelength corresponds to a low reflectivity region of the DBR mirror and is thus able to non-resonantly excite perovskite excitons. A supercontinuum white-light probe (delayed in time) was then incident onto the cavity surface at normal incidence.

Figures 6.5a-c show representative ΔT/T spectra for the bare film and cavity samples at selected delays (top panels) along with their associated steady-state absorption spectra (bottom panels). In the control film (**Figure 6.5a**), a prominent PB feature appears near the exciton (510 nm) which is accompanied by derivative-like (negative) PA sidebands around 484 and 527 nm. The resulting derivative-like spectral lineshape resembles that observed in other ultrafast studies of 2D perovskite systems, but the origins of these spectral features are still under debate[8–11]. In both $\mathbf{P_{cav}}$ and $\mathbf{N_{cav}}$ (**Figures 6.5b and c** respectively), we observe two positive PB signals together with two negative derivative-like PA sidebands. However, the two PB features do not correspond to the wavelength of the polariton branches but are instead located in the spectral region between the polariton branches.

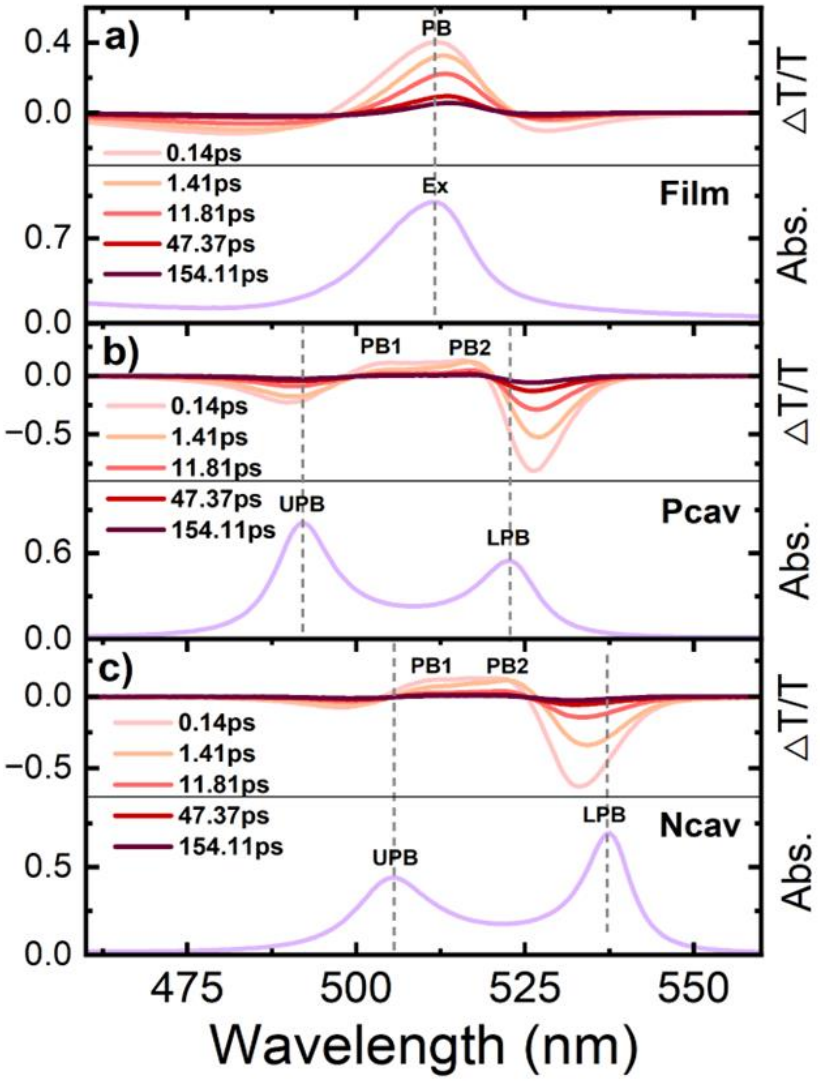

Figure 6.5. *Part* ***a)*** *shows a TA spectrum at different delay times recorded following excitation with a 28 μJ cm⁻² pump vs. steady-state absorption of the film. TA and steady-state absorption is shown in parts* ***b)*** *and* ***c)*** *for* $\mathbf{P_{cav}}$ *and* $\mathbf{N_{cav}}$ *respectively. Here, the steady-state film absorption has been experimentally measured while the absorption spectra of cavities are reproduced by our TMR model.*

To better understand the origin of the TA features and identify the factors that influence their energy and line shape, we calculate the linear optical transmission of a bare BA_2PbI_4 film at various pump–probe delay times [T(pump-on)] using

$$\frac{\Delta T}{T} = \frac{T_{pump\,on} - T_{pump\,off}}{T_{pump\,off}} \tag{6.4}$$

as shown in **Figure 6.6a**. Here, ΔT/T values were taken from the experimental data, with the amplitude of the steady-state transmission $T_{pump\,off}$ of the film being calculated using a TMR model based on the thickness of the sample layers used in the TA measurement. Note that the initial wavelength-dependent extinction coefficient parameters input into the TMR model are extracted from experimental transmission data of a bare BA_2PbI_4 film, with only the amplitude being adjusted by the model based on the film thickness. Here our calculated spectra indicates that on photoexcitation, the film exhibits an instantaneous blue-shift of 2 nm, moving from ~ 510 nm to ~ 508 nm (see spectra shown in **Figure 6.6b**), caused by a transient modification of the electronic band structure. This behaviour is primarily attributed to PSF and Coulomb screening. Following this, an energetic red-shift then occurs, with the excitonic transition relaxing from ~508 nm to ~509 nm as delay time increases, (see **Figure 6.6b**). We mainly attribute this effect to BGR[6,9,12].

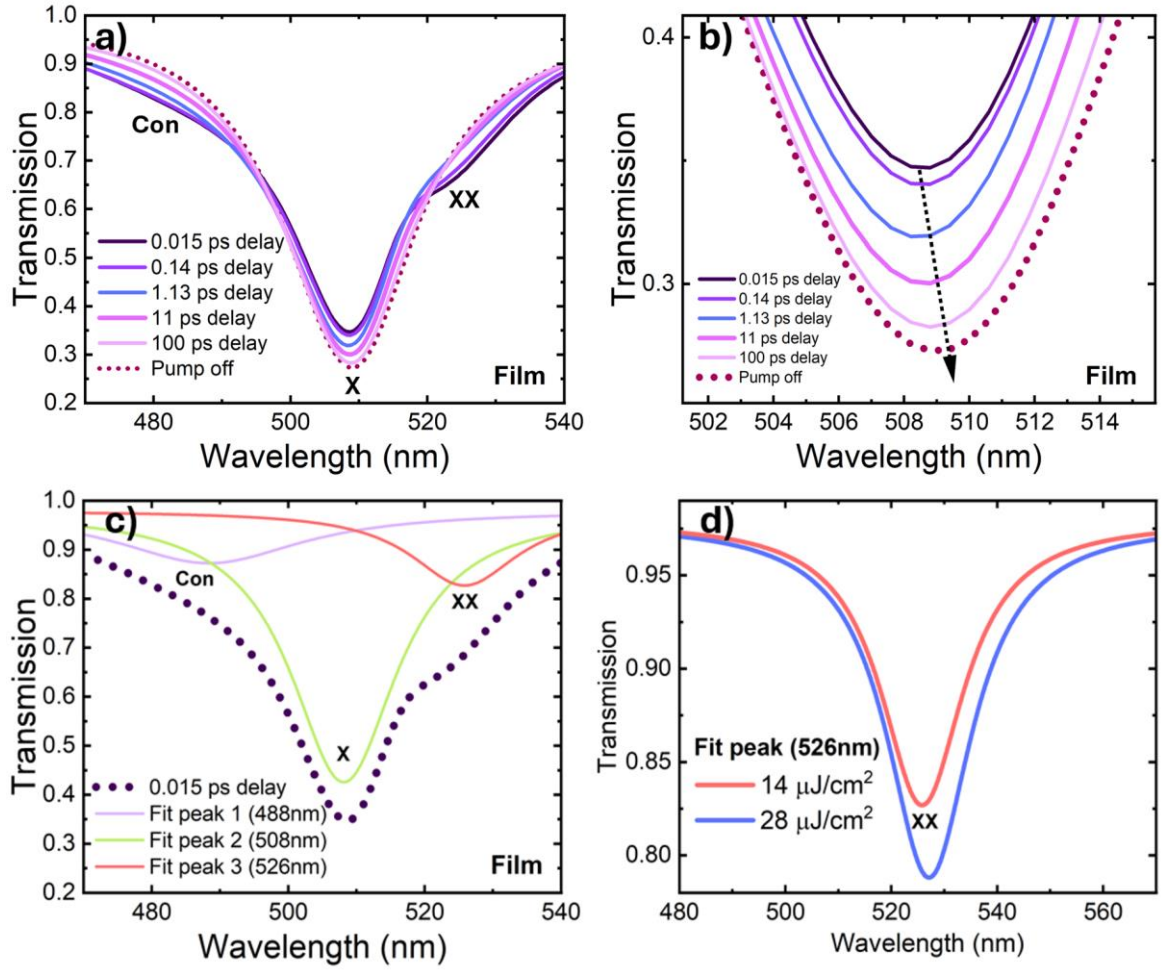

***Figure 6.6**. **a)** Transmission spectrum of the film without pump and following a 14 μJ cm⁻² pump at different time delays. The dotted line is the transmission when the pump is off (as predicted using a TMR model). The coloured solid lines correspond to the measured transmission at different time delays as indicated in the inset. **b)** zoom in on exciton energy change of part a, black dashed arrow indicates the blue-shift; **c)** shows the transmission spectrum following a 14 μJ cm⁻² pump at 0.015ps delay, with this fitted using 3 Lorentz peaks. Part **d)** shows transmission of the feature at 526 nm extracted from a fitting to the transmission data at 0.015ps delay. This fit is shown for a 14 μJ cm⁻² and a 28 μJ cm⁻² pump.*

Interestingly, we also find that a clear shoulder emerges at the low energy side of the main excitonic peak at early delay times (< 1ps). We fit the transmission spectrum at 0.015ps delay to three Lorentzian peaks at 488 nm, 508 nm, and 526 nm (see **Figure 6.6c**). Here, a band at higher energy of 488 nm having a linewidth of ~34 nm likely originates from optical transitions involving a continuum of unbound electron–hole pairs above the band edge (which we identify in the figure as "Con"). Apart from the exciton at 508 nm (marked "X"), we observe a shoulder at 526 nm which has previously been assigned to biexciton (marked "XX") formation[13]. We replot this fitted 526 nm peak at pump fluences of 14 and 28 μJ cm^{-2} in **Figure 6.6d**. Here, it is clear that the feature has a strong fluence dependence; an observation that supports its biexcitonic origin. As the delay time increases beyond around 1ps, the biexciton peak disappears and the transmission spectrum gradually recovers to its equilibrium shape; a result consistent with carrier cooling, exciton recombination, and lattice relaxation processes that restore the band structure over a time-scale of tens to hundreds of picoseconds.

We can use this TMR approach to model the TA spectra of both cavities, attempting to reproduce the line shape of the TA data. Again, we include known underlying processes active in perovskite films; PSF (included via blue-shifts and reduction in oscillator strength) and BGR (included via red-shifts and a broadening of excitonic transitions). The effect of these processes on a transient absorption spectrum is shown schematically in **Figure 6.3**. Here, it can be seen that both PSF and BGR result in the formation of a derivative line-shape due to their associated spectral-shift, while the broadening associated with BGR also introduces further PA features. We can use these basic ideas to examine the various processes that occur following photoexcitation of the control film and the cavity.

Figure 6.7a plots the differential transient transmission of $\mathbf{P_{cav}}$ at 11 ps following a 14 μJ cm^{-2} pump (dashed line). This delay time was chosen to minimize the biexciton and continuum band

contributions to the spectrum which are predominantly observed only at the fastest timescales. This approach is designed to simplify broadening and energy shift effects in the model. We first apply a model in which we simply bleach the exciton transition by 3% (oscillator strength reduction caused by PSF) shown using an orange solid line. Here we see a region of PB around the energy of the UPB and LPB, and two side-bands located at 486 and 528 nm. This simple model fails to adequately describe the measured data, as the strong bleaching predicted by the model around the UPB is not observed experimentally. We then explore a second model in which we apply a 0.5 nm blue-shift to the exciton, combined with a relative broadening of 8% as shown using the blue line in **Figure 6.7**. These values are obtained from the fitted data of the film transmission of pump-off and pump-on at 11ps delay, as shown in **Figure 6.7b**. We believe this blueshift and broadening are caused by the combined effects of PSF and BGR; here we note that at 11 ps, the exciton transmission is blue-shifted with respect to its steady-state value (see **Figure 6.6b**), although it is in fact red-shifted compared to its value at much earlier times. This suggests that a number of effects are probably important here, including PSF and BGR. It is clear however that this model alone again fails to fully predict the experiment, as it results in a strong PA at the UPB wavelength, with the wavelength of the LPB PB being relatively blue-shifted by 9 nm.

To provide a better description of the data, we can in fact combine the two models (bleaching, blueshift and broadening), with the prediction of the model shown using a dark solid line in the upper panel. Here the agreement between model and experiment is improved (although still not perfect); the model correctly predicts a small PA corresponding to the UPB and a broad PB around the exciton energy and the LPB. We believe that remaining discrepancies between this model and experiment likely arise from additional photoinduced changes in parameters such as refractive index, layer thicknesses, and DBR optical constants in the perovskite and surrounding organic layers, with all of these effects driven by thermal induced heating, which have been explored in the paper by Musser *et al.* [14]. However, our model indicates that photoinduced PSF and BGR

dominate the transient spectral reshaping not only in the bare non-cavity films but in the strongly coupled cavities as well.

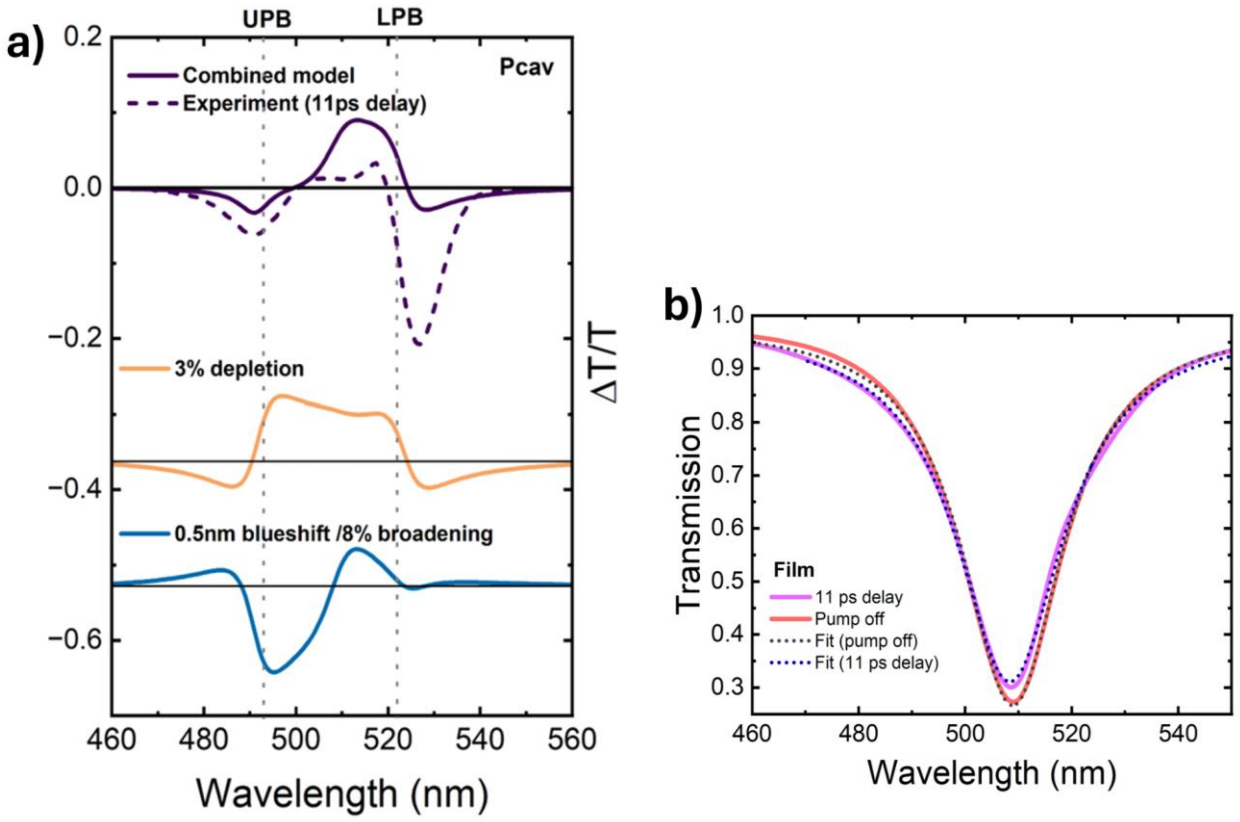

Figure 6.7. a) *Simulation vs. experimental TA spectrum of the* $\boldsymbol{P_{cav}}$ *under 14 μJ cm⁻² pump; solid line is TA spectrum at 11ps delay, dashed line is the simulation by TMR model. The orange solid line in the bottom panel shows TMR simulation with 3% exciton depletion, blue represents a net result of BGR and PSF which broadens and blueshifts the exciton energy. Here, the depletion represents the decrease of amplitude of the oscillator caused by PSF.* ***b)*** *Single-Lorentz fitting of the transmission spectrum of the film without pump and at 11ps time delay under 14 μJ/cm² pump. Dotted lines represent the fitting curves, while coloured solid lines are the experimental transmission data*

To further disentangle overlapping spectral contributions that influence the observed time-dependent features in the TA spectra, we performed a global lifetime analysis by simultaneously fitting the TA spectra across all wavelengths to a sum of exponentials convolved with the instrument response. Here, as shown in **Equation 6.5**, the TA data is fitted with a three-exponential decay function of the form:

$$I(t,\lambda) = A_1(\lambda) * \exp\left(-\frac{t}{t_1}\right) + A_2(\lambda) * \exp\left(-\frac{t}{t_2}\right) + A_3(\lambda) * \exp\left(-\frac{t}{t_3}\right) + I_0 \quad (6.5)$$

where $A_i(\lambda)$ are the wavelength-dependent amplitudes, t_i are the fitted lifetimes shared across all probe wavelengths, and I_0 accounts for a long-time offset or a drift in the baseline. This shared-lifetime strategy allows us to extract global timescales of the system while simultaneously producing amplitude spectra that indicate which spectral regions are dominated by each of the different processes. The amplitude spectra $A_i(\lambda)$ extracted for each lifetime can then be analysed to assign spectral features. For example, we can associate PB at the exciton or LPB positions with an increase in exciton or polariton populations, while red- and blue-shifted PA features indicate resonance reshaping induced by excitonic carrier populations. In this way, the global fitting decomposition can be used to directly link lifetime components to their corresponding spectral signatures in the TA data.

Using this approach, we can extract three characteristic lifetimes, t_1, t_2 and t_3, with each broadly associated with a distinct decay-associated spectrum (DAS). This is plotted in **Figure 6.8a-c**, where the amplitude of the three different lifetime components for the control film and cavities as a function of wavelength is shown for the two different pump fluxes (14 and 28 μJ cm^{-2}). This analytical approach has been widely used in previous pump-probe research to study organic and perovskite system dynamics[15–18] as it allows a more robust assignment of dynamical processes to be achieved compared to single-wavelength fits.

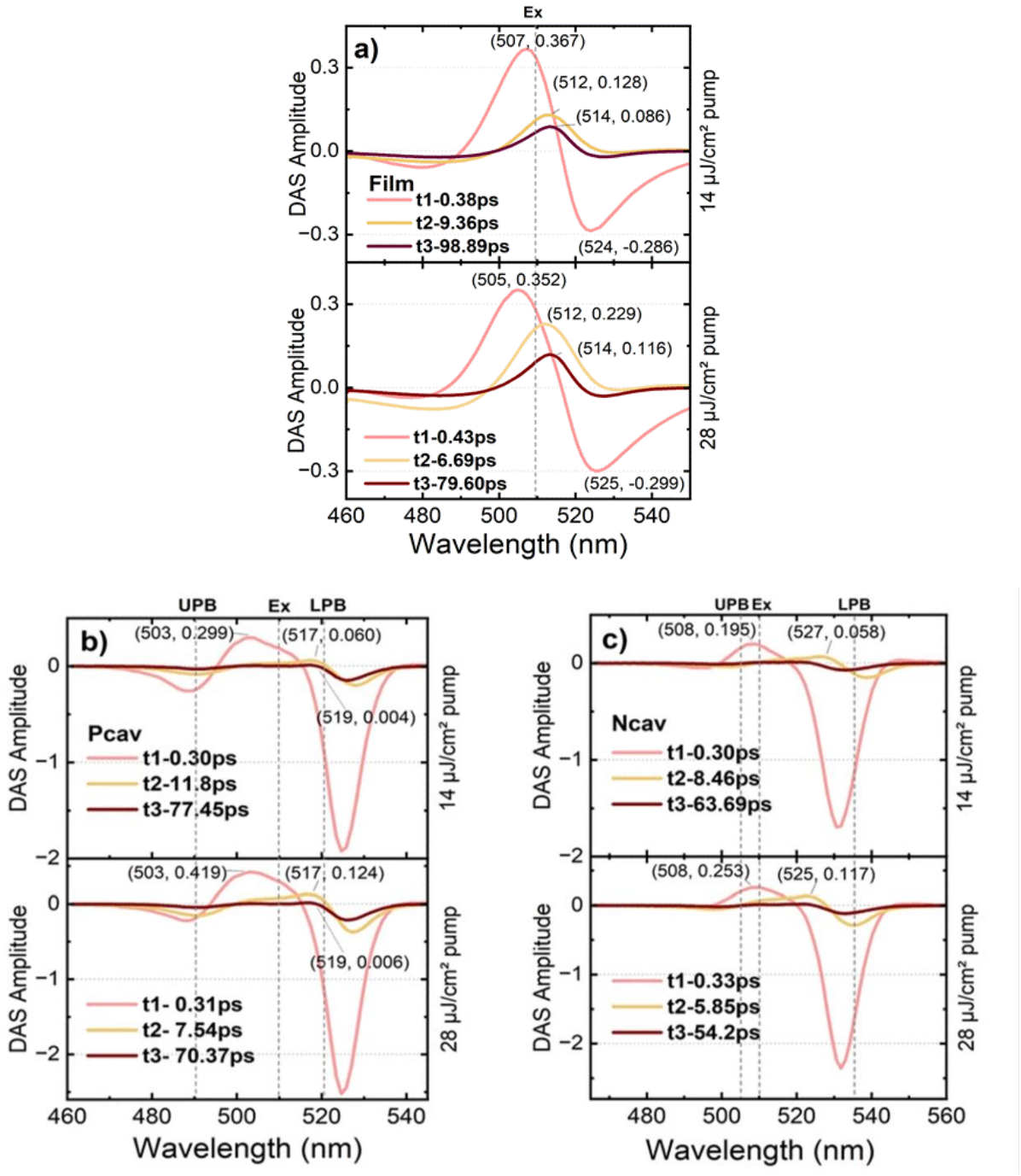

Figure 6.8. *Global fit of TA spectrum with the data presented recorded at two different pump fluxes: 14 and 28 µJ cm⁻². Data is shown for* ***a)*** *non-cavity film,* ***b)*** $\boldsymbol{P_{cav}}$ *and* ***c)*** $\boldsymbol{N_{cav}}$. *In all cases, the pink-line corresponds to the fastest decay dynamics having* t_1 *= 0.3 - 0.4 ps, orange corresponds to intermediate dynamics* t_2 *= 5 - 15 ps, with dark red representing the slowest dynamics* t_3 *= 60 - 100 ps. The vertical dashed lines correspond to the Ex, LPB and UPB wavelengths, respectively.*

6.2.2.1 Ultrafast time dynamics (t_1, 0.3 - 0.4 ps)

The pink trace in **Figure 6.8a** shows the DAS of the fastest component (t_1) in the non-cavity BA_2PbI_4 film, recorded at a pump flux of 14 and 28 μJ cm^{-2} respectively. At 14 μJ cm^{-2}, we observe a pronounced PB centred at ~507 nm, close to the 1s exciton resonance (~510 nm, marked as E_x with a vertical dashed line), accompanied by derivative-like PA sidebands at ~480 nm and ~525 nm. This spectral structure reflects several many-body processes that dominate immediately after photoexcitation. The strong PB arises primarily from PSF driven by hot-carrier thermalisation[8], which reduces the exciton oscillator strength and thereby increases transmission at the exciton wavelength. We speculate that the derivative-like PA sidebands result from a combination of PSF/Coulomb screening-induced blueshift (producing the feature centred at ~ 480 nm), with the feature at ~ 525 nm resulting from BGR and formation of biexcitons[19], as highlighted in **Figure 6.3**. At higher pump flux (28 μJ cm^{-2}), the derivative-like lineshape remains, however we find that the PB peak in the t_1 spectrum undergoes a 2 nm blue-shift to 505 nm compared to the same peak recorded at a lower pump flux. This effect is consistent with carrier-dependent PSF and Coulomb screening effects which drive a transient blue-shift at early times as discussed above.

Figures 6.8b and **6.8c** show the corresponding DAS of the t_1 component for $\mathbf{P_{cav}}$ and $\mathbf{N_{cav}}$ at both excitation fluences. In all cases, spectra are dominated by a broad PB signal located between the UPB and exciton, a weak high-energy PA at 485 - 495nm caused by PSF/ Screening, and a stronger low-energy PA band at 525 - 530 nm which mainly results from BGR and the significant population of biexcitons that are formed at ultrafast times as discussed above. For convenience, we mark the peak of the UPB, E_x and LPB wavelength as derived from steady-state reflection spectra using dashed lines. Here, the bleaching around the LPB energy is absent, which indicates that the LPB is not appreciably populated on ultrafast (< 1 ps) timescales. Instead, the t_1 response

is dominated by excitonic effects (PSF, screening, early-stage BGR, and biexciton interactions), which strongly reshape the exciton resonance and obscure polaritonic signatures. The broad PB observed in t_1 therefore reflects a transient renormalised exciton resonance, not a polariton bleach, as under nonresonant pumping, only the exciton reservoir is effectively populated on sub-picosecond timescales. As we discuss below, a LPB population appears only at later delays (t_2), consistent with picosecond-scale exciton-to-polariton scattering.

Importantly, the two cavities show different high-energy PA amplitudes. $\mathbf{P_{cav}}$ exhibits a pronounced blue-side PA at ~ 489 nm near the UPB wavelength, whereas this feature is nearly absent in $\mathbf{N_{cav}}$. This effect can be understood on the basis that the UPB in $\mathbf{N_{cav}}$ has a larger excitonic Hopfield fraction than does $\mathbf{P_{cav}}$ (56% vs. 19%). For this reason, we might expect that exciton-like UPB in $\mathbf{N_{cav}}$ to behave rather like an uncoupled exciton, undergoing a relatively large pump-induced exciton resonance reshaping, which results in a broader, more strongly damped optical mode that responds weakly to small excitonic perturbation. In other words, while the excitonic peak of the material itself experiences strong reshaping (PSF, screening, broadening), this reshaping does not efficiently modulate the UPB when the mode is strongly exciton-like and heavily broadened. In contrast, the energy of the more photon-like UPB in $\mathbf{P_{cav}}$ is likely to be strongly affected by exciton-induced dielectric changes in cavity refractive index, thermal heating etc., and will undergo a larger modulation of the UPB region in the TA spectrum. This highlights how the relative detuning not only governs polariton-branch population dynamics but also determines the visibility of spectral reshaping in transient absorption in the early-time regime. Using a TMM model, we have simulated the transmission spectra of a series of cavities with different detunings resulting in polaritons with different photon-exciton mixing. By inducing a fixed excitonic perturbation in all detunings, we have simulated the associated TA spectra, showing that the blue-side PA exhibits a non-monotonic dependence on the UPB photon fraction, peaking at intermediate mixing and diminishing for strongly exciton-like UPB states. This

indicates that the PA visibility is determined by an interplay between exciton-induced perturbations and the optical sensitivity of the cavity mode. Further details about our model are discussed in **Section 2** of the **SI** below.

6.2.2.2 Intermediate time dynamics (t_2, 5 - 15 ps)

The second kinetic component (t_2), shown as the orange trace in **Figure 6.8**, reveals pronounced differences between the bare BA_2PbI_4 film and the strongly coupled microcavities. In the control film (**Figure 6.8a**), the DAS of t_2 peaks at 512 nm, close to the steady-state exciton absorption at 510 nm. This feature reflects exciton-exciton interactions, primarily BGR and exciton-exciton annihilation (EEA). The fluence dependence of the t_2 amplitude provides clear evidence for this; at higher excitation densities, the bleach amplitude increases while the lifetime shortens (**Figure 6.8a,** bottom panel). This conclusion is consistent with EEA-induced depletion of exciton population and accelerated recombination dynamics.

In the strongly coupled cavities, however, the maximum of the t_2 DAS amplitude is red-shifted relative to the film, appearing at 517 nm for $\boldsymbol{P_{cav}}$ and 527 nm for $\boldsymbol{N_{cav}}$ (**Figures 6.8b, c** respectively). These wavelengths approximately coincide with the LPB resonances, although the PB of the LPB is relatively blue-shifted due (as we propose) to the carrier-induced PSF and BGR. This spectral evolution indicates that, on the picosecond timescale, exciton-to-polariton scattering becomes active, transferring population from the exciton reservoir into the LPB. However, because the scattering occurs over only several picoseconds (comparable to or slower than the polariton lifetime), this process produces a relaxation bottleneck, limiting efficient population build-up at the LPB minimum, which we believe likely impedes polariton condensation. A modest but measurable fluence-dependent enhancement in the t_2 bleaching amplitude is observed (from 0.06

to 0.124 in $\boldsymbol{P_{cav}}$ and from 0.058 to 0.117 in $\boldsymbol{N_{cav}}$) along with a corresponding lifetime shortening, further confirm that EEA remains operative even under strong coupling. Notably, the $\boldsymbol{P_{cav}}$, with its more exciton-like LPB, exhibits a slightly stronger t_2 bleach than the more photon-like $\boldsymbol{N_{cav}}$, particularly at higher excitation flux. This behaviour is consistent with previous reports showing that increasing the photonic fraction of a polariton mode dilutes its excitonic density, thereby reducing the strength of exciton-exciton interactions[19].

It is also worth noting that the smaller bleach amplitude of t_2 compared to t_1 at LPB implies there is a limited population accumulation which might result from reverse scattering from LPB back into the exciton reservoir; a process that has previously been reported in strong-coupled organic polariton systems.[20] Collectively, these observations confirm that while exciton–to–polariton transfer occurs efficiently on picosecond timescales, bimolecular annihilation and bottleneck-limited relaxation dominate the intermediate dynamics; these effects likely suppress the effective population of the lower polariton state which consequently prevents condensation.

6.2.2.3 Long-lived time dynamics (t_3, 60 - 100 ps)

The final decay component, t_3, dominates the late-time dynamics and is plotted in dark red in **Figure 6.8**. In the non-cavity control-film (**Figure 6.8a**), t_3 appears as a weak bleach slightly red-shifted from the main exciton resonance (514 nm), consistent with the formation of lower energy long-lived dark or trap-associated exciton states. In contrast, in both $\boldsymbol{P_{cav}}$ and $\boldsymbol{N_{cav}}$ (**Figures 6.8b and 6.8c**), no distinct bleach is observed at either the exciton or polariton energies. Instead, a weak PA feature emerges near the LPB region at 525 - 530 nm, suggesting that the residual population at long delays primarily resides in dark or localized excitonic states that couple only weakly to the cavity field.

The absence of any photobleaching recovery at the LPB wavelength confirms that the long-lived population does not efficiently feed back into the bright polariton modes. Instead, the weak red-side PA observed in t_3 is consistent with nonradiative relaxation of excitons that have become localized through trapping states. Such localized excitons relax via phonon-assisted transitions from these bound states into higher vibronic manifolds, giving rise to a broad, low-energy absorption tail. Importantly, the low-energy PA feature in t_3 is blue-shifted relative to the corresponding PA in t_2. This shift reflects the disappearance of the BGR-induced redshift present at earlier times, indicating that the carrier density has decayed and that significant reservoir-to-polariton feeding is unlikely. Together, these observations show that t_3 primarily corresponds to dark or trap-mediated exciton decay, rather than any residual population of polariton states.

It is clear that there is a noticeable and general spectral blueshift of the t_1 trace compared to t_2 and t_3 that is evident in both the film and cavities. This originates from rapid PSF and Coulomb screening effects that occur immediately after photoexcitation as discussed earlier. High carrier densities partially occupy the band-edge states, reducing the exciton binding energy and thereby shifting the exciton resonance to higher energies, causing the observed blue-shift. This blueshift may also be enhanced by a non-resonant photoexcitation-induced optical Stark effect (OSE)[10]. As the carriers cool and PSF weakens, BGR becomes dominant, lowering the bandgap and shifting the exciton resonance to longer wavelengths causing a red-shift, as reflected by the t_2 and t_3 bleaching features.

6.3. Discussion

We expect the efficiency of population transfer from the exciton reservoir to the LPB to be highly sensitive to the energetic overlap between the reservoir emission and the LPB minimum. When

these are resonant, relaxation can proceed efficiently via emission-reabsorption processes, allowing polaritons to accumulate at the bottom of the dispersion.[21] We suspect however in the negatively detuned cavity studied, there is a *polariton relaxation bottleneck* that results in inefficient exciton-to-polariton scattering, preventing the effective establishment of a large polariton population at the LPB minimum. Such bottleneck behaviour is fully consistent with the TA dynamics discussed above. In both $\boldsymbol{P_{cav}}$ and $\boldsymbol{N_{cav}}$, the t_2 component revealed incomplete exciton-to-polariton transfer within a ~10 ps timescale and a lack of sustained LPB population at longer time delays. Furthermore, the t_3 component indicated exciton trapping in dark states. Taken together, these results confirm that limited scattering efficiency, short polariton lifetimes, and strong nonradiative losses collectively prohibit the system from reaching the critical density required for polariton condensation under the conditions investigated.

It is interesting to note that the negative derivative-like PA sidebands observed in all three decay components originate from different microscopic mechanisms at each timescale. In the ultrafast regime (< 1ps), the PA arises primarily from exciton phase-space filling, hot-carrier screening, and biexciton formation, which transiently reshape and blue-shift the exciton resonance. During the intermediate t_2 dynamics, the PA is dominated by LPB reshaping, where exciton-to-polariton scattering, BGR, and carrier-induced broadening jointly distort the LPB and exciton lineshape. At late times (t_3), the remaining PA feature originates mainly from trap-assisted or dark-state absorption, reflecting long-lived, nonradiative exciton populations that weakly perturb the optical response. The evolution of these PA signatures thus captures the system's transition from coherent exciton-polariton dynamics at early delays to incoherent and defect-mediated relaxation as the system approaches equilibrium.

6.4. Conclusion

This work presents a comprehensive investigation of the ultrafast relaxation dynamics in strongly coupled 2D BA_2PbI_4 microcavities using femtosecond transient absorption spectroscopy. Global fitting analysis revealed a three-step relaxation sequence consisting of ultrafast carrier thermalization and exciton/biexciton formation (t_1), exciton-to-polariton scattering and exciton-exciton annihilation (t_2), and long-lived dark or trap-state relaxation (t_3). A detailed spectral analysis indicates how these processes evolve under strong coupling and different detuning conditions.

Compared with the bare film, the microcavities exhibit a red-shift of the t_2 bleaching feature from the exciton energy toward the lower polariton branch, signifying exciton-to-polariton transfer on picosecond timescales. However, the absence of a sustained polariton bleach at late times indicates that the remaining population becomes trapped in optically inactive states, preventing efficient radiative recombination. These findings show that under non-resonant excitation, rapid energy relaxation, bimolecular annihilation, and trap-assisted losses compete with polariton build-up, leading to a kinetic relaxation bottleneck that hinders polariton condensation.

Overall, this study provides direct ultrafast spectroscopic insight into the relaxation pathways in BA_2PbI_4 microcavities and highlights several factors, such as exciton–photon detuning, cavity losses, and the efficiency of exciton-to-polariton transfer that likely influence polariton build-up under non-resonant excitation. These observations offer guidance for future optimization strategies aimed at improving polariton relaxation and potentially enabling the so-far elusive room-temperature condensation in 2D perovskite systems.

Supporting Information

S1. Global fitting

To quantitatively analyse the ultrafast dynamics, global fitting was applied to the transient absorption (TA) spectra over the probe wavelength range of 460 - 560 nm. Instead of fitting each probe wavelength independently, global analysis assumes that the relaxation dynamics are governed by a common set of characteristic timescales, while the relative spectral contributions of these timescales vary with wavelength. This approach reduces fitting ambiguity, improves robustness, and enables clearer assignment of spectral features to specific dynamical processes. The TA data fit with a three-exponential decay function of the form which has been shown in Eq. 6.5.

Figure S1 shows the global fitting of kinetics spectrum (ΔT/T vs. delay times) of film and cavities under 28 μJ/cm^2 pump. The coloured dots are experimental data and the coloured lines are our fitting data. The R^2 for all fittings is > 0.999, which evidences that the fittings are accurate enough to predict the decay kinetics.

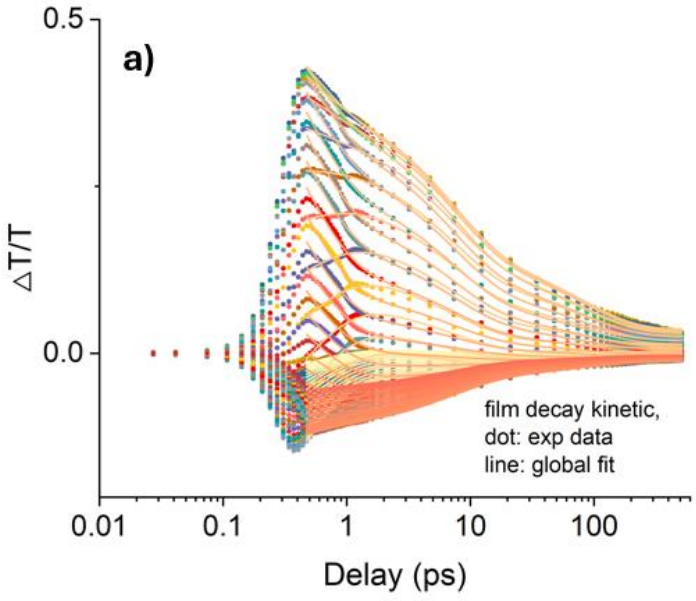

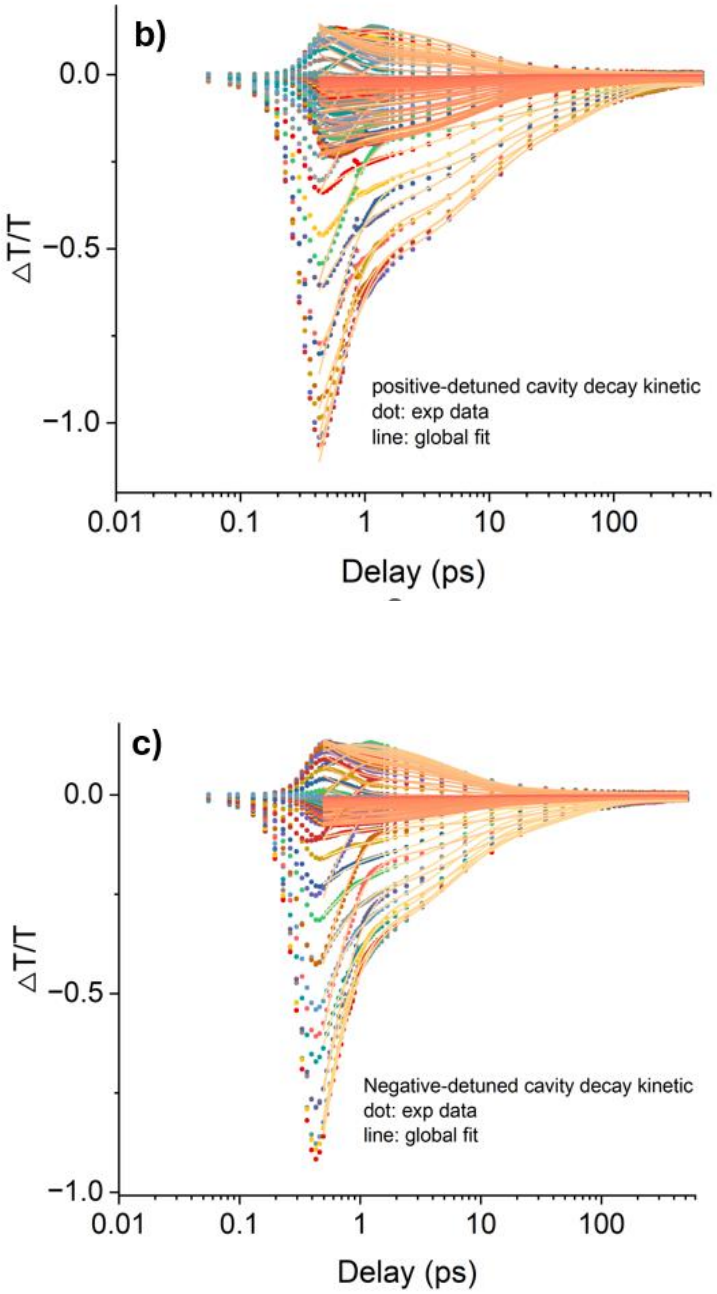

Figure S1. *Decay kinetics of all the wavelengths and their global fitting spectrum of the* ***a)*** *bare film and* ***b)*** *positive- and* ***c)*** *negative- detuned cavities under 28 μJ/cm^2 pump, respectively (here, for all the fittings, overall $R^2 > 0.999$).*

The exponential components can also be interpreted in the framework of semiconductor recombination kinetics as we discussed in Chapter 2, where the carrier density n(t) evolves according to:

$$\frac{dn}{dt} = -k_1 n - k_2 n^2 - k_3 n^3 \qquad (S2)$$

with k_1, k_2, and k_3 corresponding to the monomolecular (e.g. exciton/polariton, trap-assisted), bimolecular (e.g. exciton–exciton annihilation), and three-body (e.g. Auger) recombination coefficients, respectively.

The characteristic timescales for these processes can be approximated by: $t_1 \sim \frac{1}{k_1}, t_2 \sim \frac{1}{k_2 n_0}, t_3 \sim \frac{1}{k_3 {n_0}^2}$, where n_0 is the initial carrier density determined by the pump fluence. This relationship highlights why higher pump fluences lead to shorter apparent lifetimes for t_2 and t_3 components, as stronger exciton–exciton and Auger interactions accelerate decay. Note that this equation does not take the process of hot carrier thermalization into account while this can be seen in the exponential equation (see **eq. S1**).

Thus, the global fitting approach not only separates the experimental signal into distinct lifetimes and spectral features but also provides a framework for linking these lifetimes to underlying recombination processes. In the context of strongly coupled microcavities, t_1 corresponds to ultrafast exciton thermalization and cavity-induced reshaping, t_2 reflects exciton–polariton transfer and EEA, and t_3 represents non-radiative trapping in long-lived dark states.

S2. Effect of photon fraction of UPB for high-energy PA

To further rationalize the enhanced blue-side PA observed in the $\boldsymbol{P_{cav}}$, we performed TMR simulations in which the excitonic perturbation was kept fixed (3% oscillator-strength depletion combined with a 0.5 nm exciton blueshift and 8% broadening), while the cavity detuning and the photon-exciton mixing of the polariton branches were tuned by varying the PMMA spacer thickness. **Figure S2a** shows the corresponding simulated pump-off transmission spectra for PMMA thicknesses ranging from 90 to 130 nm, where both polariton branches shift systematically to longer wavelengths (UPB: 490 to 502 nm; LPB: 524 to 540 nm). Importantly, increasing the PMMA thickness shifts the cavity mode and thus decreases the photonic fraction of the UPB extracted from the coupled-oscillator model (see **Figure S2b**), from 62% to 18%, leading to pronounced changes in the simulated transient absorption lineshape.

The simulated ΔT/T spectra (see **Figure S2c**) reveal a non-monotonic dependence of the blue-side PA amplitude on photon fraction, with a maximum occurring at intermediate mixing (~ 35%), and a pronounced suppression for strongly exciton-like UPB states (< 25% photon fraction). This behaviour indicates that the observed PA amplitude is governed by the competition between i) the strength of the exciton-induced dielectric perturbation, which grows with excitonic character, and ii) the optical sensitivity of the cavity mode, which is enhanced for photon-like, spectrally sharp resonances. This blue-side PA amplitude (A) thus can be quantitatively described as analogous to the product: weighted exciton-induced dielectric perturbation $|X|^2\Delta\varepsilon$ × cavity sensitivity $|C|^2$. As a result, the PA is maximised at intermediate UPB mixing, where exciton-driven Δε effects remain strong while the cavity mode retains sufficient photonic character to efficiently transduce these perturbations into ΔT/T. In the experimental structures, the UPB in the $\boldsymbol{P_{cav}}$ has a photon fraction of 56%, placing it within the high-sensitivity regime where exciton-induced refractive index changes are efficiently transduced into a strong dispersive PA signal. In contrast, the UPB in the $\boldsymbol{N_{cav}}$ has a much lower photon fraction (19%), where the cavity mode becomes broader and less sensitive to refractive index modulation, leading to a strongly reduced PA amplitude. Importantly,

this behaviour arises without invoking UPB population, instead, the UPB acts as a sensitive optical probe of ultrafast exciton-induced dielectric reshaping. This reflects that the visibility of the blue-side PA is governed by the interplay between excitonic perturbations and cavity-mode sensitivity, and directly provides quantitative support for what is observed experimentally.

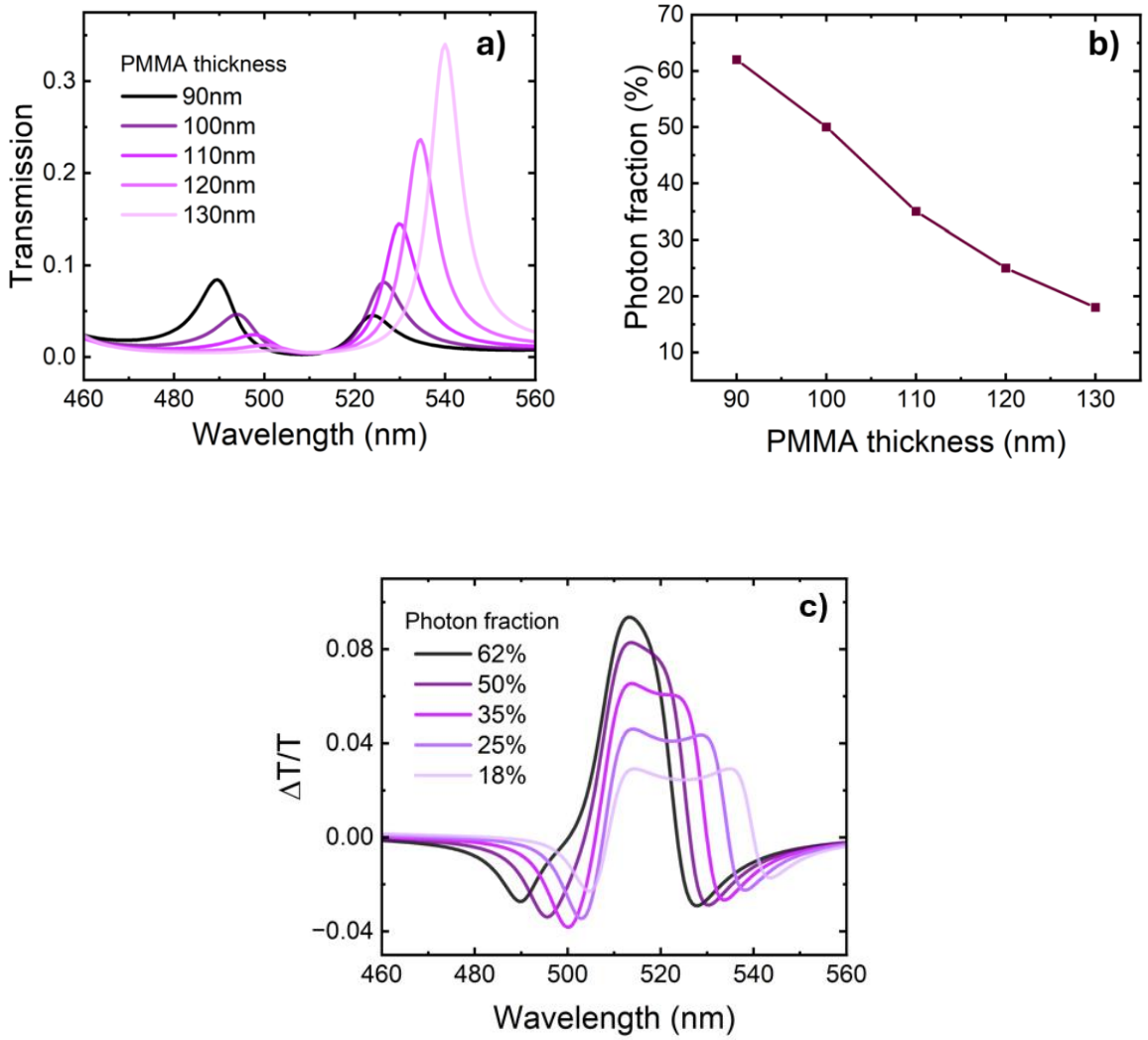

Figure S2 a) *Steady-state transmission of cavities with different PMMA thickness* ***b)*** *UPB photon fraction at normal incidence of cavities with different pmma thickness* ***c)*** *TA spectra of* $\boldsymbol{P_{cav}}$ *with different photon fractions of UPB.*

References

1 T.-Y. Liu, H. Wang, M.-S. Song, L.-Y. Zhao, Z.-F. Hu, and H.-Y. Wang, "Dynamics of Spin-Dependent Polariton–Polariton Interactions in Two-Dimensional Layered Halide Organic Perovskite Microcavities," Laser & Photonics Reviews 16(10), 2200176 (2022).

2 A. Fieramosca, R. Mastria, K. Dini, L. Dominici, L. Polimeno, M. Pugliese, C.T. Prontera, L. De Marco, V. Maiorano, F. Todisco, D. Ballarini, M. De Giorgi, G. Gigli, T.C.H. Liew, and D. Sanvitto, "Origin of Exciton–Polariton Interactions and Decoupled Dark States Dynamics in 2D Hybrid Perovskite Quantum Wells," Nano Lett. 24(27), 8240–8247 (2024).

3 M. Laitz, A.E.K. Kaplan, J. Deschamps, U. Barotov, A.H. Proppe, I. García-Benito, A. Osherov, G. Grancini, D.W. deQuilettes, K.A. Nelson, M.G. Bawendi, and V. Bulović, "Uncovering temperature-dependent exciton-polariton relaxation mechanisms in hybrid organic-inorganic perovskites," Nat Commun 14(1), 2426 (2023).

4 R. Fei, M.P. Hautzinger, A.H. Rose, Y. Dong, I.I. Smalyukh, M.C. Beard, and J. van de Lagemaat, "Controlling Exciton/Exciton Recombination in 2-D Perovskite Using Exciton–Polariton Coupling," J. Phys. Chem. Lett. 15(6), 1748–1754 (2024).

5 L. Wang, R. Nughays, J. Yin, C.-H. Shih, T.-F. Guo, O.F. Mohammed, and M. Chergui, "Band Gap Renormalization at Different Symmetry Points in Perovskites," ACS Photonics 11(6), 2273–2281 (2024).

6 A. Chernikov, C. Ruppert, H.M. Hill, A.F. Rigosi, and T.F. Heinz, "Population inversion and giant bandgap renormalization in atomically thin WS2 layers," Nature Photon 9(7), 466–470 (2015).

7 G. Yumoto, H. Tahara, T. Kawawaki, M. Saruyama, R. Sato, T. Teranishi, and Y. Kanemitsu, “Hot Biexciton Effect on Optical Gain in CsPbI3 Perovskite Nanocrystals,” J. Phys. Chem. Lett. 9(9), 2222–2228 (2018).

8 D. Babaian, D. Hill, P. Yu, and S. Guha, “Carrier relaxation and exciton dynamics in chemical-vapor-deposited two-dimensional hybrid halide perovskites,” J. Mater. Chem. C 13(1), 193–202 (2024).

9 M.C. Gélvez-Rueda, S. Peeters, P.-C. Wang, K.M. Felter, and F.C. Grozema, “Effect of Structural Defects and Impurities on the Excited State Dynamics of 2D BA2PbI4 Perovskite,” Helvetica Chimica Acta 103(9), e2000121 (2020).

10 D. Giovanni, W.K. Chong, H.A. Dewi, K. Thirumal, I. Neogi, R. Ramesh, S. Mhaisalkar, N. Mathews, and T.C. Sum, “Tunable room-temperature spin-selective optical Stark effect in solution-processed layered halide perovskites,” Science Advances 2(6), e1600477 (2016).

11 D. Giovanni, W.K. Chong, Y.Y.F. Liu, H.A. Dewi, T. Yin, Y. Lekina, Z.X. Shen, N. Mathews, C.K. Gan, and T.C. Sum, “Coherent Spin and Quasiparticle Dynamics in Solution-Processed Layered 2D Lead Halide Perovskites,” Advanced Science 5(10), 1800664 (2018).

12 Q. Li, and T. Lian, “Ultrafast Charge Separation in Two-Dimensional CsPbBr3 Perovskite Nanoplatelets,” J. Phys. Chem. Lett. 10(3), 566–573 (2019).

13 A. Shukla, G. Kaur, K.J. Babu, N. Ghorai, T. Goswami, A. Kaur, and H.N. Ghosh, “Effect of Confinement on the Exciton and Biexciton Dynamics in Perovskite 2D-Nanosheets and 3D-Nanocrystals,” J. Phys. Chem. Lett. 11(15), 6344–6352 (2020).

14 S. Renken, R. Pandya, K. Georgiou, R. Jayaprakash, L. Gai, Z. Shen, D.G. Lidzey, A. Rao, and A.J. Musser, “Untargeted effects in organic exciton–polariton transient spectroscopy: A cautionary tale,” J. Chem. Phys. 155(15), 154701 (2021).

15 J. Xie, W. Zhou, H. Li, Z. Wang, J. Jiang, Y. Zhang, X. Shen, Z. Ning, and W. Liu, “Visualizing Carrier Diffusion in Cs-Doping FAPbI3 Perovskite Thin Films Using Transient Absorption Microscopy,” Advanced Optical Materials 12(18), 2303004 (2024).

16 N.P. Weingartz, M.W. Mara, S. Roy, J. Hong, A. Chakraborty, S.E. Brown-Xu, B.T. Phelan, F.N. Castellano, and L.X. Chen, “Excited-State Bond Contraction and Charge Migration in a Platinum Dimer Complex Characterized by X-ray and Optical Transient Absorption Spectroscopy,” J. Phys. Chem. A 125(40), 8891–8898 (2021).

17 W. Thor, H.-Y. Kai, Y.-H. Yeung, Y. Wu, T.-L. Cheung, L.K.B. Tam, Y. Zhang, L.J. Charbonnière, P.A. Tanner, and K.-L. Wong, “Unearthing the Real-Time Excited State Dynamics from Antenna to Rare Earth Ions Using Ultrafast Transient Absorption,” JACS Au 4(10), 3813–3822 (2024).

18 R. Malde, M.A. Parkes, M. Staniforth, J.M. Woolley, V.G. Stavros, V. Chudasama, H.H. Fielding, and J.R. Baker, “Intramolecular thiomaleimide [2 + 2] photocycloadditions: stereoselective control for disulfide stapling and observation of excited state intermediates by transient absorption spectroscopy,” Chem. Sci. 13(10), 2909–2918 (2022).

19 G. Kaur, K. Justice Babu, N. Ghorai, T. Goswami, S. Maiti, and H.N. Ghosh, “Polaron-Mediated Slow Carrier Cooling in a Type-1 3D/0D CsPbBr3@Cs4PbBr6 Core–Shell Perovskite System,” J. Phys. Chem. Lett. 10(18), 5302–5311 (2019).

20 K. Georgiou, R. Jayaprakash, A. Askitopoulos, D.M. Coles, P.G. Lagoudakis, and D.G. Lidzey, “Generation of Anti-Stokes Fluorescence in a Strongly Coupled Organic Semiconductor Microcavity,” ACS Photonics 5(11), 4343–4351 (2018).

21 P. Deshmukh, S. Satapathy, E. Michail, A.H. Olsson, R. Bushati, R.K. Yadav, M. Khatoniar, J. Chen, G. John, B.W. Laursen, A.H. Flood, M.Y. Sfeir, and V.M. Menon, “Plug-and-Play Molecular Approach for Room Temperature Polariton Condensation,” ACS Photonics 11(2), 348–355 (2024).

Chapter 7

Conclusions and Future work

This chapter summarizes the main findings of the experimental chapters and discusses future perspectives for achieving polariton condensation in perovskite-based systems.

7.1 Conclusions

This thesis has investigated strong exciton-photon coupling, optical gain, and exciton-polariton dynamics in 2D metal halide perovskite microcavities, with a particular focus on the $n = 1$ layered perovskite BA_2PbI_4. By combining material optimization, microcavity engineering, steady-state spectroscopy, nonlinear emission measurements, and ultrafast time-resolved techniques, this work provides an assessment of the conditions required for polariton condensation in solution-processed perovskite systems and identifies the key physical mechanisms that limit its realization.

In **Chapter 4**, high-quality BA_2PbI_4 thin films were fabricated using solvent and additive engineering strategies that significantly improved surface morphology, crystallinity, and excitonic spectral sharpness. Integration of these films into DBR microcavities resulted in clear and reproducible strong exciton-photon coupling at room temperature, evidenced by pronounced anticrossing behaviour and large Rabi splitting. These results demonstrate that BA_2PbI_4 possesses the strong oscillator strength and excitonic robustness required for polariton formation, establishing a solid platform for further exploration of polaritonic phenomena.

Chapter 5 examined nonlinear optical responses at low temperatures, including amplified spontaneous emission (ASE) in bare BA_2PbI_4 films and power-dependent photoluminescence in strongly coupled microcavities. Clear ASE behaviour was observed in thin films at cryogenic temperatures, confirming that BA_2PbI_4 can support optical gain and stimulated emission. However, despite strong coupling and increased cavity quality factors, no signatures of polariton condensation were detected in microcavity structures. The absence of threshold-like superlinear emission, linewidth collapse, and large energy blueshift indicates that the system remains below the condensation threshold even under high excitation densities. These observations highlight that the presence of optical gain alone is insufficient to guarantee polariton condensation.

To uncover the origin of this limitation, **Chapter 6** employed ultrafast pump-probe spectroscopy to directly probe exciton and polariton relaxation dynamics. Transient absorption measurements revealed that carrier relaxation is dominated by ultrafast processes occurring on sub-picosecond to sub-nanosecond timescales. While reservoir-to-polariton scattering is observed on picosecond timescales, the polariton population does not persist beyond ~ 10 - 100 ps, with the longest-lived component attributed to dark or trap-associated excitons. The nanosecond-scale emission observed in time-resolved photoluminescence shown in **Chapter 4** originates from relaxed excitonic states and does not reflect sustained polariton populations. Together, these results suggest that rapid non-radiative relaxation, trapping, and finite polariton lifetimes prevent the accumulation of a macroscopic polariton population.

Taken as a whole, this thesis establishes that the absence of polariton condensation in BA_2PbI_4 microcavities is governed primarily by kinetic and dynamical limitations, rather than by insufficient exciton-photon coupling strength or lack of optical gain. Although strong coupling and ASE are both achieved, the balance between reservoir feeding, polariton lifetime, and loss mechanisms remains unfavourable for condensation. These consistent results across all

experimental chapters clarifies the fundamental challenges facing 2D perovskite-based polariton devices.

7.2 Future Directions

The findings of this thesis point toward several promising avenues for future research aimed at overcoming the limitations identified and advancing the realization of polariton condensation in 2D perovskite systems.

First, further improvements in material quality are essential. Although additive-assisted fabrication significantly enhanced film morphology, reducing trap densities and suppressing non-radiative recombination remain critical challenges. Advanced fabrication techniques, alternative organic spacer cations, and post-deposition treatments may help extend exciton lifetimes and improve the efficiency of reservoir-to-polariton scattering.

Second, cavity design and optical confinement offer substantial room for optimization. Increasing the cavity quality factor through additional DBR mirror pairs, lower-loss dielectric materials, or alternative cavity architectures, might extend polariton lifetimes.

Third, engineering the exciton reservoir represents a key strategy for enabling condensation. Resonant or quasi-resonant excitation could reduce excess carrier heating and bypass inefficient relaxation pathways, enabling a more direct population of polariton states.

Finally, extending this work to other perovskite material systems may provide improved performance. Higher-n or mixed phase quasi-2D perovskites or fully inorganic layered perovskites could likely offer enhanced carrier transport, reduced disorder, and more favourable relaxation

dynamics while retaining strong excitonic character. Comparative studies across different material platforms will be crucial for identifying optimal conditions for polariton condensation.

In conclusion, while polariton condensation was not achieved in the BA_2PbI_4 microcavities studied here, this thesis provides a detailed and coherent understanding of the physical mechanisms that limit its realization. By identifying ultrafast relaxation dynamics and cavity losses as the dominant bottlenecks, the insights gained in this work establish a roadmap for future efforts toward perovskite-based polariton lasers and non-equilibrium quantum photonic devices.